

Charles University in Prague
Faculty of Mathematics and Physics

MASTER THESIS



Jan Matoušek

Studies of Drell-Yan process at Compass experiment

Department of Low Temperature Physics

Supervisor of the master thesis: prof. Ing. Miroslav Finger, DrSc.

Study programme: Physics

Specialization: Physics of Condensed Matter and
Materials

Prague 2013

I would like to express my gratitude to my supervisor, who gave me the opportunity to get in CERN. I am indebted to Jaakko Koivuniemi for great experience, though, due to the circumstances and needs of the experiment, more in programming than physics. I wish to thank to my family, who has supported me whole five years of my study.

I declare that I carried out this master thesis independently, and only with the cited sources, literature and other professional sources.

I understand that my work relates to the rights and obligations under the Act No. 121/2000 Coll., the Copyright Act, as amended, in particular the fact that the Charles University in Prague has the right to conclude a license agreement on the use of this work as a school work pursuant to Section 60 paragraph 1 of the Copyright Act.

In date

signature of the author

Název práce: Studium procesu Drell–Yan na experimentu Compass

Autor: Jan Matoušek

Katedra: Katedra fyziky nízkých teplot (KFNT)

Vedoucí diplomové práce: prof. Ing. Miroslav Finger, DrSc., KFNT

Abstrakt: Struktura hadronu zatím není plně objasněna. Zatímco nepolarizované partonové distribuční funkce (PDFs) a PDFs závislé na helicitě jsou známy, o transversitě, a některých dalších PDFs souvisejících s příčným momentem hybnosti partonů (TMDs) informace chybějí [1]. Experiment COMPASS v CERN se v současnosti připravuje na studium TMDs pomocí Drell–Yanova (DY) procesu na příčně polarizovaném terči a pionovém svazku v letech 2014–2015 [14, 40]. Práce obsahuje úvod do problematiky partonového modelu hadronů a významu TMDs. Popisuje spektrometr COMPASS, zejména modifikace nutné pro DY program, a stručně zhodnocuje jeho možnosti v měření TMDs. Zvláštní pozornost je věnována polarizovanému terči. Práce popisuje rozpouštěcí refrigerátor, zařízení pro dynamickou polarizaci jader (DNP) a NMR systém pro měření polarizace. Také se věnuje novému software pro monitoring refrigerátoru, na němž se podílí i autor práce. Na závěr je rozebrána problematika návrhu nových NMR cívek.

Klíčová slova: Drell–Yan, struktura hadronu, nízkoteplotní polarizovaný terč, dynamická jaderná polarizace, NMR.

Title: Studies of Drell-Yan process at Compass experiment

Author: Jan Matoušek

Department: Department of Low Temperature Physics

Supervisor: prof. Ing. Miroslav Finger, DrSc., Department of Low Temperature Physics

Abstract: Hadron structure is not fully understood yet. While the spin-averaged Parton Distribution Functions (PDFs) and the helicity-dependent PDFs are well determined, little is known about the transversity and some other transverse-momentum dependent PDFs (TMDs) [1]. The COMPASS experiment at CERN is preparing for studying the TMDs using a Drell–Yan (DY) process on transversely polarized target hit by pion beam in 2014–2015 [14, 40]. An outline of the parton model of hadrons and of the TMDs is given. The COMPASS spectrometer is described, with emphasis on the modifications for the DY program, and its capabilities to measure the TMDs is briefly discussed. A special attention is paid to the polarized target. The dilution refrigerator, the DNP system for polarizing the nuclei and the NMR for polarization measurement are described. The new monitoring system of the refrigerator is described, including the author's contribution to it. Issues of the new NMR coils design are discussed.

Keywords: Drell–Yan, hadron structure, low temperature polarized target, dynamic nuclear polarization, NMR.

Contents

Introduction	3
1 Physical meaning and principles of Drell–Yan program	5
1.1 The structure of hadrons	5
1.1.1 Kinematics of scattering of leptons on hadrons	5
1.1.2 Electron-proton elastic cross section	6
1.1.3 Electron-proton inelastic cross section	7
1.1.4 Feynman’s parton model	8
1.1.5 Quark parton model, Quantum Chromodynamics	9
1.2 Transverse-spin-dependent structure of the nucleon	11
1.2.1 Nucleon spin structure in collinear approximation	11
1.2.2 Transverse-momentum dependent PDFs	13
1.3 Drell–Yan process	14
1.3.1 Unpolarized case, kinematical variables	14
1.3.2 The importance and features of Drell–Yan	16
1.3.3 Formalism of polarized Drell–Yan at COMPASS	17
1.3.4 Experimental goals of COMPASS Drell–Yan	19
1.3.5 J/ψ production — Drell–Yan duality	20
2 Realization of Drell–Yan program on COMPASS	23
2.1 General outline of COMPASS apparatus	23
2.1.1 Trigger and veto system	24
2.1.2 Tracking	24
2.1.3 RICH detector	26
2.1.4 Calorimetry	27
2.1.5 Data acquisition system	28
2.1.6 Detector control system	30
2.1.7 Drell–Yan experimental setup	30
2.2 Kinematic domain and spectrometer acceptance	33
2.3 Expected event rate and precision	35
2.3.1 Expected rate of Drell–Yan events	35
2.3.2 Expected statistical precision for asymmetries	37
3 COMPASS polarized target	39
3.1 Introduction to the polarized target	39
3.1.1 Demands on polarized targets in particle physics	39
3.1.2 Solutions used on COMPASS	39
3.1.3 Outline of the polarized target	41
3.2 Dilution refrigerator	41
3.2.1 Cooling by dilution of ^3He in ^4He	41
3.2.2 Technical solutions of the COMPASS dilution refrigerator	43
3.2.3 Low temperature thermometry and refrigerator control	45
3.2.4 Refrigerator performance	46
3.3 Dynamic nuclear polarization	47
3.3.1 System of electronic and nuclear spins and the solid effect	49

3.3.2	Spin temperature theory	51
3.3.3	Dynamic nuclear polarization at COMPASS	54
3.4	NMR polarization measurement	55
3.4.1	Principle of the NMR polarization measurement	55
3.4.2	COMPASS NMR system	57
4	Remote control and simulations of the target NMR	61
4.1	Program package pthread for remote control and monitoring	61
4.1.1	Introduction to pthread	61
4.1.2	Instrumental drivers	63
4.1.3	Current status and future of the pthread	64
4.2	Simulations of NMR coils setup	64
4.2.1	Criteria of a coil setup	64
4.2.2	Simulation with the rfindcalc package	66
4.2.3	Rfindcalc testing	67
	Conclusion	71
	Bibliography	73
	List of Abbreviations	77

Introduction

Goals of COMPASS Drell–Yan program

Open questions remain in the hadron structure, despite the wealth of data collected in the last decades. While the spin-averaged Parton Distribution Functions (PDFs) are well known and the helicity-dependent PDFs have been measured in the last 20 years, little is known about the polarizations of gluons and transversity PDF [1]. The "3-dimensional picture" of hadrons in terms of Transverse Momentum Dependent (TMD) PDFs¹ is being successfully built, but it is not complete. Especially the chiral-odd transversity and the Sivers and Boer–Mulders functions are little known.

The transversity is a leading order quantity, but it is chiral-odd, which prevents it to be studied in simple, fully inclusive Deep Inelastic Scattering (DIS). To access it, two hadrons have to be measured. One possibility is Semi-Inclusive Deep Inelastic Scattering (SIDIS), where there is one in the initial and one in the final state. The other is Drell–Yan (DY) process with two hadrons in the initial state. The two approaches are complementary. In the first the transversity is obtained from convolution of a PDF and a hadron fragmentation function, in the second from convolution of two PDFs [14]. The DY process has the advantage that only leptons have to be detected in the final state², but it is experimentally challenging due to relatively low counting rates [5].

The Common Muon and Proton Apparatus for Structure and Spectroscopy (COMPASS) is a fixed-target, high energy physics experiment at European Organization for Nuclear Research (CERN) in Geneva, Switzerland. Its purpose is to study hadron structure and spectroscopy. During the years, COMPASS has proven to be a capable and versatile apparatus. It has produced an impressive list³ of results concerning nucleon structure in the recent years [14], including SIDIS data on the Sivers function [40]. COMPASS is, during an accelerator shutdown and upgrade, preparing for the DY program planned in 2014–2015.

With the 190 GeV/ c pion beam of intensity about 6×10^7 particles per second and large polarized proton target it will be able to extract pretzelosity and transversity of proton. Moreover, there is an interesting prediction of a sign-reversal of the Boer–Mulders and Sivers functions, when they are measured by SIDIS and DY. COMPASS has an unique opportunity to test this property on a single apparatus [14]. COMPASS should deliver the first experimental results from a polarized DY process.

Polarized target

To achieve a good statistics of DY events, the COMPASS experiment requires a large, solid target with high degree of polarization. There is one of the biggest polarized target systems in the world on COMPASS. It uses the method of Dynamic

¹Called simply TMDs. They describe correlations between the spin of hadron and spins and momenta of its constituents — partons, which are identified with quarks and gluons. See the explanation of "polarized" nucleon structure in the section 1.2.

²No fragmentation model has to be used.

³For list of COMPASS publications see [15].

Nuclear Polarization (DNP) to polarize nuclei in 2.5 T field of a superconducting solenoid at temperature of about 500 mK. The polarization achieved is about two orders larger than at equilibrium. A dilution refrigerator is used to cool the target material down below 100 mK to "frozen spin mode". The polarization is measured by continuous-wave Nuclear Magnetic Resonance (NMR). Overall, the polarized target is an unique device itself, combining several interesting physical effects. It is a great experience for a low-temperature physicist to deal with it.

Motivation of the author and outline of the thesis

The purpose of this thesis is to give a wide outline over COMPASS DY program, covering the physics motivation, description of the apparatus and with an emphasis on the polarized target.

The experiments in high energy physics are usually very complex. The author believes, that if one works on a part of such experiment, although he is unable to understand its every detail, he should have a basic knowledge how the experiment works. The author contributed to the physical analysis of the modifications needed for the planned DY program and he actively cooperated on design of the new monitoring system of the dilution refrigerator. He will continue to participate on the preparations for the DY run.

The chapter 1 gives a brief introduction into the parton model and introduces the TMDs the COMPASS is going to measure. The formalism of the DY at COMPASS is briefly described and importance of the experiment with respect to the current knowledge is pointed out. The chapter 2 gives description of the apparatus, excluding the polarized target. There is a discussion of modifications for the DY program and an outline of the expected luminosity and measurement accuracy. The chapter 3 describes the polarized target. The demands on it are discussed. The refrigerator, DNP and NMR are described. The attention is paid to the physical principles as well as to the practical application. The chapter 4 is dedicated to programming. It introduces the new slow control system for the dilution refrigerator and simulations of the new NMR coil setup for the new target cells. The authors contribution to these two issues is described.

1. Physical meaning and principles of Drell–Yan program

1.1 The structure of hadrons

A general idea, of probing structure of matter by scattering experiments, dates back to the time of the famous Rutheford experiment. The angular distribution of α -particles, scattered on gold atoms, was investigated. The results showed surprisingly high number of particles scattered at large angles, which corresponded to the scattering on a point-like charge [46]. In principle very similar experimental setup was used many times later with more and more sophisticated apparatus, which allowed to go deeper and deeper into the structure of matter.

The goal of this section is to point out the way that is the structure of hadrons described using Parton Distribution Functions (PDFs) and how this approach evolved. At the end of the chapter the polarized Drell–Yan process, which is going to be studied on COMPASS experiment in the near future, is described and its importance with respect to the current knowledge is pointed out.

In the whole first chapter the natural units ($c = 1$, $\hbar = 1$) are used, unless mentioned otherwise.

1.1.1 Kinematics of scattering of leptons on hadrons

Let us first recall the kinematics of scattering of leptons on hadrons

$$l(k) + h(P) \rightarrow l(k') + X. \quad (1.1)$$

This process was important in formulation of the parton model and it is the principle of Deep Inelastic Scattering (DIS) experiments, which are in some way complementary to the Drell–Yan (DY). The lowest order Feynman diagram of special case of this process — electron-proton collision — is shown on figure 1.1b. The interaction can be mediated by photon or by intermediate vector boson. The latter is of small importance in case of charged leptons but it is the only process available in case of neutrinos. The most suitable frames for describing the process are the laboratory frame (rest frame of the proton, $\vec{P} = \vec{0}$) or the Center-of-Mass System (CMS). It is common to use relativistic invariants [12]:

$$s \equiv (k + P)^2 = M^2 + 2k \cdot P \stackrel{\text{lab.}}{=} M(2E_{\text{lab}} + M), \quad (1.2)$$

$$Q^2 \equiv -q^2 \equiv -(k - k')^2 = 2k \cdot k' = 2EE' \sin^2(\vartheta/2), \quad (1.3)$$

$$x \equiv \frac{Q^2}{2P \cdot q} \stackrel{\text{lab.}}{=} \frac{Q^2}{2M\nu}, \quad \nu \equiv E_{\text{lab}} - E'_{\text{lab}} \quad (1.4)$$

$$y \equiv \frac{P \cdot q}{P \cdot k} \stackrel{\text{lab.}}{=} \frac{\nu}{E_{\text{lab}}}, \quad (1.5)$$

$$W^2 \equiv (P + q)^2 = M^2 + Q^2 \frac{1-x}{x}. \quad (1.6)$$

The variable W has the meaning of invariant mass of the hadronic system, produced by absorption of the virtual photon by the hadron. Variable M denotes

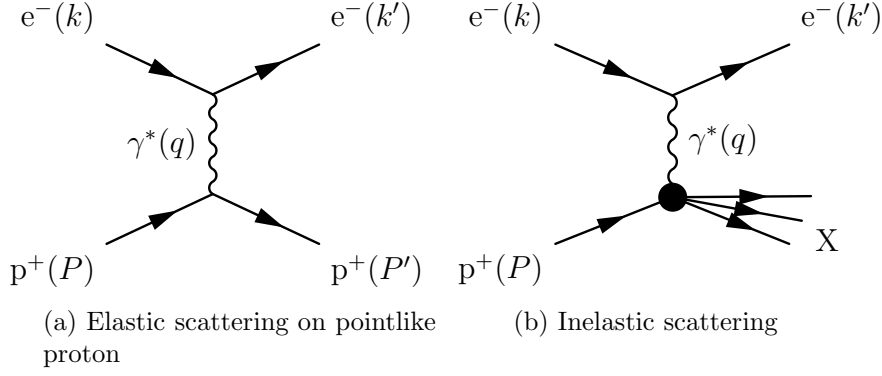


Figure 1.1: Scattering of an electron on a proton in the lowest-order Feynman diagram.

the hadron rest mass, while the lepton rest mass is neglected. The initial state is given by the Mandelstam variable¹ s . In the case of unpolarized particles the final state of the lepton can be characterized by variables x , y , Q^2 , E_{lab} and ϑ_{lab} , of which only 2 are independent. Usually (x, y) or (x, Q^2) are used as parameters of the cross section of (1.1).

In the special case of elastic scattering the final state is specified by only one variable. Simple calculation in CMS gives $x = 1$ for this case, implying also fixed $W = M$.

We can imagine rising of the virtual photon mass Q^2 as shrinking of its de Broglie wavelength. So bigger Q^2 means better spatial resolution of the experiment [46]. Process with $Q^2 \gg M^2$ and $\nu \gg M$ is called Deep Inelastic Scattering (DIS).

1.1.2 Electron-proton elastic cross section

Lets first evaluate the cross section for scattering of an electron on point-like proton (Dirac fermion) in the lowest nontrivial order of the Dyson series of Quantum Electrodynamics (QED), as is depicted on figure 1.1a.

The differential cross section for process $1 + 2 \rightarrow 3 + 4 + \dots$ is [12, 46]

$$d\sigma = \frac{(2\pi)^4}{|\vec{v}_1 - \vec{v}_2|} \frac{1}{2E_1} \frac{1}{2E_2} |M_{fi}|^2 \prod_{i=3}^n \frac{d\vec{p}_i}{(2\pi)^3 2E_i} \delta^{(4)}\left(p_1 + p_2 - \sum_{i=3}^n p_i\right) S, \quad (1.7)$$

where \vec{v}_i is velocity (in units of c) and $p_i = (E_i, \vec{p}_i)$ four-momentum of the i -th particle. Matrix element M_{fi} is the Lorentz-invariant amplitude of transition between initial and final state. S is statistical factor reflecting the case of more identical particles in final state.

The invariant amplitude squared of the figure 1.1a in QED for unpolarized particles is

$$|\overline{M}_{fi}|^2 = \frac{1}{4} \sum_{\text{spins}} \left| [\bar{u}(k', s_4) \gamma_\mu u(k, s_2)] e^2 \frac{-ig^{\mu\nu}}{q^2} [\bar{u}(P', s_3) \gamma_\nu u(P, s_1)] \right|^2, \quad (1.8)$$

¹Mandelstam s has the meaning of the total CMS energy squared.

where u, \bar{u} are Dirac bispinors and the photon propagator is taken in Feynman gauge. Using (1.7) and (1.8) we get after some treatment [12]

$$\frac{d\sigma}{dQ^2} = \frac{4\pi\alpha^2}{Q^4} \left[1 - y + \frac{y^2}{2} - \frac{M^2 y}{2k \cdot P} \right] \quad (1.9)$$

or in the laboratory frame:

$$\frac{d\sigma}{d\Omega_{\text{lab}}} = \sigma_{\text{Mott}} \frac{E'_{\text{lab}}}{E_{\text{lab}}} \left[1 + \frac{Q^2}{2M^2} \tan^2 \left(\frac{\vartheta_{\text{lab}}}{2} \right) \right], \quad \sigma_{\text{Mott}} = \frac{\alpha^2 \cos^2(\vartheta_{\text{lab}}/2)}{4E_{\text{lab}}^2 \sin^4(\vartheta_{\text{lab}}/2)}, \quad (1.10)$$

where σ_{Mott} is famous Mott formula for scattering of relativistic Dirac particle on static point charge potential and α is fine structure constant.

Lets consider proton with an **internal structure**. Quantum mechanics (as well as classical mechanics) introduces in such a case the concept of a form-factor. The amplitude of scattering on electromagnetic potential $V(\vec{r})$ generated by charge distribution $\rho(\vec{r})$ is in non-relativistic quantum mechanics given as

$$f_\rho(\vec{q}) = f_0(\vec{q})F(\vec{q}), \quad F(\vec{q}) = \int e^{-i\vec{q}\cdot\vec{r}} \rho(\vec{r}) d^3r, \quad (1.11)$$

where $f_0(\vec{q})$ is the amplitude of scattering on a unit point charge and $F(\vec{q})$ is the form-factor — the Fourier transform of $\rho(\vec{r})$ [27].

Analogical approach is taken in QED. The point-like coupling $\bar{u}(P')[ie\gamma^\mu]u(P)$ from (1.8) is replaced by a general Lorentz tensor that can be formed from four-momenta P, q and basic tensors of rank 2. Using parity conservation, gauge invariance and dropping terms that give 0 after substitution into (1.8) the general coupling is simplified into [12]

$$\bar{u}(P') \left[F_1^{\text{el.}}(Q^2) \gamma^\mu + \kappa \frac{F_2^{\text{el.}}(Q^2)}{2M} i\sigma^{\mu\nu} q_\nu \right] u(P), \quad \sigma^{\mu\nu} \equiv \frac{i}{2} (\gamma^\mu \gamma^\nu - \gamma^\nu \gamma^\mu), \quad (1.12)$$

where $F_1^{\text{el.}}, F_2^{\text{el.}}$ are elastic electromagnetic form-factors of the proton and κ is its anomalous magnetic moment. It is more convenient to use their linear combinations $G_E(Q^2)$ and $G_M(Q^2)$, called electric and magnetic form-factors. The cross section (1.10) expressed in laboratory frame then is [12, 46]

$$\frac{d\sigma}{d\Omega_{\text{lab}}} = \sigma_{\text{Mott}} \frac{E'_{\text{lab}}}{E_{\text{lab}}} \left[\frac{G_E^2 + \tau G_M^2}{1 + \tau} + 2\tau G_M^2 \tan^2 \left(\frac{\vartheta_{\text{lab}}}{2} \right) \right], \quad \tau = \frac{Q^2}{4M^2}. \quad (1.13)$$

1.1.3 Electron-proton inelastic cross section

The kinetic energy is not conserved in inelastic collisions. Energy transfer ν and Q^2 become independent. The "inelasticity" of the collision can be expressed by variable x , defined in (1.4), which equals 1 in the elastic case. This leads to dependency of the proton form-factors on two variables (if particles are unpolarized). (x, Q^2) are commonly used. The (1.13) turns into [12]

$$\frac{d\sigma}{dE' d\Omega_{\text{lab}}} = \sigma_{\text{Mott}} \frac{E'_{\text{lab}}}{E_{\text{lab}}} \left[\frac{\nu}{M} F_2(x, Q^2) + 2F_1(x, Q^2) \tan^2 \left(\frac{\vartheta_{\text{lab}}}{2} \right) \right]. \quad (1.14)$$

$$\frac{d\sigma}{dx dQ^2} = \frac{4\pi\alpha^2}{Q^4} \left[\left(1 - y - \frac{M^2 xy}{s} \right) \frac{F_2(x, Q^2)}{x} + y^2 F_1(x, Q^2) \right], \quad (1.15)$$

where $F_1(x, Q^2)$ and $F_2(x, Q^2)$ are **proton form-factors**.

These functions were studied for the first time in SLAC laboratory in the late sixties in reactions $e^- + {}^1\text{H} \rightarrow e^- + X$ and later in other laboratories using various combinations of leptons and target nucleons. These experiments show rapid decrease of elastic form-factors. The simple explanation is that if nucleon is a bound system, the higher energy that interrupts it, the smaller probability of recombination back to the initial state. This does not lead necessarily to the structure; the fall of cross sections of exclusive² reactions in general are discussed in [23].

The inelastic form-factors in contrary seemed to approach constant with rising Q^2 (above the resonance-production region) remaining only functions of x . This behaviour is called **Bjorken scaling**. In fact, the form-factors do approach zero, but very slowly — so-called approximate scaling [12].

1.1.4 Feynman's parton model

Interpretation of the data from DIS experiments at SLAC was suggested by R. P. Feynman. His famous parton model is based on idea that DIS can be modeled as "quasi-free scattering from point-like constituents within the proton, as viewed from a frame where proton has infinite momentum." [7].

In the infinite-momentum frame limit the proton is Lorentz-contracted to a disc. The internal movement of its constituents is slowed down by the time dilatation (lifetime of states inside is much longer than the duration of collision), so constituents can be handled as free during the collision. The process of hadronization³ in this model takes place much later after the e-p collision and does not affect it at all, as is depicted on figure 1.2. Altogether, the cross section (1.14), (1.15) is given by the incoherent sum of electron-parton cross sections, which have a form of (1.9)⁴. We substitute $e_i\alpha$ for α , where e_i is a fractional charge of the i -th parton.

The internal motion can be neglected with respect to the longitudinal one, so the momentum of the i -th parton can be expressed as $\eta_i P$, fraction of the proton momentum. If we write down momentum conservation law at lower vertex of figure 1.1a,

$$(\eta_i P')^2 = (\eta_i P)^2 - Q^2 + 2\eta_i P \cdot q \implies Q^2 = 2\eta_i P \cdot q, \quad (1.16)$$

we learn that variable x , defined in (1.4), corresponds to the fraction of proton momenta, carried by the hit parton. We used the fact that the collision is elastic, so the magnitudes of P , P' have to be equal. Note that this leads to conclusion that parton rest mass is dependent on its momentum $m_i = \eta_i M$. This disturbing fact can be avoided in the infinite-momentum frame where the proton appears massless. In practice the parton model is relevant only if $Q^2 \gg M$.

Lets make a high-energy limit $s \rightarrow \infty$, while x , Q^2 remain finite. The limit implies $y \rightarrow 0$. In this limit we can easily compare (1.15) with sum of N parton

²In exclusive reactions we require certain particles to be formed and no others, the opposite is inclusive.

³Generation of observed final state hadrons X .

⁴We assumed that partons have spin 1/2; the expression for spin 0 particles is anyhow quite similar [12].

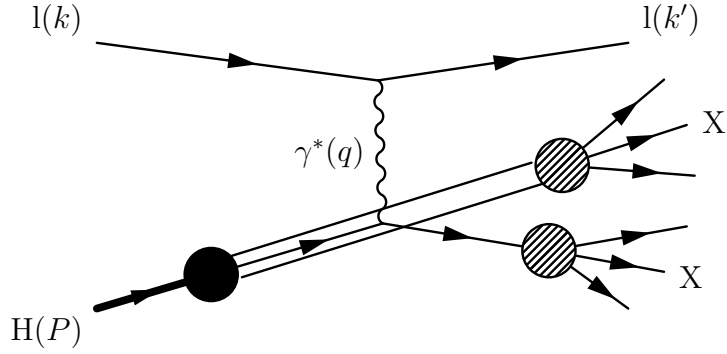


Figure 1.2: Deep inelastic scattering in parton model — scattering on quasi-free point-like parton. Hadronization follows after, here depicted as so called independent fragmentation model. The filled circle denotes PDFs and shaded fragmentation functions.

cross sections weighted by the probability $f_i(\eta)$ to find parton species i with fractional charge e_i and momentum ηP inside the proton

$$\frac{d\sigma}{dx dQ^2} = \frac{4\pi\alpha^2}{Q^4} \frac{F_2(x, Q^2)}{x} = \sum_N P_N \sum_i^N \int_0^1 \frac{4\pi\alpha^2}{Q^4} e_i^2 f_i(\eta) \delta(\eta - x) d\eta \quad (1.17)$$

$$\implies F_2(x, Q^2) = F_2(x) = x \sum_i^N e_i^2 f_i(x). \quad (1.18)$$

P_N is the probability that proton consists of N partons. We can see that this model leads to the Bjorken scaling. The functions $f_i(x)$ are called **Parton Distribution Functions (PDFs)**.

On finite energies also F_1 contributes. It can be shown that this model implies for partons with spin 1/2 the Callan–Gross relation $F_2(Q^2, x) = 2xF_1(Q^2, x)$, which was approximately confirmed by the data [12, 46].

1.1.5 Quark parton model, Quantum Chromodynamics

It is natural to identify partons with constituent quarks from static parton model. This can be properly done in Quantum Chromodynamics (QCD), but it exceeds the volume and needs of this thesis. We shall be satisfied with an intuitive understanding of its results.

Considering only u , d , s and c quark we can write the structure function F_2 of the proton as the sum of **distribution functions of quarks and antiquarks** (we denote f_i and \bar{f}_i quark and corresponding antiquark distribution, respectively) according to (1.18)

$$F_2^p = x \left(\frac{4}{9} [f_u(x) + \bar{f}_u(x) + f_c(x) + \bar{f}_c(x)] + \frac{1}{9} [f_d(x) + \bar{f}_d(x) + f_s(x) + \bar{f}_s(x)] \right). \quad (1.19)$$

A couple of problems emerges if we try to interpret partons as quarks [12]. Integrating form-factor $F_2(x)$ over x one can obtain mean square charge per parton. Value 0.17 ± 0.009 obtained from the data is far below $1/3$ given by

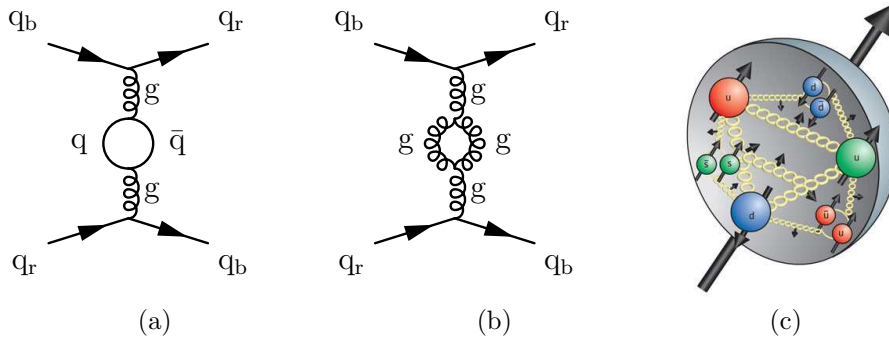


Figure 1.3: Virtual quark (a) and gluon (b) loops — the second nontrivial order of quark-quark interaction in QCD. (c) Schematic, popular view of the proton internal structure [22].

the 3-quark model. This value can not be explained even by addition of quark-antiquark pairs. There have to be also electrically neutral partons inside hadrons.

The parton distribution functions behave roughly as $1/x$ for $x \rightarrow 0$, causing the integrals $\int_0^1 f_i(x)dx$ to diverge. That means the number of charged partons in proton is infinite. Instead of quark and antiquark distribution functions $f_q(x)$, $\bar{f}_q(x)$ we can use their combinations: So called **valence** and **sea functions**. It turns out that valence functions are integrable and results for proton are in agreement with static quark model. [12]

$$f_q^{\text{val}}(x) \equiv f_q(x) - \bar{f}_q(x), \quad f_q^{\text{sea}}(x) \equiv \bar{f}_q(x) \quad (1.20)$$

$$\int_0^1 f_u^{\text{val}}(x)dx \doteq 2, \quad \int_0^1 f_d^{\text{val}}(x)dx \doteq 1. \quad (1.21)$$

The integral $\int_0^1 x f_i(x)dx$ represents the fraction of the proton momentum carried by parton of species i . Using so called isoscalar target⁵ one can measure the sum of such integrals and determine the momentum fraction carried by all quarks and antiquarks together. Such experiments showed that this fraction is about 0.5, being another clear signal of presence of uncharged particles inside hadrons.

The above mentioned properties, together with experiments with neutrinos⁶, formed our current understanding of proton structure. Hadrons are held together by **strong interactions**, described by QCD. There are 3 so called **colour charges**, R , G , B and 3 corresponding anticharges, carried by antiquarks. Interaction is mediated by massless vector bosons called **gluons**. The important difference from QED is that gluons themselves have a colour charge. This implies that quark-gluon and gluon-gluon interactions are possible. So there can be diagrams like that on figure 1.3b.

Quarks appear free in high energy collisions. On the other hand, no quarks have been observed outside hadrons, so one would expect them to be extremely

⁵Consisting of nuclei with the same number of protons and neutrons.

⁶Probing nucleon structure via weak interactions that violate particle-antiparticle symmetry brings another important informations.

tightly bound. This strange behaviour is reflected in the properties of strong-interaction coupling constant α_S . In the first order of the renormalization procedure [46]

$$\alpha_S(Q^2) = \frac{12\pi}{(33 - 2n_f) \ln \frac{Q^2}{\Lambda_{\text{QCD}}}}, \quad (1.22)$$

where n_f is the number of quark flavours in reaction and $\Lambda_{\text{QCD}} \doteq 0.2 \text{ GeV}$ is a parameter of the theory. The dependence on Q^2 is inverse than in the case of electromagnetic coupling constant. Remember that Q^2 corresponds to the wavelength of the intermediate boson. The closer are quarks to each other, the looser they are bound. This phenomenon is called **asymptotic freedom**.

The conclusions are that nucleon consists of 3 constituent, or valence, quarks, described by $f_q^{\text{val}}(x)$ distribution functions. They are bound by a potential that is consequence of complicated multi-gluon exchanges between them. The virtual quark-antiquark pairs like on figure 1.3a are formed. They exchange gluons that give rise to another quark-antiquark pairs and so forth. These particles are virtual and have to recombine after some time. But if their "virtuality" is small compared to parameter $\sqrt{Q^2}$ of proton-electron collision, they will "live" long enough for electron to scatter on them (nearly) as on real ones [12]. These quark-antiquark pairs are described by the sea distributions $f_q^{\text{sea}}(x)$.

This intuitive understanding corresponds to the experimental fact that in high- x region is the ratio of the neutron and proton form-factors $F_2^n/F_2^p \doteq 1/4$, which corresponds to valence quark dominance, and in low- x region is this ratio approaching 1 [46], corresponding to sea dominance — the excess of one u or d quark is in vast amount of quark-antiquark pairs negligible.

The internal structure of mesons is similar, but the valence partons are a quark and an antiquark.

While the parton structure of hadrons is theoretically well described, the process of hadronization, can be explain only using models. For example in the Independent Fragmentation Model is hadronization of electron-hit parton considered independent of the remaining diquark. It is described by **fragmentation function**, that express probability of produced hadron having given fraction of energy and given transverse momentum with respect to the original parton.

1.2 Transverse-spin-dependent structure of the nucleon

1.2.1 Nucleon spin structure in collinear approximation

Now we can move our attention to polarized processes. If the electron and the target nucleon in the DIS are polarized, the nucleon spin S becomes another four-vector available, except q and P , for formation of a tensor that replaces the point-like coupling $\bar{u}(P')[ie\gamma^\mu]u(P)$. More complicated tensor structures can thus be formed.

This implies that the nucleon (or hadron in general) structure is described by three structure functions (or PDFs) [12]. The unpolarized distribution function $f_1(x)$ denoted as $f_i(x)$ in the previous section, the **helicity distribution**

$$g_1(x) = f_{1i} \uparrow (x) - f_{1i} \downarrow (x) \quad (1.23)$$

describing the difference between the number densities of quarks with spin parallel and antiparallel to the longitudinally polarized hadron, and **transversity** $h_1(x)$, with the similar meaning like g_1 , but for transversely polarized hadrons. This description is valid in the leading order of the perturbative QCD in collinear approximation⁷. [6, 14]

The transversity is, though being a leading order quantity, quite a little known. The reason is that it is chiral-odd, so its measurement demands flip of the probed quark chirality. Such reactions in the fully inclusive DIS are strongly suppressed by chirality conservation condition. In order to measure $h_1(x)$ the chirality must be flipped twice, so either two hadrons in the initial state (like in DY) or one in the initial and one in the final state (like in semi-inclusive DIS or leptonproduction) are needed. [6].

On the other hand helicity distribution have been quite successfully measured several times. The way how to access it experimentally can be outlined using simple tools of QED and the quark parton model.

Lets consider longitudinally polarized proton and electron. There actually is no other possibility, if we want to stay at the approximation neglecting their masses, because massless particles can be polarized only in the direction of their momentum. The experimentally accessible quantities are the cross sections $\sigma \uparrow\uparrow$, $\sigma \uparrow\downarrow$ of parallel and antiparallel polarized target and beam. To point out the effect of spins the **asymmetry** A is defined as

$$A \equiv \frac{\sigma \uparrow\uparrow - \sigma \uparrow\downarrow}{\sigma \uparrow\uparrow + \sigma \uparrow\downarrow}. \quad (1.24)$$

If we want to calculate the scattering amplitude squared for polarized pointlike Dirac particles, we use the equation (1.8), but we omit averaging of incoming particles spins s_1, s_2 . Using trivial equality $a = \text{Tr}(a)$ for scalar a , properties of trace and chiral projectors $\frac{1 \pm \gamma_5 s}{2}$ (we neglect masses of both particles) we write

$$|M_{fi}|^2 = \frac{e^4}{Q^4} \sum_{s_{3,4}} \text{Tr} \left[\not{k}' \frac{1 + \gamma_5 s_4}{2} \gamma^\mu \not{k} \frac{1 + \gamma_5 s_2}{2} \gamma^\nu \right] \text{Tr} \left[\not{p}' \frac{1 + \gamma_5 s_3}{2} \gamma_\mu \not{p} \frac{1 + \gamma_5 s_1}{2} \gamma_\nu \right]. \quad (1.25)$$

After some treatment, using properties of trace and γ -matrices, we get the result

$$|M_{fi}|^2 = \frac{e^4}{64Q^2} [(1 - s_1 s_2) s^2 + (1 + s_1 s_2) u^2], \quad (1.26)$$

where $s = (k + P)^2 = 2k \cdot P$ and $u = (k - P')^2 = -2k \cdot P'$ are standard Mandelstam variables. This implies we can express relation between cross sections of polarized Dirac particles simply, using y from (1.5), as

$$\sigma \uparrow\uparrow = (1 - y)^2 \sigma \uparrow\downarrow. \quad (1.27)$$

In simple quark parton model we write proton-electron cross section as an incoherent sum of quark-electron cross sections, but now we have to consider quark

⁷The transverse momentum of partons is neglected, as was stated in section 1.1.4 about parton model.

polarizations, given by the helicity distribution $g_1(x)$:

$$\sigma_p \uparrow\uparrow(x) = \sum_i e_i^2 \left[\frac{f_{1i}(x) + g_{1i}(x)}{2} \sigma_{\uparrow\uparrow} + \frac{f_{1i}(x) - g_{1i}(x)}{2} \sigma_{\uparrow\downarrow} \right]. \quad (1.28)$$

Finally we get the relation between asymmetry and helicity distribution:

$$A(x) = \frac{(y-1)^2 - 1}{(y-1)^2 + 1} \frac{x}{F_2(x)} \sum_i e_i^2 g_{1i}(x). \quad (1.29)$$

The conclusion is that, as long as we know the unpolarized structure function, the helicity distribution is experimentally accessible measuring asymmetry $A(x)$.

This was done in the SMC⁸ experiment at CERN. Polarized muon beam and polarized proton and neutron targets were used. The total contribution of quark spins to the total nucleon spin was evaluated. It was shown, that [12]

$$\Gamma_1^p = \int_0^1 \sum_i e_i^2 g_{1i}^p(x) dx = +0.136 \pm 0.011, \quad (1.30)$$

$$\Gamma_1^n = \int_0^1 \sum_i e_i^2 g_{1i}^n(x) dx = -0.063 \pm 0.024. \quad (1.31)$$

If we consider isospin symmetry and neglect the strange quark contribution, we can by addition of these two results obtain total fraction of the spin carried by u and d quarks [12]

$$\Gamma_1^p + \Gamma_1^n = \frac{5}{18} \left(g_{1u} + g_{1d} + \frac{2}{5} g_{1s} \right) = 0.073 \pm 0.03 \quad (1.32)$$

$$g_{1u} + g_{1d} = 0.26 \pm 0.09. \quad (1.33)$$

This implies that there have to be other significant contributions to the nucleon spin. With more careful treatment the contribution of u , d and s quarks is 0.27 ± 0.11 [12]. The question of what carries most of the nucleon spin is still to be solved. The gluon spins or quark and gluon angular momenta are possibly to blame. One of the goals of the Common Muon and Proton Apparatus for Structure and Spectroscopy (COMPASS) experiment is to help to reveal this puzzle.

1.2.2 Transverse-momentum dependent PDFs

There have been several experimental observations, which can not be explained in collinear approximation. The quark transverse momentum \vec{k}_T with respect to the hadron momentum has to be taken into account. There are two main approaches in QCD that go beyond the above sketched model of three PDFs. One uses collinear twist-3 quark-gluon correlation functions in the formalism of collinear factorization, the second generalizes Feynman's original parton picture by transverse-momentum dependent factorization and deals with **Transverse**

⁸The Spin Muon Collaboration (SMC) was performing experiments in 90's and is a direct ancestor of the COMPASS experiment.

Momentum Dependent (TMD) PDFs⁹ [14]. The first approach is applicable for large transverse momentum $k_T \gg \Lambda_{QCD}$. The latter is suitable for small transverse momentum, which is the case of DY at COMPASS. [14] Because of that the TMD approach will be only discussed in this thesis.

Assuming time-reversal invariance, the hadron structure is described by six PDFs: $f_1(x, k_T^2)$, $g_{1L}(x, k_T^2)$, $h_1(x, k_T^2)$, $g_{1T}(x, k_T^2)$, $h_{1T}^\perp(x, k_T^2)$ and $h_{1L}^\perp(x, k_T^2)$. The first three functions, when integrated over k_T^2 , give the simple $f_1(x)$, $g_1(x)$ and h_1 distributions. The other three after integration over k_T^2 disappear. [6, 14]

If we do not impose time-reversal invariance condition, two more T -odd distributions emerge. The **Boer–Mulders function** $h_1^\perp(x, k_T^2)$ describes the correlation between transverse spin and transverse momentum of the quark within an unpolarized nucleon. The **Sivers function** $f_{1T}^\perp(x, k_T^2)$ describes the influence of the transverse spin of the nucleon on the quark transverse momentum. [6, 14]

We have adopted here so called Amsterdam notation of PDFs. The letters f , g and h denote unpolarized, longitudinally polarized and transversely polarized quark distributions, respectively. The subscript 1 labels leading twist quantity. Subscripts T and L mean that parent hadron is transversely or longitudinally polarized and superscript \perp signals the presence of transverse momenta with uncontracted Lorentz indices. [6]

The Drell–Yan (DY) program of COMPASS experiment concentrates mainly on transversity h_1 and the latter two, T -odd, PDFs. As was discussed in previous subsection, the chirally-odd transversity can be also investigated by other processes, like Semi-Inclusive Deep Inelastic Scattering (SIDIS). In such reactions the chirality is conserved through convolution of PDFs with polarized quark fragmentation function [14]. The advantage of DY is that there is no fragmentation to deal with, because we observe no hadrons in the final state.

In the past ten years first measurements of SIDIS with transversely polarized targets were performed by the COMPASS and HERMES (DESY) collaborations at beam energies of 160 GeV and 27.5 GeV, respectively. Their results together with these of BELLE Collaboration permitted to extract the Collins fragmentation function¹⁰ and u and d transversity functions. The Sivers asymmetry was also measured and was found different from zero for proton and positive pions and kaons (see figure 1.4). The Boer-Mulders function was estimated, but open questions remain. [14]

1.3 Drell–Yan process

1.3.1 Unpolarized case, kinematical variables

The production of dilepton pairs in hadron-hadron collisions

$$H_a(P_a) + H_b(P_b) \rightarrow l^-(k) + l^+(k') + X \quad (1.34)$$

can in quark parton model proceed via diagram in figure 1.5b, such process is called Drell–Yan (DY) (after its discoverers, see [21]). We denote $P_{a,b}$ momenta of the hadrons, $q = k + k'$ the total momentum of the dilepton pair (or equivalently

⁹Often simply referred to as TMDs.

¹⁰Describe fragmentation of transversely polarized quark into unpolarized hadron.

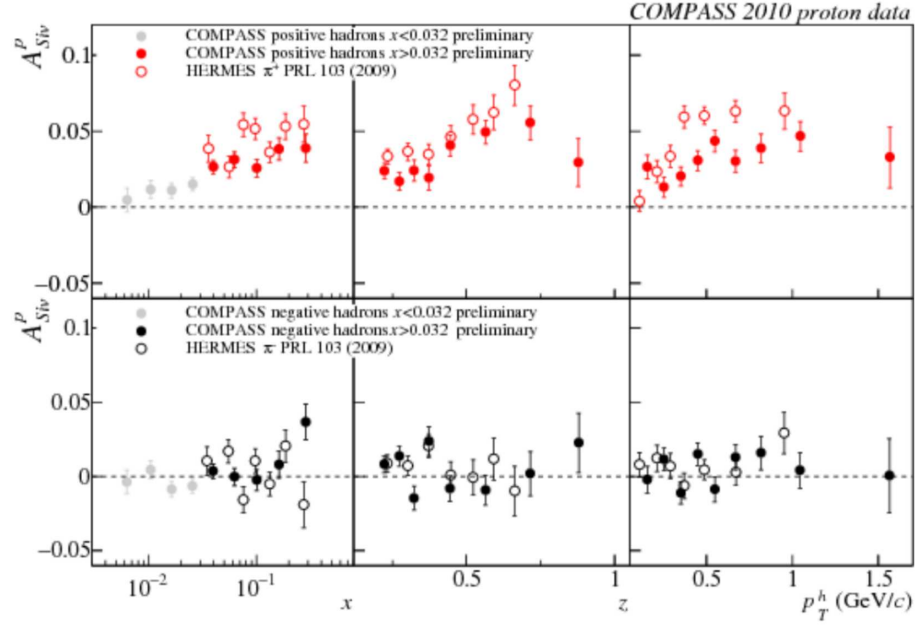


Figure 1.4: Sivers function for positive (upper figure) and negative (bottom figure) hadrons as measured by COMPASS and HERMES in SIDIS [40].

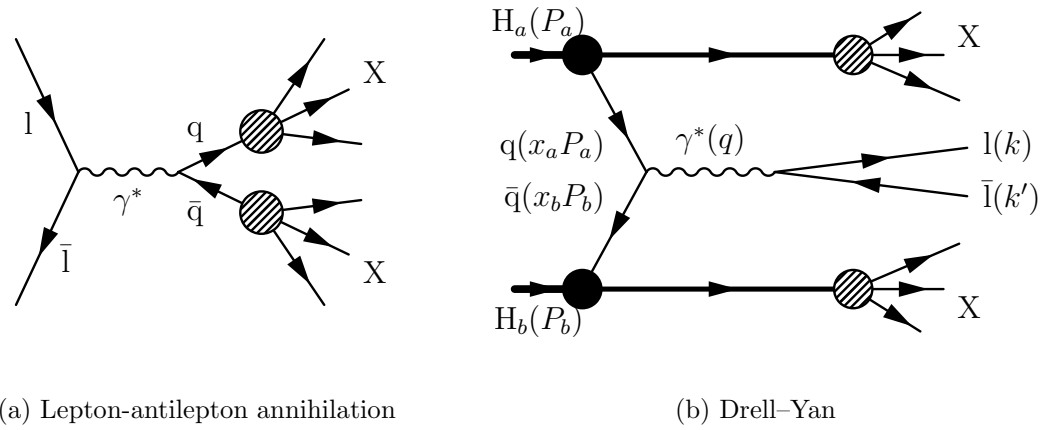


Figure 1.5: DIS (figure 1.2) is based on lepton-quark scattering. Other possibilities how to probe hadron structure using leptons are processes based on "90° rotated" annihilation diagram. The filled circles denotes PDFs and shaded fragmentation functions in independent fragmentation model.

of the virtual photon). We assume that hadrons collide head-on along the z -axis in our reference frame. Experimentally can be the dilepton pair characterized by its invariant mass $m = \sqrt{q^2}$ and its momentum \vec{q} ¹¹. More practical is use of two dimensionless parameters

$$x_F \equiv x_a - x_b \doteq \frac{2|\vec{q}|}{\sqrt{s}}, \quad \tau \equiv \frac{4m^2}{s}, \quad \text{where} \quad x_{a,b} = \frac{q^2}{2P_{a,b} \cdot q}. \quad (1.35)$$

The variable s is as usual the total CMS energy of hadrons squared and x_a, x_b are fractions of hadron momenta. The parameter x_F is usually called Feynman variable and the approximate equality holds if we neglect quark masses. In that case we find also $m^2 = x_a x_b s$. Using quark parton model we can express the cross section [12]

$$\frac{d\sigma}{dm^2 dx_F} = \frac{1}{3} \left[\frac{4\pi\alpha^2 e_i^2}{3m^2} \right] \sum_i \int f_{1i}(x_a) \bar{f}_{1i}(x_b) \delta(x_a x_b s - m^2) \delta(x_a - x_b - x_F) dx_a dx_b, \quad (1.36)$$

the term in square brackets being the parton-antiparton (pointlike) cross section. The factor $1/3$, which reflects the probability that both quark and antiquark have the same color charge, is there because colorless leptons are produced. The index i runs over both quarks and antiquarks to take into account both cases quark being from hadron H_a and antiquark from H_b and vice versa. Evaluating the expression we obtain

$$\frac{m^3 d\sigma}{dm dx_F} = \frac{8\pi\alpha^2}{9\sqrt{x_F^2 + \tau}} \left[\sum_i e_i^2 f_{1i}(x_a) \bar{f}_{1i}(x_b) \right]. \quad (1.37)$$

The right hand side of the equation scales with variable τ independently on PDFs, which was experimentally verified (outside the resonance region) [12]. This is another example of scaling behaviour of parton model.

1.3.2 The importance and features of Drell–Yan

Unpolarized DY process played an important role in determining PDFs of hadrons. Information obtained from DY is complementary to that from DIS and it was crucial for measurement of structure of pions and kaons, which can not be investigated by DIS. [5, 12]

The DY still attracts attention of both experimentalists and theoreticians, this time mostly its polarized version. As was stated before, it allows to study the chirally-odd transversity distribution, TMDs and also other interesting phenomena in both perturbative and nonperturbative QCD. It was also mentioned that using DY has an advantage that no hadron is detected in final state so no fragmentation mechanism has to be assumed. On the other hand it is experimentally challenging due to relatively low counting rates. [5]

As was sketched in previous subsection, the PDFs of two hadrons act in DY in convolution. They can be extracted using QCD-factorization theorem, which applies if masses of produced leptons is sufficiently large [5]. This is one reason

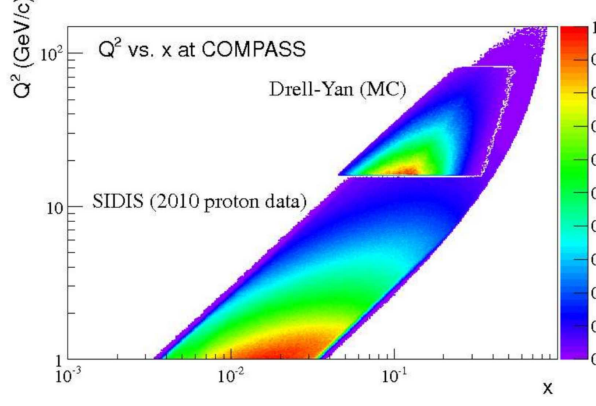


Figure 1.6: Covered region in x and Q^2 of COMPASS SIDIS and DY experiments [40].

to look for muons in final state, as COMPASS is going to do. The other is that muons are easily distinguished in detectors from other particles.

There are several DY experiments planned in near future. DY studies are planned in nucleon-nucleon collisions in next years on RHIC (2016 or later), J-PARC (KEK, 2018 or later) and NICA (JINR, Dubna, 2018 or later) and antiproton-nucleon collisions at FAIR (GSI, 2018 or later) [40]. There is also a plan to study both nucleon-nucleon and pion-nucleon DY at IHEP (Protvino¹²). The pion-proton DY program at COMPASS is going to start in 2014/2015¹³. The experimental interest in the field illustrates its significance for understanding the hadron structure. Complementary approach is based on SIDIS process and extracts results from PDF-fragmentation function convolution. The opportunity to perform both types of measurement on the same apparatus will be unique at COMPASS (see figures 1.4, 1.6).

1.3.3 Formalism of polarized Drell–Yan at COMPASS

In COMPASS DY program the reaction

$$\pi^-(P_\pi) + p(P_p, S_p) \rightarrow \gamma^*(q) + X \rightarrow \mu^-(l) + \mu^+(l') + X \quad (1.38)$$

will be studied with **negative-pion beam** and **transversely polarized proton target**. S_p is proton spin four-vector with properties $P_p \cdot S_p = 0$, $S_p^2 = -1$. Two reference frames are convenient to describe DY [14]:

The target rest frame (TF) is defined by unit vectors \hat{z} along the beam-hadron momentum, \hat{x} along the transverse component q_T of the virtual photon momentum and $\hat{y} = \hat{y} \times \hat{x}$. This definition implies:

$$P_{\pi, \text{TF}} = (P_{\pi, \text{TF}}^0, 0, 0, P_{\pi, \text{TF}}^3), \quad P_{p, \text{TF}} = (M_p, 0, 0, 0), \quad (1.39)$$

$$q_{\text{TF}} = (q_{\text{TF}}^0, q_T, 0, q_{\text{TF}}^3), \quad S_{\text{TF}} = (0, S_T \cos \phi_S, S_T \sin \phi_S, S_L), \quad (1.40)$$

where ϕ_S is an angle between transverse (with respect to \hat{z}) components of spin and virtual photon momentum (see figure 1.7a).

¹¹The choice of frame implies $\vec{q} \parallel z$.

¹²Timescale unknown to the author of this thesis.

¹³Second data taking is proposed for 2017 [40].

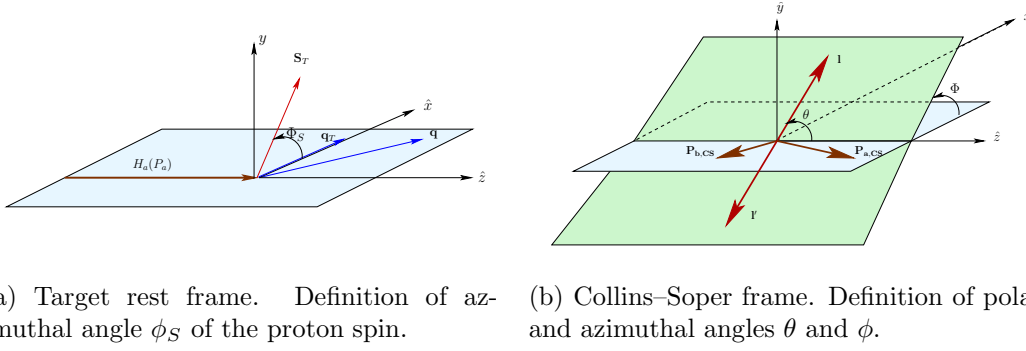


Figure 1.7: Definition of angles in coordinate systems for DY. Here P_π , P_p are denoted P_a , P_b , respectively [14].

The Collins-Soper frame (CS) is the rest frame of the virtual photon. It is obtained from TF by boosting along the photon momentum. Neglecting the muon mass, the muon and antimuon momenta in CS frame are

$$l_{\text{CS}} = \frac{q}{2}(1, \sin \theta \cos \phi, \sin \theta \sin \phi, \cos \theta), \quad (1.41)$$

$$l'_{\text{CS}} = \frac{q}{2}(1, -\sin \theta \cos \phi, -\sin \theta \sin \phi, -\cos \phi). \quad (1.42)$$

The polar and azimuthal angles θ and ϕ define orientation of dimuon momenta (see figure 1.7b).

The general form of DY cross section with polarized nucleons in the initial state in one-photon-exchange approximation was derived in [5]. The expression was adapted and simplified for the case of only one polarized nucleon in the COMPASS Note [34]. Assuming the factorization theorem it was shown that at high energies (s , $q^2 \gg M_\pi^2$, M_p^2) and small transverse momentum $q_T \ll q$ the cross section can be expressed as a convolution over TMDs. Such a convolution is defined as

$$\mathcal{C}[w(k_{\pi T}, k_{pT}) f_1 \bar{f}_2] \equiv \frac{1}{N_c} \sum_i e_i^2 \int \delta^{(2)}(q_T - k_{\pi T} - k_{pT}) w(k_{\pi T}, k_{pT}) \quad (1.43)$$

$$[f_1^i(x_\pi, k_{\pi T}^2) \bar{f}_2^i(x_p, k_{pT}^2) + \bar{f}_1^i(x_\pi, k_{\pi T}^2) f_2^i(x_p, k_{pT}^2)] d^2 k_{\pi T} d^2 k_{pT},$$

where N_c is number of colors and $f_i(x, k_T^2)$ are TMDs, depending on momentum fraction x and magnitude of transverse momentum $|\vec{k}_T|$.

For the case of transversely polarised target and in the leading order (LO) of QCD parton model we obtain [34]

$$\frac{d\sigma}{d^4 q d\Omega} \stackrel{\text{LO}}{=} \frac{\alpha^2}{F q^2} \hat{\sigma}_U \left\{ (1 + D_{[\sin^2 \theta]} A_U^{\cos 2\phi} \cos 2\phi) \right. \quad (1.44)$$

$$+ |\vec{S}_T| \left[A_T^{\sin \phi_S} \sin \phi_S + D_{[\sin^2 \theta]} \left(A_T^{\sin(2\phi + \phi_S)} \sin(2\phi + \phi_S) \right. \right.$$

$$\left. \left. + A_T^{\sin(2\phi - \phi_S)} \sin(2\phi - \phi_S) \right) \right] \left. \right\},$$

where the spatial angle Ω specifies the orientation of the muon and

$$F = 4\sqrt{(P_\pi \cdot P_p)^2 - M_\pi^2 M_p^2}, \quad (1.45)$$

$$\hat{\sigma}_U \stackrel{\text{LO}}{=} F_U^1 (1 + \cos^2 \theta), \quad D_{[f(\theta)]} \stackrel{\text{LO}}{=} \frac{f(\theta)}{1 + \cos^2 \theta}. \quad (1.46)$$

Parameter F represents the flux of incoming pions, $D_{[f(\theta)]}$ is called depolarization factor and $\hat{\sigma}_U$ is the part of the cross section which survives integration over azimuthal angles ϕ and ϕ_S . The unpolarized structure function F_U^1 corresponds in leading order to

$$F_U^1 \stackrel{\text{LO}}{=} \mathcal{C}[f_1 \bar{f}_1]. \quad (1.47)$$

and asymmetries $A_P^{f(\theta, \phi, \phi_S)}$ ($P = U, T$ for polarization-independent and transverse-polarization dependent asymmetries, respectively) to [34]

$$A_U^{\cos 2\phi} \stackrel{\text{LO}}{=} \mathcal{C} \left[\frac{2(\vec{h} \cdot \vec{k}_{\pi T})(\vec{h} \cdot \vec{k}_{pT}) - \vec{k}_{\pi T} \cdot \vec{k}_{pT}}{M_\pi M_p F_U^1} h_1^\perp \bar{h}_1^\perp \right], \quad (1.48)$$

$$A_U^{\sin \phi_S} \stackrel{\text{LO}}{=} \mathcal{C} \left[\frac{\vec{h} \cdot \vec{k}_{pT}}{M_p F_U^1} f_1 \bar{f}_{1T}^\perp \right], \quad (1.49)$$

$$A_T^{\sin(2\phi+\phi_S)} \stackrel{\text{LO}}{=} -\mathcal{C} \left[\frac{2(\vec{h} \cdot \vec{k}_{pT})[2(\vec{h} \cdot \vec{k}_{\pi T})(\vec{h} \cdot \vec{k}_{pT}) - \vec{k}_{\pi T} \cdot \vec{k}_{pT}] - k_{pT}^2(\vec{h} \cdot \vec{k}_{\pi T})}{4M_\pi M_p^2 F_U^1} h_1^\perp \bar{h}_{1T}^\perp \right], \quad (1.50)$$

$$A_T^{\sin(2\phi-\phi_S)} \stackrel{\text{LO}}{=} -\mathcal{C} \left[\frac{\vec{h} \cdot \vec{k}_{\pi T}}{2M_\pi F_U^1} h_1^\perp \bar{h}_1 \right], \quad (1.51)$$

where $\vec{h} = \vec{q}_T/q_T$. We can see that measurement of asymmetries gives access:

- $A_U^{\cos 2\phi}$ to the Boer–Mulders function of the beam pion,
- $A_T^{\sin \phi_S}$ to the Sivers function of the target proton,
- $A_T^{\sin(2\phi+\phi_S)}$ to the Boer–Mulders function of the beam pion and to the "pretzelosity" function h_{1T}^\perp of the target nucleon,
- $A_T^{\sin(2\phi-\phi_S)}$ to the Boer–Mulders function of the beam pion and to the transversity function h_1 of the target proton.

Beyond the leading order more asymmetries emerge¹⁴. Within the QCD TMDs approach they can be viewed as kinematic corrections of higher order in q_T/q .

1.3.4 Experimental goals of COMPASS Drell–Yan

The two T -odd PDFs, Boer–Mulders function h_1^\perp and Sivers function f_{1T}^\perp , are process dependent. It is possible to show, on quite general grounds, that these

¹⁴Overall twelve in case of unpolarized beam hadron, see [34] or for more general expressions [5].

functions extracted from DY and SIDIS measurements should have **opposite signs** [14].

$$f_{1T}^\perp \Big|_{\text{DIS}} = -f_{1T}^\perp \Big|_{\text{DY}}, \quad h_1^\perp \Big|_{\text{DIS}} = -h_1^\perp \Big|_{\text{DY}}. \quad (1.52)$$

As was mentioned before, observations of non-zero Sivers function were performed by COMPASS and HERMES in SIDIS processes. By measuring the $A_T^{\sin \phi_S}$ asymmetry, which is given as a convolution of the pion f_1 PDF (which is known) and nucleon Sivers function (eq. (1.49)), the first verification of the sign-reversal property of Sivers function shall be performed on COMPASS.

The Boer–Mulders function can be extracted from both polarized and unpolarized DY, but in the unpolarized case there is only convolution of two of them. In polarized case it couples to other PDFs, so only polarized experiment is sensitive to its sign. [14]

The DY measurement on COMPASS will allow to extract the pretzelosity and transversity functions h_{1T}^\perp and h_1 , respectively (eqs. (1.50) and (1.51)). To extract them, the knowledge of the Boer–Mulders function of the pion is needed. This can be accomplished either by putting some constraints on transversity and extract both from $A_T^{\sin(2\phi-\phi_S)}$ or by using existing data from unpolarized DY measurements, especially recent data from E866/NuSea, which reported extraction of Boer–Mulders function of proton. [14]

Overall, by performing measurements of target-spin-(in)dependent asymmetries in the Drell–Yan process, and comparing them to those of SIDIS, the important verification of universality of the TMD approach to description of these reactions will be performed. This would mean also a test of QCD in non-perturbative regime [14]. See the section 2.3.2 for discussion of measurement precision.

1.3.5 J/ψ production — Drell–Yan duality

In spite of large amount of experimental data the production mechanism of J/ψ is still unclear. The vector boson J/ψ with rest mass about $M_{J/\psi} = 3.1$ GeV, which is bound state of c and \bar{c} , can be produced in reactions

$$H_a + H_b \rightarrow J/\psi + X \rightarrow l^- + l^+ + X. \quad (1.53)$$

The cross section of this process consists of contributions from quark-antiquark and gluon-gluon interactions. Quark-antiquark regime dominates at relatively low energies. If angular dependencies are included, the lack of data does not allow to construct a model capable of quantitative predictions. [14]

In this situation a model based on the close analogy (duality) of (1.53) and Drell–Yan process (1.34) attracted much attention. In the $q\bar{q}$ dominance region, since both J/ψ and γ are vector particles and helicity structure of $q\bar{q}(J/\psi)$ and $(q\bar{q})\gamma^*$ couplings is the same, one can obtain J/ψ production cross section from that of DY by simple replacements [14]

$$16\pi^2\alpha^2 e_q^2 \rightarrow (g_q^{J/\psi})^2 (g_l^{J/\psi})^2, \quad \frac{1}{M^4} \rightarrow \frac{1}{(M^2 - M_{J/\psi}^2)^2 + M_{J/\psi}^2 \Gamma_{J/\psi}^2}, \quad (1.54)$$

where $M^2 \equiv q^2$ is the squared invariant mass of the dilepton pair and $\Gamma_{J/\psi}$ is the full J/ψ width.

It is believed that this model holds for both unpolarized and polarized cases. In the region of u -quark dominance (large Bjorken x) all couplings exactly cancel in ratios (like asymmetries), so that they become the same for DY and J/ψ production. This enables to use the J/ψ production region for extraction of PDFs, which will significantly help the analysis because the dilepton production rate is about a factor 30 higher in this region than in DY continuum region above the J/ψ mass. [\[14\]](#)

Though the main goal of COMPASS DY program is to collect enough data in the "safe" dimuon mass region 4–9 GeV and use the J/ψ data, which will come as a by-product, to a separate analysis.

2. Realization of Drell–Yan program on COMPASS

This chapter at the beginning briefly describes the COMPASS spectrometer, with exception of the polarized target, which is reported to in more detail in the Chapter 3. Then it focuses on Drell–Yan program realization, on expected acceptance, event rates and errors of measured asymmetries.

2.1 General outline of COMPASS apparatus

In 1997 the COMPASS (Common Muon and Proton Apparatus for Structure and Spectroscopy) was approved by CERN as an experiment NA-58. It was installed in 1999-2000 and commissioned during a technical run in 2001. It is located in hall 888 on **CERN Prévessin site** near Geneva. It is a place with interesting history. In the very same hall the NMC, EMC and SMC collaborations performed their target experiments and brought important information about hadron structure.

The unique M2 beam line delivers hadron or naturally polarized muon beams in energy range between 50 GeV and 280 GeV from **Super Proton Synchrotron (SPS)** into the hall. The spectrometer itself (excluding the beam monitoring) is about 60 m long. Its parts are placed in the hall one after another in a sandwich-like pattern. They are relatively independent, some are on rails and there is a powerful crane available, so the setup is quite variable. For example, the polarized target, used in muon-nucleon SIDIS program, was for needs of deep virtual Compton scattering and deep virtual meson production replaced by liquid-hydrogen target with a 4 m long recoil proton detector surrounding it. This illustrates how flexible and versatile tool is the COMPASS spectrometer.

The apparatus consists of three parts — detectors upstream of the target (monitoring the beam), and the Large Angle Spectrometer (LAS) and the Small Angle Spectrometer (SAS) downstream of the target, analyzing scattered or new-born particles. The use of two spectrometers is a consequence of large momentum range and large angular acceptance requirements. Each of the spectrometers has a bending dipole magnet (in red on figure 2.1), trackers, muon filter and electromagnetic and hadron calorimeters. The LAS has in addition a Ring-Imaging Cherenkov (RICH) detector. [14, 15]

The spectrometer setup is shown on figure 2.1. The **LAS** is built around a bending magnet SM1, which is designed to have ± 180 mrad angular acceptance. Its field lines are perpendicular to the tracks pointing to the target. Its field integral was measured about 1 Tm, which corresponds to deflection of 300 mrad for particles with momentum of 1 GeV/c [1]. It is followed by trackers and a RICH detector, electromagnetic calorimeter ECAL1, hadron calorimeter HCAL1, a muon filter and trackers behind it to detect muons. The calorimeters and the filter have holes fitting the SAS angular acceptance.

The task of **SAS** is to detect particles at angles in range ± 30 mrad and large momenta of 5 GeV/c and higher. Its central element is a bending magnet SM2 with a field integral about 4.4 Tm [1]. The current of 4000 A is needed to feed the magnet. It is surrounded by trackers. The electromagnetic and hadron

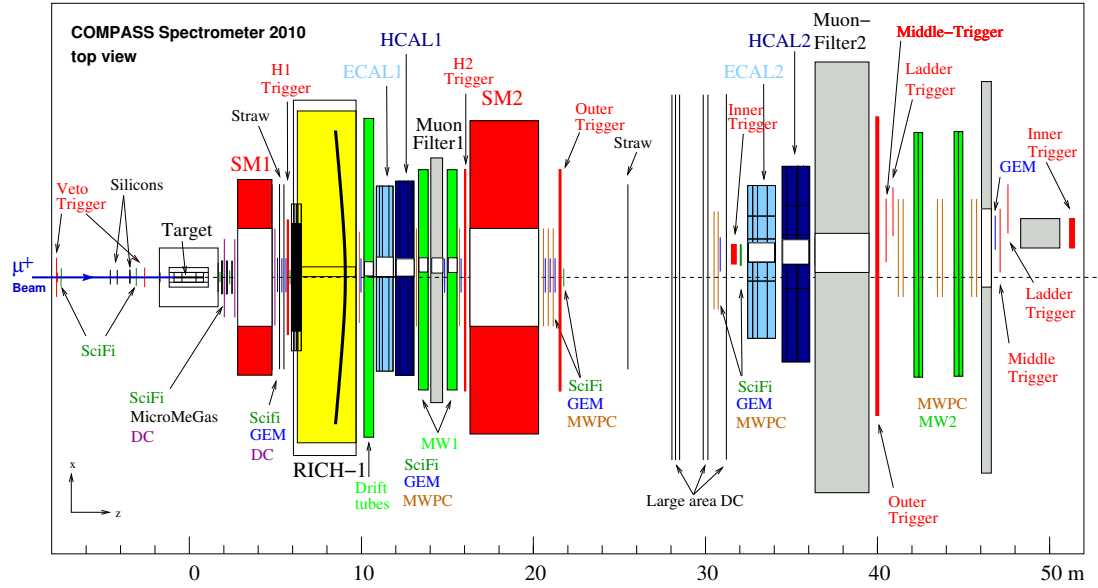


Figure 2.1: Top view of the 2010 COMPASS spectrometer setup (used with muon beam and polarized ammonia target) [14]. The longitudinal and transverse dimensions are not to scale. A hadron absorber will be placed right after the target for DY program.

calorimeters ECAL2 and HCAL2 follow and the spectrometer is closed with a second muon filter.

2.1.1 Trigger and veto system

DY measurements depend on good recognition of two oppositely charged muons. The real DY events have to be distinguished from pion decays, reactions in the hadron absorber and other possible muon sources. The decision whether to record an event has to be taken in less than 500 ns. Muons are detected behind thick concrete or iron absorbers, that filter out another particles. The fast scintillator hodoscopes will be used to measure either scattering angle in a plane perpendicular to the dipole bending plane ("target pointing trigger") or the energy loss using the deflection in the dipole fields ("energy loss trigger"). Due to the variety of counting rates, the four trigger systems are being used for different kinematic regions.

Veto system is very similar to the trigger system, but it plays an opposite role. It should disable detection of muons originating outside the target volume. This is very important in the case of muon beam, which has a large halo. In the DY program is veto system less critical.

2.1.2 Tracking

The requirements on trackers vary greatly with the distances from the target and from the beam axis. Right after the target the trackers have to cope with a high particle rate and requirements on excellent spatial resolution. In addition

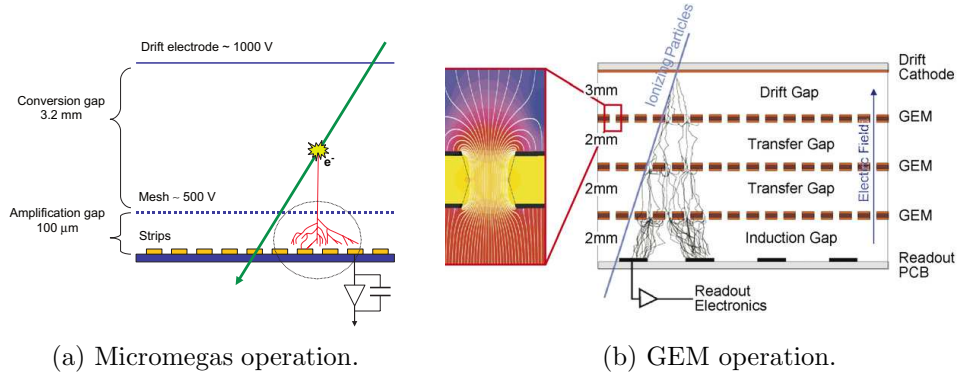


Figure 2.2: Small area trackers [1].

the amount of material in the way of the beam path has to be minimized to prevent multiple scattering and secondary interactions. In contrary, far from the beam the demands are not so severe, but a large area has to be covered. These differences imply that various tracking techniques are used. Some of the tracking technologies have been designed and tested on COMPASS itself.

Very small area trackers cover the space closest to the beam. They have to combine high flux capabilities (up to a few MHz per channel) and extremely fine spatial resolution ($100 \mu\text{m}$ and better). The couple of scintillating-fibers stations are used to monitor the beam and area close to it. Each consists of more than 8000 scintillating fibers. The produced light is led by optical fibers to 2500 photomultipliers. Due to the high particle flux the reconstruction of tracks uses time rather than spatial correlation. Upstream the target the silicon microstrip detectors are installed. They have wafers with two-sided readout to minimize the amount of material present and a capillary flushed with about 400 l/h of gaseous nitrogen to cool down the front-end chips. [1]

Small area trackers are medium sized detectors for distances larger than 2.5 cm from the beam. Very good spatial resolution, high rates and minimum material budget are required. Three Micromesh Gaseous Structure (Micromegas) stations and eleven Gas Electron Multiplier (GEM) stations serves that purpose. The Micromegas is a gaseous detector developed in Saclay [10], based on a wire chamber. Its installation on COMPASS in 2001 was its first large-scale use. When the particle ionizes gas inside the detector, the ions drift in electric field towards the micro-mesh; in the strong field close to the mesh it gathers enough energy to start an electron avalanche which is detectable by microstrips behind the mesh (see fig. 2.2a). The amplification gap is very narrow ($100 \mu\text{m}$) to allow fast (less than 1 ns) detection. Each Micromegas station consists of four planes and has an area of $40 \times 40 \text{ cm}^2$. Novel "bulk" technique is under study to further improve the performance of Micromegas and to the cover the dead zone in the center ($5 \times 5 \text{ cm}^2$) [14]. This new central elements with pixelized readout further improve the detector performance.

Each GEM station is composed of two detectors and covers an area of $31 \times 31 \text{ cm}^2$. As can be seen from figure 2.1, the Micromegas are placed right behind the target and the GEMs are distributed from SM1 to the end of the hall. In

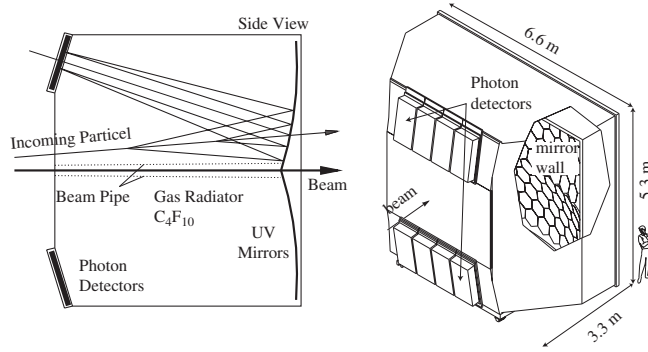


Figure 2.3: RICH detector — schema and artistic view [1].

GEM detectors the two thin metal layers with high voltage in between, deposited on two sides of a isolating foil with holes in it, are used to multiply electrons produced by an ionizing particle (see fig. 2.2b). They were invented at European Organization for Nuclear Research (CERN) in 1997 [43] and COMPASS was one of the first large-scale users. Some of COMPASS members are active in their further development [26]. Five of them have been upgraded in 2007/2008 and have now pixelised readout structure in the center [14]. They are used on the stations closer to the target, because of their smaller size ($10 \times 10 \text{ cm}^2$).

Large area trackers have to provide good spatial resolution on a large area. The gaseous detectors fits best this purpose. The drift chambers (with area about $1.8 \times 1.3 \text{ m}^2$) and "straw" drift tubes (about $3.2 \times 2.7 \text{ m}^2$) are placed upstream and downstream of SM1. Downstream from the RICH follow the Multiwire Proportional Chambers (MWPCs) and drift tube stations. All of the large area trackers have a dead zone in the middle of about 20 cm in diameter to prevent large occupancies [1]. The new drift chambers are planned to replace some large area trackers [40].

Detection of muons is performed by two **muon walls** (MW1, MW2 in LAS, SAS, respectively). They consist of an absorber (MW1 has a 60 cm thick iron wall and MW2 a 2.4 m thick concrete wall) and trackers. They recognize muons from other particles that stop inside the absorbers. Muons go through, because they do not interact via strong force like hadrons and are too heavy to be significantly slowed down by electromagnetic interaction. The MW1 has dedicated drift tubes upstream and downstream the absorber, the muon detection in SAS uses trackers after the SM2 magnet and dedicated drift-tubes stations (MW2) and three stations of MWPCs downstream the absorber.

2.1.3 RICH detector

The RICH detector is used to identify charged hadrons with momenta ranging from a few GeV/c up to $43 \text{ GeV}/c$. It is based on Cherenkov effect — emission of electromagnetic radiation, when a particle passes through a dielectric medium with velocity greater than the phase velocity of light in that medium. The detector consists of a radiative vessel where light is emitted, the reflective surface and photodetectors (see fig. 2.3). The vessel is filled with C_4F_{10} at 1 Pa. It has volume of about 80 m^3 . The transparency of the gas is essential, so the gas has to

be purified regularly. The reflecting system consists of two spherical mirror surfaces of total area larger than 21 m^2 . It reflects the Cherenkov rings towards the photodetectors. The reflective surface is composed of a mosaic of 116 hexagons and pentagons made of borosilicate glass.

The photodetection is now provided by MWPCs equipped with photocathodes, consisting of printed circuit board segmented into $8 \times 8 \text{ mm}^2$ pads coated with CsI film. The Cherenkov photons enter the chamber via quartz window and hit the photocathode. The produced photo-electrons are multiplied in the MWPC. The chamber has to be operated on low gain, because of the presence of sensitive CsI film. The "long" integration time of the original Gassiplex front-end chips of about $3 \mu\text{s}$ caused difficult correlation of Cherenkov rings with individual particles, especially in the center, most occupied, region. The upgrade was made in 2006. The central region (25% of the surface) was instrumented with fast multi-anode photomultipliers, coupled to individual telescopes with fused silica lenses and the MWPCs in the remaining peripheral area were equipped with new readout system based on fast APV chips [14].

In spite of remarkable success of operating this in its time novel system, there are serious problems. The CsI layer suffers from aging in positive ion bombardment in the chamber and the system has a long (about a day) recovery time in case of a detector discharge, so it has to be operated on a low gain. To overcome this limitations a new large-gain system based on Thick GEM (THGEM) electron multipliers [9] coupled to the solid-state CsI photocathodes is being developed. The capton foil (normally about $50 \mu\text{m}$ thick) used on standard GEMs is replaced by a printed circuit board of thickness of 0.4–1 mm. The development is still in progress, the goal is to replace the MWPCs with THGEMs, coupled with the CsI photocathodes, and obtain a better time resolution, more stable operation and higher gain, which would result in larger efficiency of the single photo-electron detection.

2.1.4 Calorimetry

The hadron calorimeters are used to measure energy of particles that interact, passing through a material, mostly via strong force. Both hadron calorimeters (HCAL1, HCAL2) are sampling "shashlik" calorimeters, they consist of alternating stacks of iron, in which particle showers are produced, and scintillator plates, which measure the showers. The HCAL1 has a modular structure, each module is formed by 40 layers of iron and scintillator plates, 20 and 5 mm thick, respectively. The total thickness is equivalent to 4.8 nuclear interaction lengths. There are 480 such modules assembled in a matrix with a hole in the middle to left particles at low angles pass to SAS. The scintillators have been produced by molding under pressure from granulated polystyrene PSM-115 mixed with P-terphenyl (1.5%) and POPOP (0.04%) [1]. The light from scintillators is collected by a single flat wavelength-shifting light guide made of an organic glass and led to the photomultiplier. The system is able to get enough light to produce 4–6 photoelectrons on the photocathode (which are enough to be detected) from one minimum-ionizing particle crossing one scintillator. The stability during data-taking is monitored by Light Emitting Diode (LED) system. The light of a single LED is collected and distributed to all modules using optical fibers. The energy resolution for

pions was measured to be $\sigma(E)/E = (59.4 \pm 2.9)\%/\sqrt{E} \oplus (7.6 \pm 0.4)\%$ with E in units of GeV. [1]

The HCAL2 has a form of a matrix of 22×10 elements with hole of 2 elements in the middle to pass the high-intensity beam. The overall thickness of modules is 5 nuclear interaction lengths for pions and 7 for protons. The readout of scintillating plates is done with wavelength-shifting fibers. The light is detected in photomultipliers. Small fraction of signal from photomultipliers can be fed to fast summation system for trigger purposes. The calorimeter has a LED monitoring. The energy resolution is $\sigma(E)/E = (66/\sqrt{E} \oplus 5)\%$ for pions. [1]

The electromagnetic calorimeters detect particles interacting in matter electromagnetically, mostly electrons and photons. COMPASS has two of them, ECAL1 and ECAL2. ECAL1 consists of lead-glass modules, which serve both to produce showers and to detect them. The high-energy electron or gamma start an electromagnetic shower in the lead glass. The electrons and positrons in shower produce Cherenkov radiation on their way, which is detected. The amount of light is proportional to the deposited energy. The light is detected by photomultipliers located on one side of each block.

There are about 3000 modules of $38 \times 38 \text{ mm}^2$ in the central part; they had been originally used in GAMS-4000 spectrometer, but the readout system was upgraded for COMPASS. The peripheral part is covered by larger $14.3 \times 14.3 \text{ cm}^2$ Olga modules.

The ECAL2 is composed of various types of modules with various sizes. There are, going from the centre, shashlik modules (also $38 \times 38 \text{ mm}^2$), radiation-hardened GAMS modules, normal GAMS modules and larger Mainz modules ($75 \times 75 \text{ mm}^2$). The radiation hardness in the central part is essential due to large particle fluxes. There are some exchanges of modules between the calorimeters and additions of new modules proposed to improve the performance of the system. [14]

2.1.5 Data acquisition system

The basic principle of the Data Acquisition (DAQ) is the same regardless of the scale of the experiment. There have to be a trigger, that sends signal to take measurement (in many experiments the trigger is just a clock). The data are processed (at least digitized, often also involves basic checks) and finally stored. In high energy physics the attention is often turned to rare processes, implying high particle fluxes have to be employed and triggers have to filter out as much uninteresting data as possible and have to do it very fast. Even if that is accomplished, very large amount of data is taken and its processing and storing is challenging.

The readout of data from detectors is performed by frontend electronics. It has to be very fast to cope with high data rate. The radiation hardness is also often required on COMPASS. The triggers consist of fastest detectors and electronics (usually programmable boards) available, but still there is some delay. Thus the analog data from detectors first go to analog buffers, which delay the signal long enough for trigger to determine whether to record data or not. Then analog-to-digital conversion and preprocessing are performed. There are about 250 000 detector channels on COMPASS. Data from multiple channels are assembled by

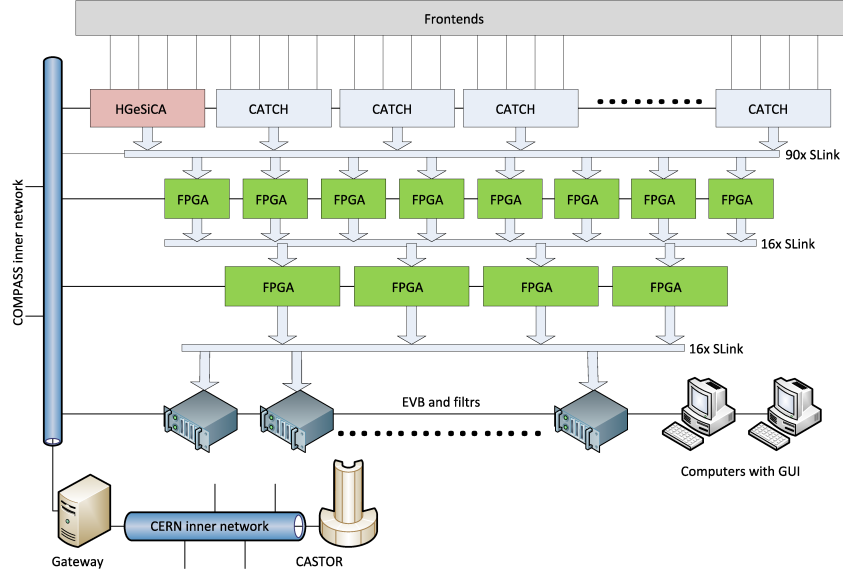


Figure 2.4: New DAQ hardware [38].

modules called CATCH and GeSiCA. They are connected to trigger and timing systems and they label the data with timestamps and event identification. The created data structures are called subevents. [38]

Subevents are transferred by optical S-link bus to readout buffers. Presently they are standard servers with a custom PCI cards called spillbuffers. These cards allow to hold the subevents and distribute their further processing over the whole period of SPS supercycle¹. The subevents are then send via Gigabit Ethernet to the event builders, which assemble them and form whole events and transfers them via CERN network to the permanent storage at the Castor tape system.

The data acquisition is presently performed, controlled and monitored by Data Aquisition and Test Environment (DATE) software that has been adapted from ALICE experiment. It is very flexible and scalable system. It can run on hundreds of computers as well as on a few. Though it did its work well, the new system is being developed to fit the DAQ hardware upgrade which is being prepared.

The frontend electronics should be more or less the same, but the following layer will be replaced by two layers of Field Programmable Gate Arrays (FPGAs). This devices has programmable interconnections between logical units and are ideal for high-rate data processing, because they offer so called real-time operation². The hardware-based event building should be more reliable and faster [35].

The new software which is being developed [38] will secure configuration of the hardware, monitoring of the data taking and its own operation, control of the hardware (giving commands to FPGAs) and control of the data flow. The Distributed Information Management (DIM)³ library will be used for communication between processes. It should provide more user-friendly and customizable

¹The spill itself is about 10 s long while the supercycle length varies through years around 30–50 s to fit the needs of various experiments.

²Real-time system has to guarantee response within a time constraint.

³Develpedn in CERN. See [24].

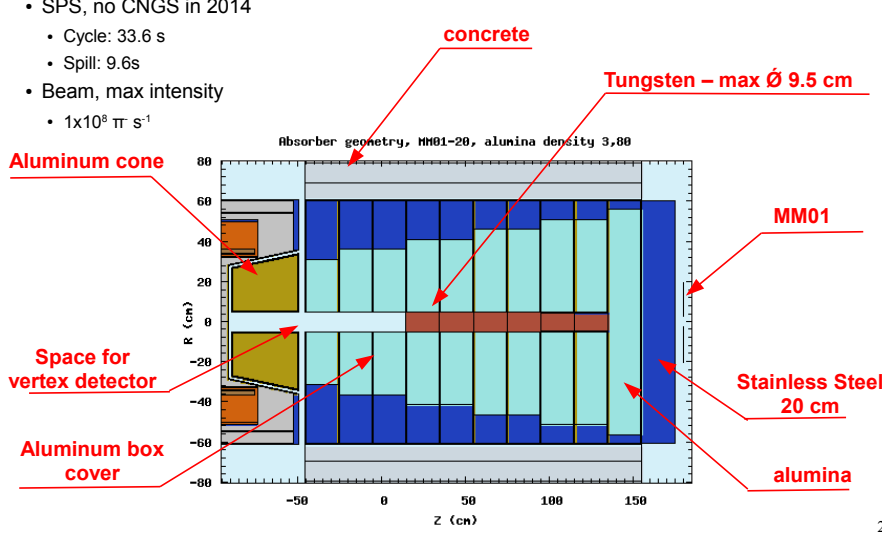


Figure 2.5: Hadron absorber schema [36]. The aluminium cone will be plugged into a hollow at the back of the target magnet.

interface for operators, detector experts and DAQ experts.

2.1.6 Detector control system

On experiment like COMPASS there are many various detectors and other systems, which need monitoring and control. Some systems are very sensitive or potentially dangerous like detectors using flammable gases and the experienced experts can not be present during whole data-taking, which runs 24 hours a day if all works well. If something fails, tracing errors back in time to discover the cause is necessary.

The Detector Control System (DCS) takes care of these tasks. It gathers information about detectors and other equipment and stores them in the database. It has a graphical user interface where the gathered parameters can be checked and their history can be plotted. The system periodically checks if the parameters are in given limits. If some limit is exceeded, the DCS warns the shift crew with an alarm. The system recognizes various users with different privileges and can be accessed remotely. The system uses commercial supervisory controls and data acquisition system called PVSS, which is widely used in big experiments. The devices communicate with the PVSS through OPC servers or they use SLIC package and communicate via DIM server. [16]

2.1.7 Drell–Yan experimental setup

As was stated before, at COMPASS the DY reaction will be studied on negative-pion beam and polarized proton target. The beam momentum will be 190 GeV/c (see section 2.2). The pion beam is produced from SPS 400 GeV/c proton beam in a Be target. The beam contains a small contamination of other particles⁴.

⁴About 2% of kaons and less than 1% of \bar{p} and of μ [40].

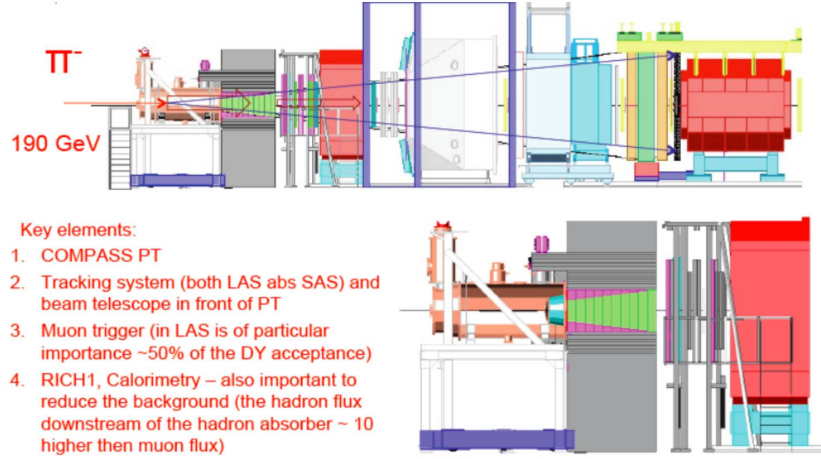


Figure 2.6: Spectrometer setup for Drell–Yan [17]. Note the hadron absorber downstream of the target.

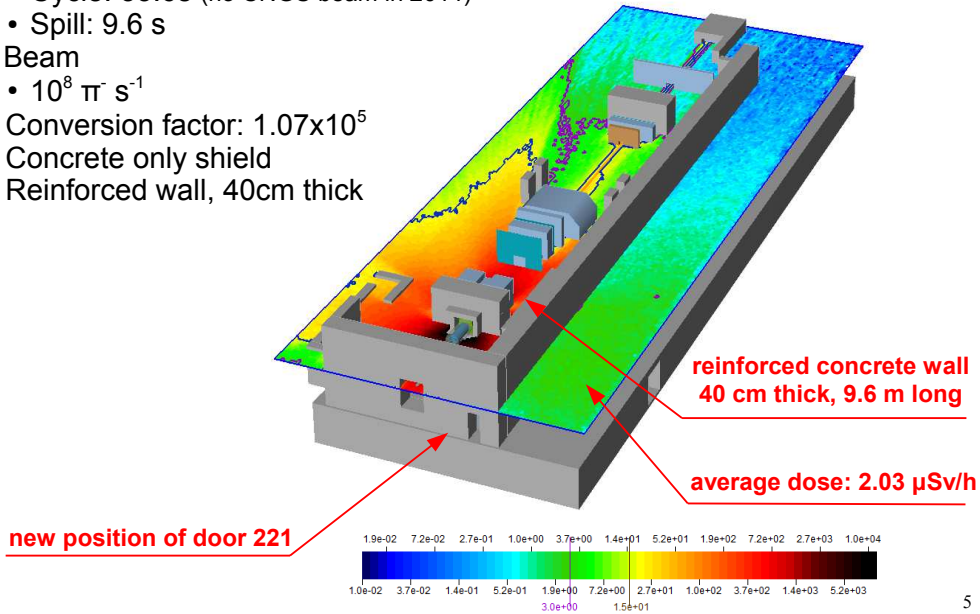
For the Drell–Yan program some changes in the experimental setup with respect to the layout shown on fig. 2.1 will be done. The most noticeable will be mounting of a **hadron absorber** right after the target to stop the beam and hadrons produced in the target and lower the occupancies of trackers. Detection of the muons from DY reaction, which should pass mostly intact, will be thus easier.

The decision of building a hadron absorber was taken after tests in 2007 and 2008. The two criteria have to be followed: The number of interaction lengths crossed by hadrons have to be maximized in order to stop them, while the radiation length has to be minimized in order to have minimal energy loss and multiple scattering of the muons. The experience from past Drell–Yan experiments in CERN was taken into account⁵ [14], simulations have been run. There was a test with model absorber in 2009. The occupancies of detectors have been lowered satisfactorily [14]. The final design is shown on figure 2.5 and its position on figure 2.6. The beam itself will be stopped inside a tungsten "beam plug". Before the beam plug there is a hole (filled only with air) to minimize back-scattering of the beam particles into the target volume. The absorber will have a concrete and steel radiation shielding, which will reduce the radiation from the absorber material, activated by the beam. Additional shielding concrete blocks will be placed around to protect the target electronics and lower the radiation dose in the hall.

The hadron absorber has also a negative effect. The multiple scattering of DY dimuons in it will make vertex reconstruction less accurate. Thus there will be increased "migration" of events from one target cell to another, which will result in smaller asymmetries. This systematical error should be minimized. One precaution is that the gap between the target cells will be increased to 20 cm. The second measure will be installation of **additional tracking station** between the target and absorber, which should improve the resolution of the vertex reconstruction by a factor of about five [14]. This task will be secured by

⁵Especially the hadron absorber of NA50, where the conditions were found in some way similar.

- SPS
 - Cycle: 33.6s (no CNGS beam in 2014)
 - Spill: 9.6 s
- Beam
 - $10^8 \pi^- \text{ s}^{-1}$
- Conversion factor: 1.07×10^5
- Concrete only shield
- Reinforced wall, 40cm thick



5

Figure 2.7: Radiation dose in the experimental hall in Drell–Yan run, simulated by FLUKA [36]. The wall dividing the hall into the experimental zone and the area with control room and barracks should be reinforced in critical part. Behind the wall target, shielding of the absorber, spectrometer magnets and some detectors are visible. The lines on scale mark 3 and 15 $\mu\text{Sv}/\text{hour}$

scintillating-fibers station, which will be mounted in the 5 cm gap between the absorber and the aluminium cone. The detector is being developed [4].

The hadron beam of a high intensity about 6×10^8 hadrons per SPS super-cycle⁶, planned for DY program, in combination with the beam plug are conditions that will exceed the limits given by the Radiation Protection Committee at COMPASS commissioning. The test in 2009 with beam of about 1.5×10^8 pions per supercycle showed indeed **increased radiation dose** in the hall. The radiation levels have been calculated with Monte Carlo particle transport code FLUKA and compared to those measured during the beam tests. Excellent agreement was achieved⁷, permitting to use the simulation to determine the dose in real operation with 6×10^8 pions per spill [14]. Not only particles penetrating the wall, but also those reflected by the roof have to be taken into account.

The areas of special interest are the present control room, DAQ and other experimental barracks, pathways and also the target platform because of the electronics present. The experimental barracks and control room are presently protected by a 160 cm thick and 6.4 m high concrete shielding wall. The shielded part of the hall is classified according to CERN’s standards as a ”supervised radiation area”⁸.

⁶Which is about 10 s long, implying $6 \times 10^7 \text{ s}^{-1}$.

⁷Actually, the calculated doses were about 30% higher, so there is some safety margin.

⁸This classification requires the ambient dose equivalent rate not to exceed 3 $\mu\text{Sv}/\text{hour}$ in permanently used areas and 15 $\mu\text{Sv}/\text{hour}$ in low occupancy areas (corridors, stairways).

The simulation showed this limit will not be exceeded, if some measures are adopted [36]. The door to experimental area should be moved and wall reinforced in critical part next to the target by additional 40 cm of concrete. Though the equivalent dose will remain under the limit, it was decided, applying the As Low As Reasonably Achievable (ALARA) approach, to move the control room to the office building and **control the experiment remotely**. The remote operation brings challenges for the DAQ system as well as for the DCS. The integration of polarized target instruments into the DCS will be discussed in the chapter 3 and 4.

The study of radiation from activated materials on the experimental zone have been done too. After one year of data taking the material of absorber and around it will be activated. Simulation shows, that entering the area is safe after less than one hour after switching off the beam. Only the area near the absorber should be accessed with limitations [36].

Besides the polarized DY program there is a possibility to study unpolarized DY nuclear effects by insertion of a thin nuclear target in the region upstream of the beam plug [40].

2.2 Kinematic domain and spectrometer acceptance

The acceptance of the COMPASS spectrometer for Drell–Yan events with $\mu^+\mu^-$ pairs in the final state was investigated in the invariant-mass intervals 2–2.5 GeV/ c^2 and 4–9 GeV/ c^2 using a Monte Carlo simulation. The range of large combinatorial background below and the range of J/ψ , ϕ and Υ between the intervals were excluded (see figure 2.8 with background processes). The event generation in simulation was based on PYTHIA 6.2 generator and the simulation of spectrometer response was done using COMGEANT, the COMPASS Monte Carlo simulation program based on GEANT 3.21. [14]

The probability density functions of the sea quarks fall steeply with increasing Bjorken x . When both x_π and x_p , the fractions of beam pion and target proton momenta carried by the quark or antiquark, is greater than 0.1, the valence quark contributions are dominant. In order to be sensitive to the transverse polarization of the target proton one should stay in this region. Considering the quark content of π^- and p we learn the DY proceeds via annihilation of u quark from the proton and \bar{u} from the beam pion. The beam momentum 190 GeV/ c was chosen as a compromise between sufficient cross section in the 4–9 GeV/ c^2 range to obtain reasonable statistics and staying in the valence region [14]. The phase space for the DY process in the upper dimuon mass range for the CMS energy squared 357 GeV², corresponding to the beam momentum 180 GeV/ c , is shown on figure 2.9a.

The spectrometer is capable to detect muons with angles 18–180 mrad [40]. The muon pair is counted as being in the spectrometer acceptance if it is detected at least by one of the two muon filtering systems. This means at least 5 hits in the second station of MW1 or 7 hits in MW2 or 5 hits in MWPCs behind the MW2. The geometrical acceptance is a ratio between the number of event inside the spectrometer acceptance to the total number of generated events in the same

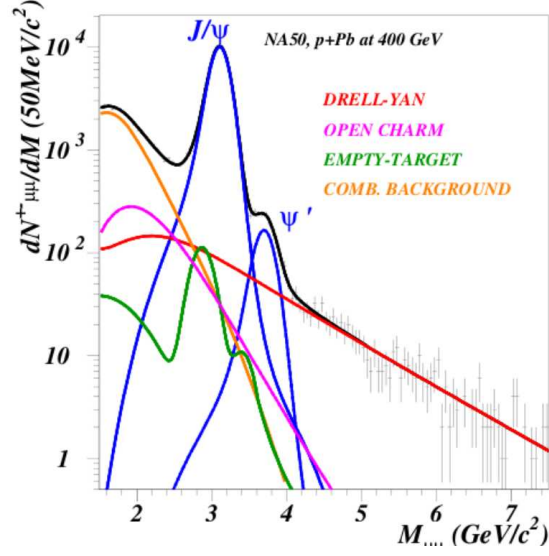


Figure 2.8: Drell–Yan and major background processes contributing to the total cross section [40]. Combinatorial background will be suppressed by the hadron absorber. The picture shows why regions 2–2.5 GeV/c², J/ψ and 4–9 GeV/c² are discussed separately.

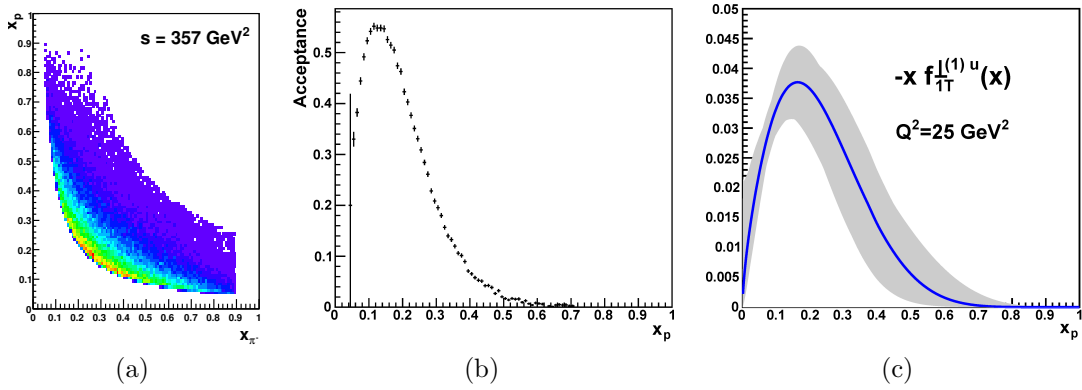


Figure 2.9: (a) Phase space for Drell–Yan process in mass range 4–9 GeV/c² with beam momentum 180 GeV/c. (b) COMPASS acceptance as a function of x_p . (c) The first \vec{k}_T -moment of the presumed u -quark Siverts function. Source: [14]

kinematic window. The average geometrical acceptance was found to be 43% and 35% in the mass ranges 2–2.5 GeV/ c^2 and 4–9 GeV/ c^2 , respectively [14]. The acceptance as a function of x_p of the u -quark from target proton is compared to the expected first \vec{k}_T -moment of the Siverts function on the figures 2.9b and 2.9c. We can see that its value is expected to be largest where the acceptance is largest. In the lower dimuon invariant mass region is the situation similar, but the acceptance falls more steeply with x_p .

2.3 Expected event rate and precision

2.3.1 Expected rate of Drell–Yan events

The instantaneous luminosity for target experiment is given as

$$\mathcal{L} = L_{\text{eff}} \frac{\rho F_P N_A}{A_{\text{eff}}} I_{\text{beam}}, \quad (2.1)$$

where N_A is Avogadro constant. Definition of the other parameters and their values in case of COMPASS are stated in table 2.1. The effective target length is defined by the formula [11]

$$L_{\text{eff}} = \frac{\lambda_{\text{int}}}{\rho F_P} \left[1 - \exp \left(- \frac{L_{NH_3} \rho F_P}{\lambda_{\text{int}}} \right) \right], \quad (2.2)$$

where L_{NH_3} is target material length (2 cells, 55 cm each) and λ_{int} is interaction length, which is 114.81 g cm⁻² for ammonia [11]. Packing fraction F_P is fraction of volume occupied by the target material, which has a form of irregular pieces of 3–4 mm diameter. The packing fraction was assumed as 0.5, according to the 2007 measurement [11].

If the target material was elemental material (e.g. pure hydrogen) there would be mass number A of the element in denominator of equation (2.1). The effective mass number A_{eff} and atomic number Z_{eff} take into account that ammonia is a molecule. They are defined as [11]

$$A_{\text{eff}} = \frac{\sum_i n_i A_i^2}{\sum_j n_j A_j}, \quad Z_{\text{eff}} = \frac{\sum_i n_i Z_i^2}{\sum_j n_j Z_j}, \quad (2.3)$$

where n_i is number of atoms of i -th element in molecule and A_i is its mass number. The stated values lead to an expected luminosity of $\mathcal{L} = 1.18 \times 10^{32} \text{ cm}^{-2}\text{s}^{-1} = 118 \mu\text{b}^{-1}\text{s}^{-1}$.

The Drell–Yan cross sections in the two dimuon invariant mass regions and for different momenta of the negative-pion beam were calculated using the PYTHIA generator [14]. The cross sections for pion-proton and pion-neutron interactions were calculated⁹. The cross section for ammonia was obtained from their combination

$$\sigma_{\pi^-NH_3}^{\mu\bar{\mu}} = Z_{\text{eff}} \sigma_{\pi^-p}^{\mu\bar{\mu}} + N_{\text{eff}} \sigma_{\pi^-n}^{\mu\bar{\mu}}, \quad (2.4)$$

where Z_{eff} is effective atomic number, defined in equation (2.3), and N_{eff} the effective neutron number $N_{\text{eff}} = A_{\text{eff}} - Z_{\text{eff}}$. For the π^- momentum 190 GeV/ c

Parameter	Explanation	COMPASS value
L_{eff}	Effective target length (see eq. (2.2))	90.36 cm
ρ	Target material (ammonia) density	0.85 g cm ⁻³
F_P	Target material packing fraction	0.5
A_{eff}	Effective mass number of NH ₃ (see eq. (2.3))	11.71 g mol ⁻¹
I_{beam}	Beam intensity	6×10 ⁷ s ⁻¹
\mathcal{L}	Instantaneous luminosity	118 μb ⁻¹ s ⁻¹
$\sigma_{\pi^-\text{NH}_3}^{\mu\bar{\mu}, \text{low}}$	Cross section for inv. mass 2–2.5 GeV/ <i>c</i> ²	6.231 nb
$\sigma_{\pi^-\text{NH}_3}^{\mu\bar{\mu}, \text{high}}$	Cross section for inv. mass 4–9 GeV/ <i>c</i> ²	1.291 nb
K_{DY}	Correction for σ_{DY} from PYTHIA	2
d_{spill}	Duration of the SPS spill	9.6 s
n_{spill}	Maximal number of SPS spills per day	1800 day ⁻¹
Ω	Spectrometer acceptance (average)	0.4
E_{rec}	Efficiency of event reconstruction	0.8
E_{trig}	Trigger efficiency	0.81
E_{SPS}	Accelerator efficiency	0.8
E_{spec}	Spectrometer availability	0.85
E_{tot}	Total efficiency of the measurement	0.17
R_D^{low}	Event rate for inv. mass 2–2.5 GeV/<i>c</i>²	4858 day ⁻¹
R_D^{high}	Event rate for inv. mass 4–9 GeV/<i>c</i>²	809 day ⁻¹

Table 2.1: Estimate of experimental factors affecting event rate [14, 11].

were cross sections in two invariant-mass regions found to be: $\sigma_{\pi^-\text{NH}_3}^{\mu\bar{\mu}, \text{low}} = 6.231$ nb for the range 2–2.5 GeV/*c*² and $\sigma_{\pi^-\text{NH}_3}^{\mu\bar{\mu}, \text{high}} = 1.291$ nb for the range 4–9 GeV/*c*² [14].

As is known from 1980's, the leading-order Drell–Yan cross section calculated in PYTHIA is smaller than the experimental value by so-called K_{DY} factor. This factor is about two. So the calculated cross sections have to be multiplied by this factor. In reference [11] was the calculated cross section compared to that measured for unpolarized DY on experiment NA10 and good agreement was found.

It is important to note that only the hydrogen atoms are polarized and thus only fraction of DY events contribute to asymmetries. The DY processes on protons and neutrons from nitrogen nucleus are background events, which can not be separated on event-by-event basis. This fact will be treated in the section 2.3.2.

The event rate per day is given as

$$R_D = \mathcal{L} \sigma_{\pi^-\text{NH}_3}^{\mu\bar{\mu}} K_{DY} d_{\text{spill}} n_{\text{spill}} E_{\text{tot}}. \quad (2.5)$$

The used parameters are summarized in the table 2.1. The E_{tot} is the total efficiency of the measurement, given as

$$E_{\text{tot}} = \Omega E_{\text{rec}} E_{\text{trig}} E_{\text{SPS}} E_{\text{spec}}. \quad (2.6)$$

The spectrometer acceptance Ω and the efficiencies of all stages of detection of events used in the calculation are stated in table 2.1. The trigger efficiency

⁹It was found that $\sigma_{\pi n}^{\mu\bar{\mu}} \approx 2\sigma_{\pi p}^{\mu\bar{\mu}}$, which is easily understood considering the quark contents.

for detecting single muon is 0.9, implying 0.81 for dimuon. The spectrometer availability includes trigger dead time, the run start-stop procedure and DAQ availability.

The equation (2.5) in combination with values from table 2.1 imply Drell–Yan event rates $R_D^{\text{low}} = 4858/\text{day}$ for invariant mass range 2–2.5 GeV/ c^2 and $R_D^{\text{high}} = 809/\text{day}$ for 4–9 GeV/ c^2 .

2.3.2 Expected statistical precision for asymmetries

As is shown in [34], the simple estimate of statistical errors of asymmetries in leading order can be done if we assume flat spectrometer acceptance in azimuthal angles ϕ , ϕ_S and $\cos \theta$. By integrating the equation (1.44) over photon transverse momentum q_T and lepton polar angle θ and performing Fourier projection on modulation, corresponding to an asymmetry, we can separate that asymmetry from the measured cross section. We find for example

$$A_T^{\sin \phi_S}(x_\pi, x_p) = \frac{2}{f|\vec{S}_T|} \frac{\int d\phi_S d\phi \frac{dN(x_\pi, x_p, \phi, \phi_S)}{d\phi_S d\phi} \sin \phi_S}{N(x_\pi, x_p)}, \quad (2.7)$$

and similarly for other asymmetries. $N(x_\pi, x_p)$ is the total number of events in bin (x_π, x_p) , $|\vec{S}_T|$ the transverse polarization and f dilution factor, which takes into account fraction of polarizable nuclei in the target material (see the chapter 3). The statistical accuracy is then given as

$$\delta A_T^{\sin \phi_S}(x_\pi, x_p) = \frac{1}{f|\vec{S}_T|} \frac{\sqrt{2}}{\sqrt{N(x_\pi, x_p)}}. \quad (2.8)$$

In the estimation $|\vec{S}_T| = 0.9$ and $f = 0.22$ were used. The statistical errors for accessible asymmetries were calculated for beam momentum 190 GeV/ c and in three invariant mass regions — two clear ones and a middle including J/ ψ (see section 1.3.5), where the ratio of J/ ψ ’s produced by $q\bar{q}$ process was assumed 60%. Results are stated in table 2.2. Results were compared with theoretical predictions [14]. It was found, that COMPASS results can be precise enough to be compared with these predictions. Example is shown on figure 2.10.

Feasibility of the experiment was proven in beam tests in 2007, 2008, 2009 [14, 40] and 2012 [17]. The target cooling system should give enough cooling power to withstand the large hadron flux. The hadron absorber enables to reach reasonable occupancies and the vertex-reconstruction precision remains on sufficient level of accuracy to distinguish the target cells. The Monte Carlo simulations were compared with beam-tests results and good agreement was found.

The conclusion is the experiment should be able to deliver first experimental results of polarized Drell–Yan scattering, to extract transversity and pretzelosity of proton and to check the sign reversal property of the Sivers function (see section 1.3.4).

Asymmetry	Dimuon invariant mass [GeV/ c^2]		
	2–2.5	J/ ψ region	4–9
$\delta A_U^{\cos 2\phi}$	0.0026	0.0014	0.0056
$\delta A_T^{\sin \phi_S}$	0.0065	0.0036	0.0142
$\delta A_T^{\sin(2\phi+\phi_S)}$	0.0131	0.0073	0.0284
$\delta A_T^{\sin(2\phi-\phi_S)}$	0.0131	0.0073	0.0284

Table 2.2: Statistical-error estimate for accessible asymmetries [40].

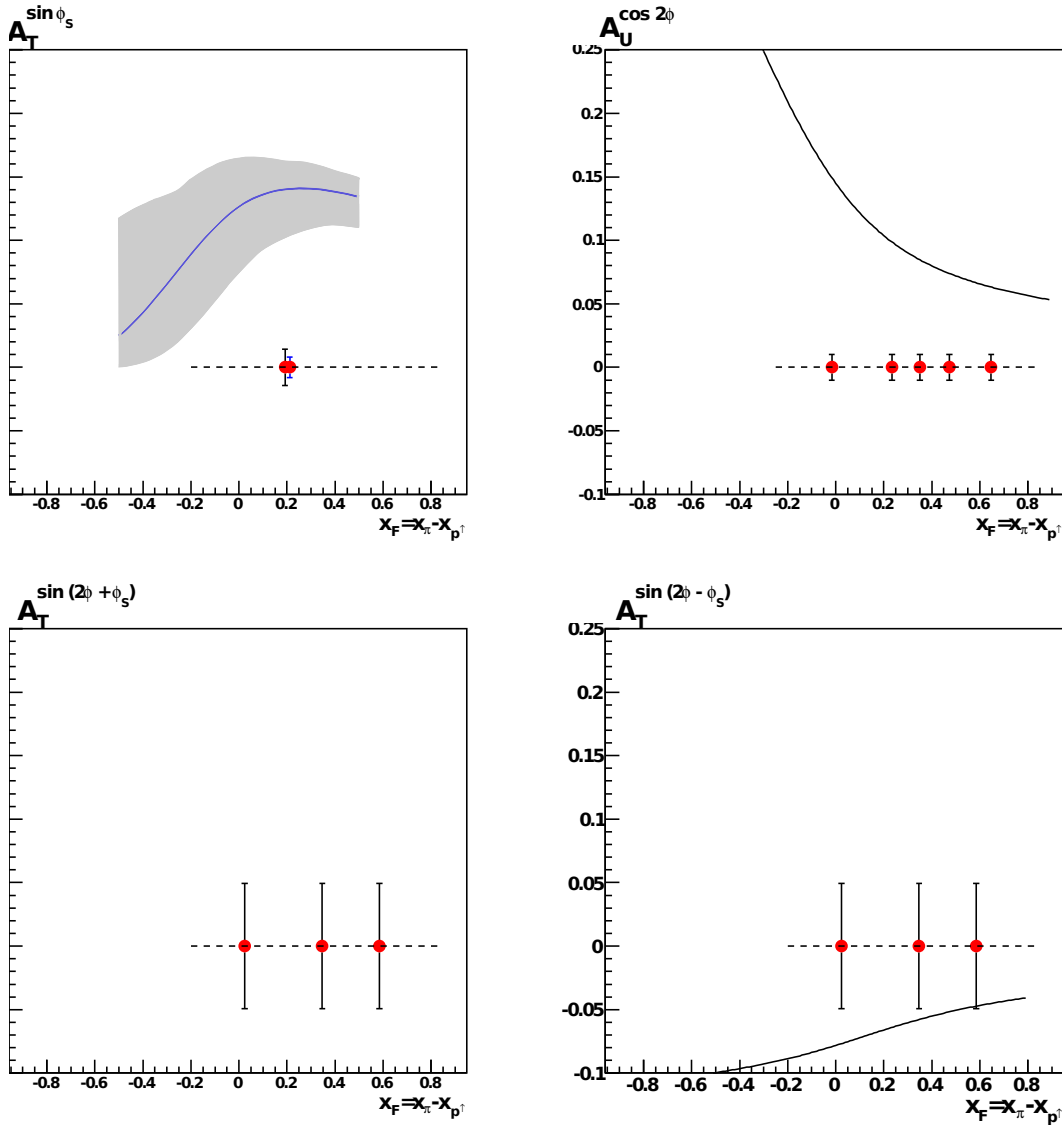


Figure 2.10: Theoretical predictions for Siverts (top-left), Boer–Mulders (top-right), $\sin(2\phi + \phi_S)$ (bottom-left), and $\sin(2\phi - \phi_S)$ (bottom-right) asymmetries for a DY measurement in dimuon invariant mass region 4–9 GeV/ c^2 . [14, 40]

3. COMPASS polarized target

3.1 Introduction to the polarized target

3.1.1 Demands on polarized targets in particle physics

From expression for statistical error of the asymmetry (2.8) we can see that it is inversely proportional to the dilution factor, transverse polarization and square root of the total number of Drell–Yan events. As can be seen from equations (2.5) and (2.1), the number of collected DY events is proportional to the target material density and packing fraction. Overall, the statistical uncertainty δA of an asymmetry is proportional to

$$\delta A \sim \frac{1}{\sqrt{F_{oM}}}, \quad F_{oM} = f^2 P^2 \rho F_P \quad (3.1)$$

for a given data taking time. We defined so called "figure of merit" F_{oM} , which characterizes the polarized target. Equation (3.1) can be alternatively seen as follows: If we demand certain level of statistical accuracy, the figure of merit is inversely proportional to the data taking time needed. P is polarization (fraction of polarized nuclei from all polarizable nuclei), ρ is density of the target material, F_P is its packing fraction (the fraction of the target volume occupied by the target material) and f is dilution factor, the fraction of events scattered off the polarized nucleons under study. We can calculate it as a molar concentration of the nuclei under study, weighted by cross section of the studied reaction [3]

$$f = \left(1 + \sum_A \frac{n_A \sigma_A}{n_p \sigma_p} \right)^{-1}, \quad (3.2)$$

where $n_{A,p}$ is the number of nuclei and $\sigma_{A,p}$ is the unpolarized cross section of the studied reaction on nucleus of element with atomic weight A or of ^1H .

We can see that polarization and dilution factor are essential for the minimization of the statistical uncertainties and density and packing fraction are important players too. The polarized target should be also the longest possible (in terms of interaction length) to improve the statistics, because the measured events are very rare. The experiment requires **long, solid target with high degree of polarization**.

3.1.2 Solutions used on COMPASS

The nuclear paramagnetism is very weak and nuclear spins, unlike the electron moments, does not reach significant polarization even in the high magnetic fields and very low temperatures¹. The technique of Dynamic Nuclear Polarization (DNP) is used instead on polarized targets. The method requires temperatures in order of 10^{-1} K and homogeneous and strong magnetic field. The microwaves are used to polarize unpaired electronic spins to a high degree and

¹The ^1H nuclei in NH_3 reach polarization about 0.25% in 2.5 T magnetic field at 1 K [29], see the section 3.3

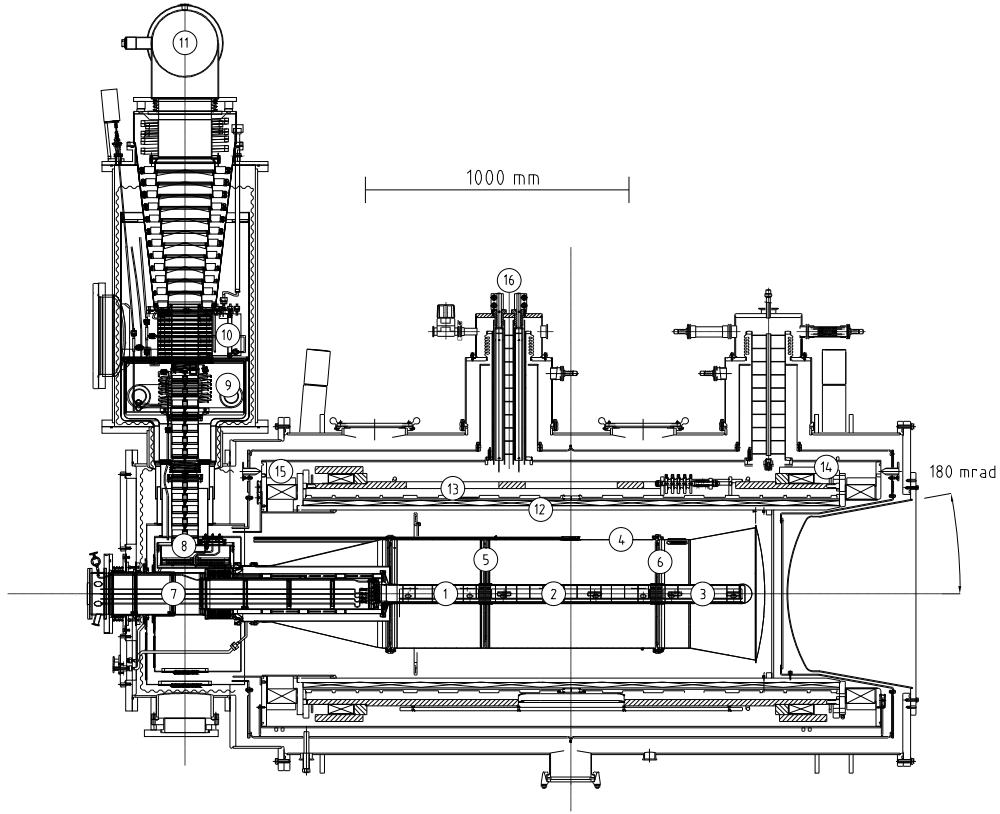


Figure 3.1: Side view of the COMPASS polarized target system (2009): (1,2,3) Upstream, middle, downstream target cell (setup from the muon run, there will be two cells for Drell–Yan), (4) microwave cavity, (5,6) microwave stoppers, (7) target holder, (8) still (^3He evaporator), (9) ^4He evaporator, (10) ^4He gas/liquid separator, (11) ^3He pumping port, (12) solenoid magnet, (13) correction coils, (14) dipole coil, (15) solenoid end compensation coil and (16) magnet current leads. [31]

transfer the polarization to the nuclei (see section 3.3). Polarizations close to 100% are achievable using this method.

Such a strong and homogeneous magnetic field in transverse direction is difficult to achieve, since the target is long. The different strategy is used instead. The target is placed inside a dilution refrigerator, which provides enough cooling power to keep temperature of the target well below 1 K when microwaves are in operation and to cool it rapidly down below 100 mK when they are switched off (see section 3.2). The magnetic field for polarization procedure is provided by 2.5 T superconducting solenoid. After the polarization is build-up the solenoid is slowly ramped down and an additional 0.6 T superconducting dipole with a saddle-type coil is used to rotate the spins in transverse direction. At temperatures about 70 mK the relaxation times of nuclear spins are long enough² to enable measurement with transverse polarization. The operation without microwaves is called "frozen-spin mode". In addition, the combination of two perpendicular

²about 4000 h for ammonia in the 0.6 T field [19]

fields enables relatively fast rotation of spins about 180° (a few tens of minutes).

The asymmetries cannot be reliably extracted from consecutive measurements of the same target with opposite polarizations because of variations of relative beam flux, which cannot be controlled with high enough accuracy. Therefore two target cells in line along the beam labeled "upstream" and "downstream" with opposite polarizations are used. The two cells have to be separated with a suitable distance to allow reliable identification of events coming from each cell. There is an unknown difference in spectrometer acceptance for the two cells. The solution is to perform polarization reversals (by a field rotation) periodically.

The polarization of the target have to be known accurately in order to determine asymmetries. The measurement of polarization in the whole target volume is challenging. The system of 10 Nuclear Magnetic Resonance (NMR) coils is used. Much attention have to be paid to the design of the system and to the analysis of the NMR signals (see the section 3.4).

3.1.3 Outline of the polarized target

The side view of the COMPASS polarized target system is shown on figure 3.1. The figure depicts the setup used in 2009 in muon program. The new target cells and microwave cavity will be used for Drell–Yan in order to cope better with heat load from the hadron beam and enable reliable vertex reconstruction, which is more difficult with hadron absorber (see section 2.1.7). The pair of cells will be used, instead of a trio.

The beam enters from the left-hand side of the picture through thin (0.1 mm) stainless steel windows. Each of the two target cells will be 55 cm long and the cells will be separated by 20 cm gap. The cells are placed inside the glassfiber-reinforced epoxy mixing chamber of the refrigerator. Around it there is a copper microwave resonance cavity for the polarization. It is divided into two parts by a microwave stopper to enable operation at different frequencies in upstream and downstream cells, which is necessary to obtain opposite polarizations. The cavity is placed in vacuum and surrounded by the cryostat and the magnet system. Special attention was paid to minimalization of the amount of material in the downstream end of the cryostat. The large inner diameter of the magnets enable spectrometer angular acceptance of 180 mrad.

3.2 Dilution refrigerator

Dilution refrigerator is the only way to achieve high cooling power in temperatures of about 10^{-1} K, when the microwaves are in operation, and very low temperatures of about 60 mK, when in frozen spin mode. The dilution refrigerator used by COMPASS was originally build for the SMC (1993–1996). The main changes done by the COMPASS collaboration were in the computer interface.

3.2.1 Cooling by dilution of ^3He in ^4He

Helium is the lightest of the noble gases. Two stable isotopes of helium can be found in nature — ^4He and ^3He . The latter is very rare, with natural abundance of about 1 atom per 10 000 atoms of ^4He and is obtained mainly from nuclear

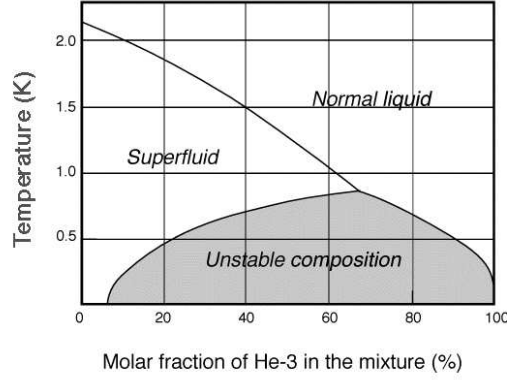


Figure 3.2: The phase diagram of ^3He - ^4He mixture [45]. The diagram corresponds to saturated vapor pressure.

decay of ^3H , produced as a byproduct at nuclear facilities. Both isotopes of helium have the lowest boiling points of all known substances, being 4.215 K for ^4He and 3.19 K for ^3He [44]. Their behaviour is very close to that of the ideal gas at normal temperatures, but at low temperatures, below the boiling points, their properties start to be exotic and cannot be described in terms of classical physics.

The two significant features of both of them is absence of a triple point and a superfluidity. The first can be described as a result of zero-point oscillations, which are large for light helium atoms, and weak van der Waals interaction, which is the only attractive force available for helium. The result is that helium does not form a solid unless under high pressure (in order of MPa). The latter is even more interesting. The ability of superfluid helium to pass without friction through narrow capillaries and its other unique properties have attracted much attention in the past, and many open questions remain. Note, that ^4He , with its two protons and two neutrons, is a boson, and ^3He a fermion. This implies that the mechanism of the superfluidity differ for them. Also the temperatures of the superfluid phase transitions are very distinct, being about 2.2 K for ^4He (called λ -transition) and about 1 mK for ^3He . [44]

The mixture of liquid ^3He and ^4He is even more interesting phenomenon than the two 'quantum liquids' alone, because its constituents obey different quantum statistics. The mixture is characterized by dimensionless parameter x , which is the molar concentration of ^3He in the mixture. The phase diagram of the mixture is shown on figure 3.2. Note that there is a forbidden region in which the composition spontaneously separates into a ^3He -concentrated and ^3He -diluted phases. Due to the lower atomic weight the concentrated phase floats on the diluted phase. In the limit of zero temperature the diluted phase contains about 6% of ^3He , while the concentrated phase becomes pure ^3He . The temperature of λ -transition of ^4He in the mixture depends on x .

The phase separation is caused by the fact that atoms of ^4He interact much more among themselves and with the vessel than with atoms of ^3He , so they leave the concentrated phase as the temperature goes down. On the other hand the Fermi-Dirac statistics do not let atoms of ^3He approach zero energy at zero temperature and forces them to stay in the diluted phase. The ^3He in both the

concentrated and the diluted phase can be described as a Fermi liquid. The ^4He plays role of physical vacuum for the ^3He atoms. The lower concentration of ^3He implies lower Fermi energy of the diluted phase. The equilibrium is reached when the Fermi energy equals the latent heat needed for ^3He atom to cross the phase boundary.

Outside the forbidden region on phase diagram 3.2 the thermodynamic variables pressure P , temperature T and x are independent. But if the mixture gets to the forbidden region, e.g. by cooling, two phases are formed. The Gibbs phase rule restricts the number of independent variables. At a constant pressure, the temperature becomes function of ^3He concentration. This fact provides an efficient cooling mechanism.

The principle of the cooling is similar to that by the evaporation. If atoms of ^3He are forced to cross the phase boundary, they consume the latent heat and cool the mixture. The molar latent heat $l_{\text{mix}} = T(s_D - s_C)$ is positive, because the molar entropy of diluted phase s_D , which is inversely proportional to the Fermi energy, is greater than that of concentrated phase [44]. Practically this is done by pumping the ^3He vapours from the surface of the diluted phase. Because the ^3He atoms are lighter, they prevail in the pumped mixture. This means the ^3He concentration in the diluted phase decreases and new atoms can cross the phase boundary. Because the concentrated phase is lighter, the volume with liquid mixture is usually designed as a U-shaped joined vessels. In one arm, called 'mixing chamber', floats the concentrated phase and the bottom part and the other arm, where pumping takes place and which is called 'still', are filled with more dense diluted phase.

In such a way the mixture can be cooled until there is no ^3He left. Such an operation is called "single-shot regime". To enable a continual operation the ^3He is returned back to the mixing chamber. The amount of heat it brings in have to be minimized, so the ^3He goes through a series of heat exchangers, where it is cooled down by the pumped vapours and by pumped ^4He bath at about 1 K. The efficiency of the heat exchange is key parameter of the refrigerator.

3.2.2 Technical solutions of the COMPASS dilution refrigerator

The main requirements on dilution refrigerator of the SMC were: (1) to have a minimum amount of material in the beam and scattered particles paths, (2) to allow loading of the target material precooled below 100 K, (3) to provide large cooling power needed for DNP. The possibility to load precooled material is important to allow the use of solid NH_3 as a target material. A flow-type cryostat was chosen instead of a bath-type to enable faster operation. [3]

The schema of the refrigerator is shown on figure 3.3. The ^3He return flow is first cooled in a series of copper tubular heat exchangers by the pumped ^3He and by the ^4He evaporator (1.5 K). Then the return flow is cooled by thermal contact with diluted phase which flows from mixing chamber to the still. The contact is provided first by tubular heat exchanger made of flattened stainless steel tubes, which has a total surface area of 0.1 m^2 . It is followed by a series of sintered copper heat exchangers. Since the refrigerator has to provide high cooling powers at about 0.3 K, the effective surface area had to be increased by increasing the

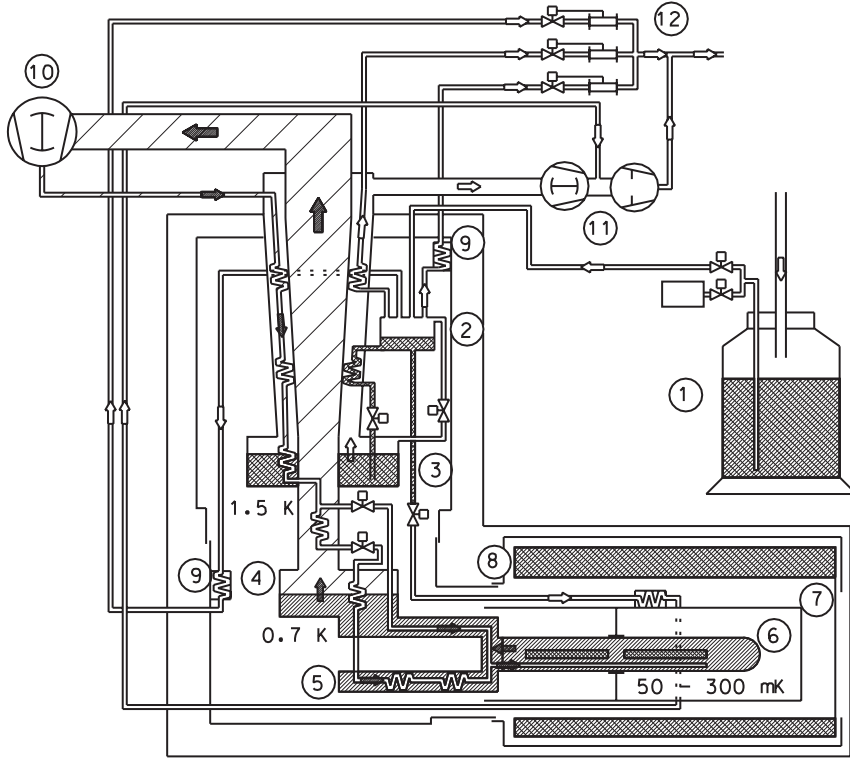


Figure 3.3: Simplified schema of the dilution refrigerator. (1) liquid He buffer dewar (2000 l), (2) ^4He gas/liquid separator, (3) ^4He evaporator, (4) still, (5) main heat exchanger, (6) mixing chamber, (7) microwave cavity, (8) magnet liquid He vessel, (9) thermal screen, (10) ^3He Root's pumps, (11) ^4He Root's and rotary pumps, (12) ^4He recovery line. Black (blank) arrows show ^3He (^4He) flows. [20]

interfacial area instead of sinter thickness. The 0.75 mm thick sinter with nominal grain size of about $18\ \mu\text{m}$ provides geometrical surface area of about $12\ \text{m}^2$ on both sides. The ^3He flows in two parallel streams, which are crossed on several points to prevent cold plug formation due to increasing viscosity around 0.5 K. [3]

The mixing chamber is made of glass-fiber reinforced epoxy with 0.6 mm wall thickness. It is 1.6 m long and has 7 cm in diameter. To ensure uniform cooling the ^3He is fed inside through CuNi tube, placed on the bottom of the chamber, with 40 holes drilled in it. The target holder can slide into a horizontal access tube (see figure 3.1) and is connected to the dilution unit by a cold indium seal. The cables for NMR coils and the cryogenic sensors enter the mixing chamber through the holder, which provides also thermal anchors to them. The 55 cm long target cells are made of polyester net with 60% of empty space to enable free access for the He mixture to the target material beads. The cells are held by Kevlar-epoxy composite structure for lightness, rigidity and small thermal contraction. [3, 20]

The mixing chamber is surrounded by the cylindrical copper microwave cavity. The cavity is divided axially into two or three compartments by a microwave stopper(s), made of copper foil. Inside the mixing chamber it has honeycomb structure to allow free He flow. The cavity is cooled to 3 K by pumped ^4He flow. [20]

The ^3He pumping is provided by 8 Root's blowers³ arranged in series. The pumping speed is 13 500 m³/h. The ^3He gas is purified in zeolite filters and in charcoal traps at room temperature and at 77 K. The ^3He flow rate is controlled by an electrical still heater, typical values are 15–100 mmol/s, measured by the flow meter and a quadrupole mass spectrometer⁴, which is used to measure the $^3\text{He}/^4\text{He}$ ratio [20]. Due to the rather high still temperature of about 0.7–0.9 K the pumped mixture contains about 25% of ^4He [3, 20].

The refrigerator working mixture consists of 9200 l of ^4He gas and 1400 l of ^3He gas (at standard temperature and pressure). During operation it consumes 15–20 l/h of liquid ^4He in separator, evaporator and the thermal-screen lines, depending on the ^3He flow rate [20]. The liquid ^4He is provided by a helium liquefier which has a maximum capacity of 100 l/h and also supplies the magnet system. A 2000 l dewar serves as a buffer.

3.2.3 Low temperature thermometry and refrigerator control

There are about 36 temperature sensors in the refrigerator. The temperatures of the thermal screens, and also of the mixing chamber during precooling, are measured using silicon diodes. The temperatures of the target cells, mixing chamber, still, evaporator and isolation vacuum are measured by ruthenium-oxide (RuO) and carbon⁵ resistors, read by four-wire AC resistance bridges⁶, which use very low excitation (low-frequency, square-wave) and low-noise, mostly analog, circuits, to minimize parasitic heating of the sensors. The Speer resistors at target cells are used as bolometers during microwave operation. [3, 29]

The thermometer resistance depends on the magnetic field. For the RuO sensors the resistance error was reported to be less than 2% over the temperature range used and at 2 T field [29].

Precise thermometry is needed during the thermal equilibrium (TE) calibration of the NMR system. The calibration is performed at temperatures about 1 K with ^4He circulating in the refrigerator. The temperature is measured by a ^3He pressure bulb inside the mixing chamber. The method is the most straightforward, since the international temperature scale ITS-90 is based on the ^3He saturated vapour pressure between 0.5 and 5 K. The pressure is measured by a high-precision capacitive gauge⁷. The error of temperature during TE calibration estimated by the SMC collaboration was about 0.4%. [3, 29]

The operation of the refrigerator is regulated by the resistive still heater and several motor-driven cold needle valves. The next section and the figure 3.4 shows the constraints on the operation conditions. Increase of the still temperature leads to faster evaporation and therefore to higher cooling power. On the other hand it increases the heat input into the mixing chamber (through the ^3He return).

The thermometers, pressure gauges, flowmeters and other sensors were connected to a PC with National Instruments LabVIEW control program[25] in the

³Pfeiffer Vacuum GmbH, they were originally used by the EMC experiment.

⁴Balzers QMS 311

⁵Speer and Allen–Bradley

⁶AVS-46 and AVS-47 from Picowatt (RV-Elektronikka Oy)

⁷MKS Baratron 270B

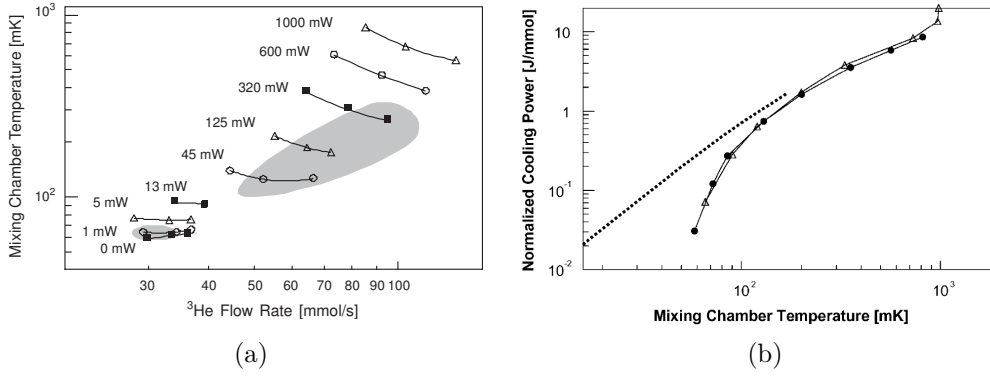


Figure 3.4: (a) Temperature of the mixing chamber as a function of ³He flow rate at various cooling powers. The shadowed regions define conditions during DNP (the wider one) and frozen-spin mode. (b) Dependence of the cooling power, normalized by \dot{n}_3 and assuming that 70% of ³He goes to the upstream cell, on the mixing chamber temperature at frozen-spin mode. The circles (triangles) show upstream (downstream) cell and the dashed line the idealized situation with $T_{in} = T_{mc}$ [20].

previous runs. In addition there was a Programmable Logic Controller (PLC)⁸ which ran in parallel with the LabVIEW control. There were three ET200 distributed I/O stations, that collected most important parameters and sent them to the PLC. The PLC controlled them and gave alarms. The motor-driven valves can be operated via the PLC. It had been added after experiencing several power failures in 2001 and 2002, which had made the control system blind. The PLC was powered by 48 V DC uninterruptable power source. There was also an ethernet interface that enabled to control its operation via the CERN network [29, 25]. Some less important or slow-varying parameters, e.g. the pump room temperature, were checked manually by the shift crew once in four hours.

The remote control planned for the DY program brings need to change this schema. The dilution refrigerator control is being transferred under the COMPASS DCS. This process, as well as the involvement of the author of this thesis in it, is described in more detail the chapter 4.

3.2.4 Refrigerator performance

The enthalpy balance for the mixing chamber is expressed by the equation [20]

$$\dot{n}_3[H_d(T_{mc}) - H_c(T_{mc})] = \dot{n}_3[H_c(T_{in}) - H_c(T_{mc})] + \dot{Q} + \dot{Q}_{leak} + \dot{Q}_{beam}, \quad (3.3)$$

where \dot{n}_3 is ³He molar flow, $H_{d,c}$ the molar enthalpy of the diluted and concentrated phase, T_{mc} is the mixing-chamber temperature and T_{in} is the temperature of the ³He return flow at the inlet into the chamber. The heat \dot{Q}_{leak} is brought to the chamber by the thermal conduction and radiation from outside and \dot{Q}_{beam} by the beam. The left-hand side of the equation represent the cooling capability of

⁸Siemens S7 300

the mixing process. The term in square brackets represent l_{mix} , the molar latent heat of the ^3He crossing the phase boundary.

The first term on the right-hand side represents the heat brought to the chamber by the ^3He return flow. The cooling power \dot{Q} can be used to cool down the chamber and the target material. It is what remains after subtraction of all mentioned heat inputs from the cooling capability:

$$\dot{Q} = \dot{n}_3[H_d(T_{\text{mc}}) - H_c(T_{\text{in}})] - \dot{Q}_{\text{leak}} - \dot{Q}_{\text{beam}}. \quad (3.4)$$

The heat leak \dot{Q}_{leak} was estimated conservatively to be about 4.5 mW, the dominant source being the conduction through the microwave stopper from the cavity and the thermal isolation providing Teflon tubes from the outside of the mixing chamber. The leak was measured in a single-shot regime, when the ^3He inlet is closed, to be 2.3 mW. The measurement was taken without a beam and the lowest temperature reached was 30 mK [20]. The \dot{Q}_{beam} was calculated to be about 2 mW [14] with the intense pion beam. The performance of the COMPASS refrigerator is shown on figures 3.4. The figure 3.4a shows the relations between cooling power, ^3He flow and temperature. The figure 3.4b shows normalized cooling power per mmol at frozen-spin mode. The measurement showed that 70% of ^3He goes to the upstream cell, which explains its slightly lower temperature, resulting in 2–3% higher polarization, observed at normal operation.

3.3 Dynamic nuclear polarization

If a particle with spin I is subjected to a magnetic field B , parallel to the z -axis, then the Zeeman interaction with Hamiltonian $\mathcal{H}_{IZ} = -\vec{\mu} \cdot \vec{B}$ forms a set of $2I + 1$ sublevels with energies $E_{Zm} = -\hbar\gamma_I Bm$. The $\vec{\mu} = \hbar\gamma_I \vec{I}$ is a magnetic dipole moment of the particle, γ_I is its gyromagnetic ratio and $m = \langle I_z \rangle$. The energy can be alternatively expressed as $E_{Zm} = \hbar\omega_I m$, where $\omega_I = -\gamma_I B$ is called Larmor frequency⁹

Consider the assembly of spins $I = 1/2$ in the magnetic field. We describe the orientation of the assembly by polarization $P_I = \langle I_z \rangle / I$ [8], which can be expressed as

$$P_I = n^+ - n^-, \quad (3.5)$$

where n^+ and n^- are fractions of the spins parallel ($m = +1/2$) and antiparallel ($m = -1/2$) to the magnetic field. If the system with Hamiltonian \mathcal{H} is in thermal equilibrium, the populations of its energy levels is given by the Boltzmann distribution. In other words, the density matrix of the system is

$$\rho = \exp(-\beta \mathcal{H}) \{ \text{Tr} [\exp(-\beta \mathcal{H})] \}^{-1}, \quad (3.6)$$

where $\beta = 1/(k_B T)$ is the inverse temperature (T is temperature and k_B the Boltzmann constant). The trace plays a role of a normalization factor. The expectation value of the polarization can be calculated using the density matrix as $\langle P_I \rangle = \text{Tr}(\rho P_I)$. If the spins are non-interacting, the polarization can be obtained directly using (3.5) and the Boltzmann distribution

$$\frac{n^-}{n^+} = e^{-\beta E_{Zm}}, \quad \text{leading to: } P_I = \tanh(\beta \hbar \gamma_I B m), \quad (3.7)$$

⁹It corresponds to the frequency of precession of a dipole in magnetic field in classical physics.

which is the special case (for $I = 1/2$) of the Brillouin law (3.30).

It turns out, that the thermal-equilibrium polarization of nuclei is very low even in high fields and at low temperatures. The ^1H nuclei in NH_3 reach polarization about 0.25% in 2.5 T magnetic field at 1 K [29]. In 8 T field and at 10 mK it can be about 70%, but these conditions are quite difficult to obtain and the thermal exchange between lattice and nuclei would become extremely slow for practically all insulators [2]. On the other hand, the 'brute force' method work well for metals, where the relaxation is shorter (and the DNP is impossible). It can be very effective for para- and ferro-magnets where the local fields can be amplified by electronic spins to a degree as high as 10^2 T [8].

For the electronic spins, which have the gyromagnetic ratio¹⁰ of about three orders higher, the polarization can be very close to -100% (-99.75% in a 2.5 T field at 0.5 K [8]).

The method of **Dynamic Nuclear Polarization (DNP)** allows to obtain high nuclear polarization. Phenomenologically it can be described as follows: Into the dielectric isolator, which contains the nuclei we want to polarize, we get¹¹ a small amount of paramagnetic impurities. The material is then put into static magnetic field, where the Larmor frequencies are ω_I and ω_S for nuclei and electrons¹² respectively, and irradiated by an oscillating magnetic field of a frequency $\omega = \omega_S + \delta$, where $\delta \simeq \omega_I \ll \omega_S$. For the typical static fields of the order of 1 T is ω_S in microwave region, while the ω_I in radiofrequency region.

The described procedure can lead to an enhanced nuclear polarization comparable to the electronic polarization. The method is called 'dynamic' since the polarized nuclei are in quasi-static state and the polarization decreases as they return back to equilibrium with the lattice. The relaxation times even in presence of the paramagnetic centers can be long enough (weeks or months) to allow experimental use, e.g. as polarized targets.

Originally the mechanism called **solid effect** was proposed for the above described phenomenon but it turned out that DNP works at much wider scale of conditions than is necessary for the solid effect and that other mechanisms contribute, or even prevail. In the solid effect approach the paramagnetic impurities are very dilute and interaction between them is neglected. In contrary, the DNP can be, for many materials, described rather as a cooling of an electronic spin-spin interaction 'reservoir', thermally connected with nuclear spins. The key concept of this approach is **spin temperature**. In the next two sections an outline of the mechanism of the DNP is given. The comprehensive explanation, as well as many experimental results, can be found in reviews [2, 8]. The latter principle is also the case of the COMPASS target [3]. The description of the COMPASS DNP system is given in the section 3.3.3.

Calling only the above described method DNP may seem not quite correct, because also other 'dynamic' methods of polarization exist, but the practical importance of the above described method exceeds that of the other methods so much, that the restrictive definition is used [2].

¹⁰Note, that the gyromagnetic ratio for electrons is negative. That means the polarization defined in (3.5) is negative in thermal equilibrium.

¹¹The paramagnetic centers can be introduced by chemical doping or irradiation, which creates free radicals [3].

¹²Or, more precisely, ω_S is the center of the Electron Spin Resonance (ESR) line.

3.3.1 System of electronic and nuclear spins and the solid effect

Consider the assembly of nuclear spins I and electronic spins S in magnetic field B . The Hamiltonian is

$$\mathcal{H} = \mathcal{H}_{SZ} + \mathcal{H}_{IZ} + \mathcal{H}_{SS} + \mathcal{H}_{II} + \mathcal{H}_{IS} + \mathcal{H}_{RF}, \quad (3.8)$$

the first two terms being Zeeman Hamiltonians of electronic and nuclear spins, the last term influence of the possible oscillating magnetic field and the other three interaction Hamiltonians between spins. We consider both spins to be $1/2$, since that is the case for electrons and ^1H . The term describing the interaction with lattice was omitted. The standard approach to it is phenomenological. The return to the thermal equilibrium with lattice is described by an exponential function.

First consider only a pair of a nuclear spin I and an electronic spin S . The interaction between them is generally in the form $\vec{S} \cdot a \cdot \vec{I}$, where a is a tensor. We shall consider only the simple dipolar interaction

$$\mathcal{H}_{SI} = \frac{\hbar^2 \gamma_S \gamma_I}{r^3} \left[\vec{S} \cdot \vec{I} - \frac{3(\vec{S} \cdot \vec{r})(\vec{I} \cdot \vec{r})}{r^2} \right], \quad (3.9)$$

where \vec{r} is the vector joining the spins with magnitude r and azimuthal and polar angles θ and ϕ . The more complicated cases would be if there is an anisotropy in electronic gyromagnetic factor or if the wavefunction of the electron is non-negligible on the nuclear site, making the scalar hyperfine interaction possible.

The interaction can be viewed as an interaction of the nucleus with fluctuating field produced by the electron. One source of the fluctuation is \vec{r} , which would, in a solid, represent a thermal motion of the lattice. This motion is nearly frozen-out at low temperatures. Another possible source are electron-spin flips, which can be caused by spin-lattice relaxation of the spins S . The correlation time is then given by the electronic spin-lattice relaxation time T_{1S} or spin-spin relaxation time T_{2S} , whichever is shorter¹³. If the power spectrum of the fluctuation is non-zero at the nuclear Larmor frequency, it can initiate nuclear spin flips. This approach is useful when dealing with electron-enhanced nuclear relaxations.

The other approach is as follows: Consider energy levels of the nucleus-electron pair. For non-interacting pair the states are pure: $|++\rangle$, $|+-\rangle$, $| - + \rangle$ and $| -- \rangle$ ¹⁴. The transitions between levels with two spin flips are forbidden. The dipolar interaction (3.9) admixes the states into perturbed ones: $|a\rangle$, $|b\rangle$, $|c\rangle$ and $|d\rangle$, shown on figure 3.5. The mixing coefficients in the first-order perturbation theory are [2]

$$q = \frac{3}{4} \frac{\gamma_I \gamma_S \hbar^2}{r^3 \omega_I} \sin \theta \cos \theta e^{i\phi}, \quad p = \sqrt{1 - qq^*} \approx 1. \quad (3.10)$$

In the 2.5 T field and for $r = 2 \text{ \AA}$ is q typically in order of 10^{-2} [8]. We can see that the interaction enabled mutual flips of spins I and S , if they are put

¹³More precisely, the inverse correlation times are additive: $1/\tau = 1/\tau_r + 1/T_{1S} + 1/T_{2S}$.

¹⁴Note, that $\gamma_S < 0$ and $\gamma_I > 0$ implies that the lowest level is $| - + \rangle$ (S antiparallel and I parallel to the magnetic field).

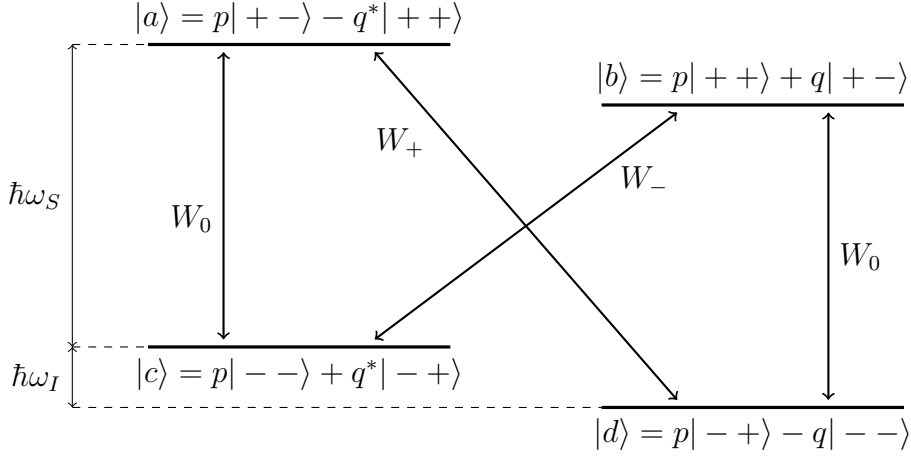


Figure 3.5: Eigenlevels of a nucleus-electron pair of spins 1/2 in high magnetic field, coupled by a dipolar interaction (3.9) in the first-order perturbation theory [2, 8].

in an oscillating field which can supply the energies $\hbar(\omega_S \pm \omega_I)$ needed for the transitions. For the case of relaxation the energy is supplied by the lattice. The transition probabilities W_{\pm} can be calculated by evaluating corresponding matrix elements of the \mathcal{H}_{RF} . The ratio W_{\pm}/W_0 is found to be proportional to $4|q|^2$ [8].

The solid effect can be outlined¹⁵ as follows: The sample is in magnetic field and is irradiated by microwaves with frequency corresponding to one of the forbidden transitions. The mutual flip-flops to the upper states are induced. Once the electronic spin is up, it starts relaxing and returns to the equilibrium state in a time of about T_{1S} . Then it is ready to flip other nuclear spin. On the other hand the nuclear-spin relaxation time T_{1I} is much longer, so polarization enhancement is possible. There is an obstacle, because the probability is proportional to $|q|^2$, and thus to r^{-6} , which would make the polarization build-up time uncomfortably long for our case of very diluted paramagnetic impurities. This is not a problem thanks to the 'spin diffusion', caused by the energy-conserving flip-flop processes among the nuclear spins¹⁶. Their characteristic time T_{2I} is usually very short in solids.

The above-described mechanism is well understandable if the ESR linewidth is smaller than the nuclear Larmor frequency $\Delta\omega_S \ll \omega_I$. In that case, called 'resolved solid effect', we can tune the frequency such that nuclear flips in only one direction can occur. On the other hand, if the ESR line is broader, which is often the case, complications arise. It is still possible to use the above outlined theory, but only if the ESR line can be viewed as a set of independent spin packets with slightly different Larmor frequencies, which is seldom justified. The other problem is that this 'differential solid effect' model does not allow to calculate a reasonable absolute value of the polarization enhancement [2].

Note, that the ESR linewidth is usually given by an inhomogeneous broadening, caused by the fact that spins occupy sites with different chemical neigh-

¹⁵More details (also quantitative, such as rate equations) can be found in [2].

¹⁶Caused by the secular part of \mathcal{H}_{II} , to which a dipolar coupling and possibly a J-coupling contribute.

bourhood. The small inhomogeneity of the electronic g-factor in the order of $\gamma_I/\gamma_S \ll 1$ can disturb the condition $\Delta\omega_S \ll \omega_I$ at all fields. In most substances where DNP is observed the condition of the resolved solid effect is violated [2].

3.3.2 Spin temperature theory

The spin temperature theory is based on presumption that the system of spins S can be considered isolated. The system then evolves towards equilibrium, described by the density matrix (3.6), where \mathcal{H} is replaced by spin-spin Hamiltonian \mathcal{H}_{SS} and inverse temperature β by $\beta_S = 1/(k_B T_S)$, T_S being the spin temperature. The presumption is justified only if spin-spin relaxation time T_{2S} , being the time needed to reach the internal equilibrium among the spins, is much shorter than spin-lattice relaxation time T_{1S} . For the time T_{1S} the spin temperature exists and can be different from lattice temperature T . From this point of view the spin-lattice relaxation is seen as an equalization of the temperatures T_S and T of spin and lattice reservoirs. [2]

The spin temperature can be both positive and negative, because the energetic spectrum of the spin system has an upper limit. The negative temperature means that entropy of the system decreases when heat is transferred to it. The higher levels are more populated than the lower ones at negative temperature.

The principle of DNP in most substances is cooling¹⁷ of the spin-spin reservoir of electronic spins, which is thermally connected to nuclear Zeeman reservoir. The connection has a form of the interaction, described under the equation (3.9). This time the fluctuating field is due to electronic spin-spin interaction. That is because the probability that an electronic spin flips due to the spin-lattice relaxation is much smaller than due to spin-spin relaxation when $T_{2S} \gg T_{1S}$.

The evidence of the strong connection is that the nuclear spin-lattice relaxation rate is for many materials simply proportional to the concentration of paramagnetic impurities, if the concentration is low. In fact, in high fields and at low temperatures it is usually the electronic spin-spin reservoir, what intermediates the thermal connection of nuclear spin system with the outside world. If we are able to cool the spin-spin reservoir and the thermal connection is good enough, we can cool also the nuclear Zeeman reservoir, which means to polarize the nuclear spins.

Consider the system of electronic spins in high magnetic field. The Hamiltonian

$$\mathcal{H} = \mathcal{H}_{SZ} + \mathcal{H}_{SS} = \sum_i S_{zi} \omega_S + \mathcal{H}_{SS} \quad (3.11)$$

is a sum of Zeeman Hamiltonian and spin-spin Hamiltonian, for which we assume the form of a dipolar interaction. Only the secular part

$$\begin{aligned} \mathcal{H}'_{SS} &= \frac{1}{2} \sum_{i,j} A_{ij} [2S_{zi} S_{zj} - 1/2(S_{+i} S_{-j} + S_{-i} S_{+j})], \\ A_{ij} &= \frac{1}{2} \gamma_S^2 \hbar (1 - 3 \cos^2 \theta_{ij}) r_{ij}^{-3}, \end{aligned} \quad (3.12)$$

¹⁷Here the term 'cooling' is used for any process, when $|T|$ decreases. If temperature of the nuclear spins $T_I \rightarrow 0^+$, than $P_I \rightarrow 100\%$; if $T_I \rightarrow 0^-$, than $P_I \rightarrow -100\%$.

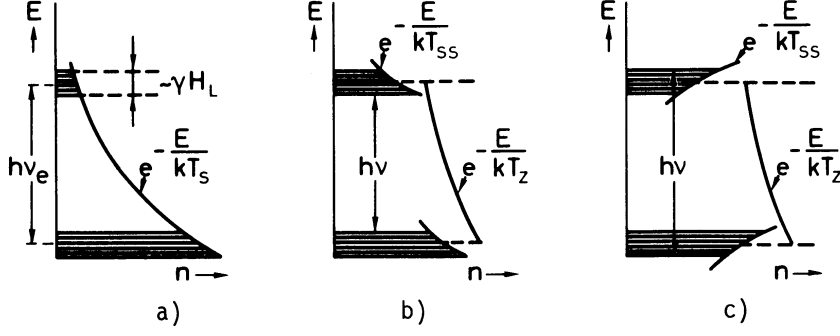


Figure 3.6: The distribution of populations over the energy levels for spins in high field: (a) In the thermal equilibrium with the lattice, (b,c) after irradiation at frequency ν , slight different from ν_e , can the temperatures of the Zeeman and spin-spin reservoirs differ. Here ν_e denotes the Larmor frequency of electrons and T_S , T_{SS} temperatures of Zeeman and spin-spin reservoir respectively [8].

of the dipolar Hamiltonian has to be taken into account, according to the first-order perturbation theory. In the high field the broadening of the levels is much smaller than the distance between them (see the figure 3.6). The internal processes have to conserve energy and cannot take place between levels with different value of $S_z = \sum_i S_{zi}$. If one spin is flipped up, there have to be other spin that simultaneously flips down. This means that, apart from the total energy $\langle \mathcal{H} \rangle$, also the Zeeman energy $\langle \mathcal{H}_{SZ} \rangle$ is conserved, yielding that the spin-spin energy $\langle \mathcal{H}_{SS} \rangle$ is conserved too. The most probable populations of states then are [2]

$$\rho = \exp(-\alpha \omega_S S_z - \beta_S \mathcal{H}'_{SS}) \{ \text{Tr}[\exp(-\alpha \omega_S S_z - \beta_S \mathcal{H}'_{SS})] \}^{-1}, \quad (3.13)$$

α and β_S being the inverse temperatures of the Zeeman and spin-spin reservoirs respectively. Now we focus on two particular levels a, b , separated by energy $\hbar\omega = \hbar(\omega_S - \delta)$, $|\delta| \ll \omega_S$. Their Zeeman levels differ by $\hbar\omega_S$, and spin-spin sublevels by $\hbar\delta$. The ratio of populations on the levels is given by (3.13) as

$$p_a/p_b = \exp(\alpha \omega_S - \beta_S \delta). \quad (3.14)$$

If the material is irradiated at frequency ω , the populations of the levels a, b can be equalized, if we neglect the spin-lattice relaxation. That implies

$$\alpha \omega_S = \beta_S \delta. \quad (3.15)$$

Since $|\delta| \ll \omega_S$, an absolute value of the spin temperature $|T_S|$ can be much lower than $|T|$. We can see that negative temperature can be obtained when $\delta < 0$. This is illustrated on figures 3.6b, c.

It is more convenient to work in reference frame rotating at frequency ω of the oscillating field, perpendicular to the static field B . The effective Hamiltonian then is

$$\mathcal{H}_{\text{eff}} = S_z \delta + \mathcal{H}'_{SS} + \omega_1 S_x, \quad (3.16)$$

where $\omega_1 = -\gamma_S B_1$ is the Larmor frequency in the oscillating field. The Zeeman temperature in oscillating field is $\alpha' = \alpha \omega_S / \delta$, so the equation (3.15) has a simple

meaning $\alpha' = \beta_S$ in the rotating frame. The heat capacity $\omega_1 S_x$ can usually be neglected, since $B_1 \ll B$ in most cases.

The rate equations for α' , β_S under irradiation can be derived in high temperature limit¹⁸, where we can approximate the exponential in ρ by its expansion to the first order. Then the Provotorov equations can be derived. After addition of relaxation terms they are [2]

$$\begin{aligned}\frac{d\alpha'}{dt} &= -W(\alpha' - \beta_S) - \frac{\alpha' - \alpha_L}{T_{1Z}} \\ \frac{d\beta_S}{dt} &= W \frac{\delta^2}{D^2}(\alpha' - \beta_S) - \frac{\beta_S - \beta_L}{T_{1D}},\end{aligned}\quad (3.17)$$

where $W = \pi\omega_1^2 g(\delta)$, $g(\delta)$ is the shape of the absorption signal, normalized to unit area and

$$D = \gamma_S B'_{\text{loc}} = \sqrt{\text{Tr}(\mathcal{H}'_{SS})^2 [\text{Tr}(S_z^2)]^{-1}} \quad (3.18)$$

is the local Larmor frequency in the rotating frame. The relaxation terms describe the equalization of temperatures between the reservoirs and the lattice. Without the oscillating field:

$$\begin{aligned}\frac{d}{dt}\langle S_z \rangle_{\text{relax}} &= -\frac{\langle S_z \rangle - \langle S_z \rangle_L}{T_{1Z}} \\ \frac{d}{dt}\langle \mathcal{H}'_{SS} \rangle_{\text{relax}} &= -\frac{\langle \mathcal{H}'_{SS} \rangle - \langle \mathcal{H}'_{SS} \rangle_L}{T_{1Z}},\end{aligned}\quad (3.19)$$

where the subscript L means values in the equilibrium with the lattice. β_L is the lattice inverse temperature and $\alpha'_L = \beta_L \omega_S / \delta$. The values of β and α' in the steady state can be easily calculated from the equations (3.19). In limit of strong oscillating field $WT_{1D}, WT_{1Z} \gg 1$ one gets

$$\beta_s^{\text{eq}} = \beta_L \frac{\omega_S \delta}{\delta^2 + (T_{1Z}/T_{1D})D^2}. \quad (3.20)$$

The absolute value of the inverse spin-spin temperature in oscillating field is largest when $\delta^2 = (T_{1Z}/T_{1D})D^2$. The concept of spin temperature was proven valid for dilute electronic systems with concentrations down to 10^{-4} – 10^{-5} . It is also valid if other interactions than dipolar contribute to the spin-spin Hamiltonian [2].

In the case of DNP the spin-spin reservoir is connected to the nuclear Zeeman reservoir and they share the same temperature. There have to be done some modifications to the equation (3.20). For example the relaxation of the combined system towards the lattice temperature is slowed down, because the joint reservoir is bigger. Finally we obtain [2]

$$\beta_s^{\text{eq}} = \beta_L \frac{\omega_S \delta}{\delta^2 + (T_{1Z}/T_{1D})D^2(1-f)}, \quad (3.21)$$

where f is the leakage factor. It takes into account the relaxation of nuclear spins through dipolar coupling with electronic spins.

The results of the spin temperature theory can be well illustrated when two nuclear spin species are present. The temperatures of the two nuclear spin systems

¹⁸The limit is valid if the energy per spin is much smaller than the thermal energy $k_B T_S$.

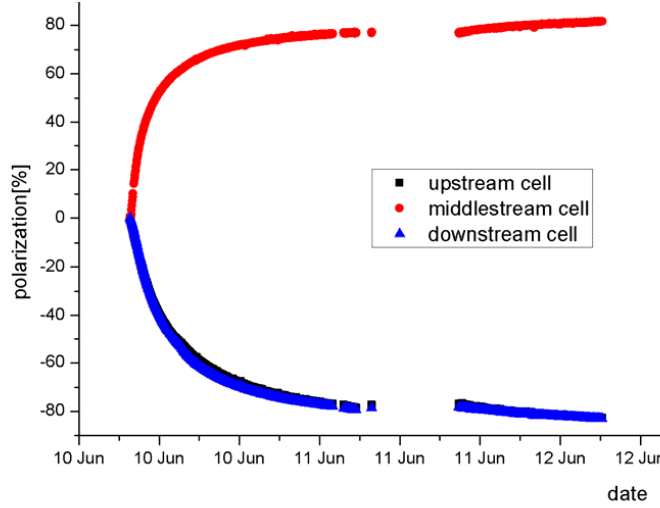


Figure 3.7: Polarization buildup, 10–12 June 2010. The target material was NH_3 in three cells, polarized $(- + -)$ in this case [39].

are the same through the duration of DNP. The highest polarizations of both spin systems are reached at the same oscillating field frequency. That is in contrast with the resolved solid effect. In that case the ideal frequencies differ.

The validity of the spin temperature theory in ammonia target material was tested by SMC collaboration. The DNP was performed with stops along the way to measure polarizations of both ^1H ($\omega_I = 106.5$ MHz) and ^{14}N ($\omega_I = 6.47$ MHz). The spin temperature was found to be equal in large range of polarizations, despite the different Larmor frequencies. The small systematic deviation was found for large polarizations, possibly due to solid effect contribution [3].

3.3.3 Dynamic nuclear polarization at COMPASS

The polarization by DNP at COMPASS is performed in 2.5 T magnetic field. An example of the polarization buildup is shown on figure 3.7. The corresponding electronic Larmor frequency is about 70 GHz. There are two independent microwave sources to enable simultaneous opposite-polarization buildup in the two target cells. They operate at frequencies on the edges of the ESR line with a spacing of about 0.4 GHz. The frequency and the power are fine-tuned during the DNP. [3]

The sources of microwaves are two Extended Interaction Oscillator (EIO) tubes. They can be tuned coarsely in range of about 2 GHz around 70 GHz by changing the cavity size. The fine tuning is done by changing the voltage of the HV power supply. A triangular waveform was applied to the cathode voltage to improve both the speed and the maximal degree of polarization for the ^6LiD target [3]. The effect of modulation was found small for NH_3 [29].

The two power control attenuators were used to regulate microwave power. They were constructed by the SMC target group, because the commercial attenuators would not withstand the power levels of about 15 W. They consist of two hybrid tees, waveguides and matched loads arranged in a trombone-like structure. The incoming microwaves are divided into two arms and then combined again.

The length of one arm is adjustable by a motor-driven screw. Thus the phase difference of the combined waves can be adjusted. The attenuation is in range 2.5–20 dB. Fine control of the power is done by tuning the anode voltages [3].

The frequency is monitored by two frequency counters¹⁹. The power is measured on two places. After the attenuators there is a single thermocouple power meter, fed through a microwave switch. Inside the cavity there are two carbon resistors²⁰, used as bolometers. The thermocouple power meter is used for their calibration. The optimum power in the cavity was found to be 0.8 W at the start of the process, decreasing to less than 0.1 W at the maximum polarization [3].

The microwave sources, power control attenuators, frequency counters and a power meter are located in the control room. The microwaves are delivered to the cavity via 15 m X-band waveguides. The thermal isolation in the waveguides inside the cryostat is made of internally silvered CuNi tubes of 4 mm diameter. The connection to the cavity consists of K-band waveguides soldered along the cavity with several equidistant slits. A new copper cavity of 0.4 m diameter and 1.376 m length will be used in Drell–Yan program [29]. The cavity is divided axially into two compartments by a microwave stopper. This allows operation on different frequencies to obtain opposite polarizations. The microwave isolation was measured to be about 20–30 dB [3].

3.4 NMR polarization measurement

The experiment requires precise measurement of the nuclear polarization throughout the whole target volume. The continuous-wave NMR system with 10 coils serves this purpose. The outline of the measurement principle is given in section 3.4.1, the apparatus used on COMPASS is described in section 3.4.2.

3.4.1 Principle of the NMR polarization measurement

Consider an ensemble of nuclear spins I in static magnetic field B . A degree of ordering of the spins is described by macroscopic polarization, which is the ratio of spins parallel to the magnetic field (see equation (3.5)). Another important macroscopic quantity is magnetization

$$M = \mu NP, \quad M = \chi_0 B, \quad (3.22)$$

where N is number density of spins, μ magnetic moment of the nucleus and χ_0 is called static magnetic susceptibility. The magnetization can be in principle measured directly, but for the nuclear spins it is too small. If the magnetic field is not static, the relation between field and magnetization is described by dynamic susceptibility $\chi(\omega)$. Clearly $\chi_0 \equiv \chi(0)$. The dynamic susceptibility has both real and imaginary part

$$\chi(\omega) = \chi'(\omega) - i\chi''(\omega) \quad (3.23)$$

¹⁹Phase Matrix EIP 578

²⁰Speer 220 Ω

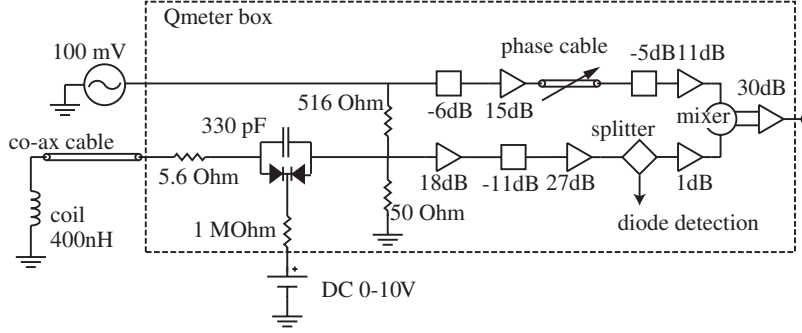


Figure 3.8: The Q-meter circuit. The RF voltage drives the series-tuned resonance circuit with a constant current. The real part of voltage is selected by phase sensitive detection [33].

to describe both dispersion (χ') and absorption (χ''). The Kramers–Kronig relations, which bind the real and the imaginary part, imply

$$\chi_0 = \chi'(0) = \frac{2}{\pi} \mathcal{P} \int_0^\infty \frac{\chi''(\omega)}{\omega} d\omega, \quad (3.24)$$

where \mathcal{P} denotes principal value of the integral. Using equation (3.22), nuclear Larmor frequency $\omega_I = \gamma_I B$ and remembering $\mu = \hbar \gamma_I I$ we obtain

$$P = \frac{\chi_0 B}{\mu N} = \frac{2}{\pi \hbar \gamma_I^2 I N} \mathcal{P} \int_0^\infty \chi''(\omega) \frac{\omega_I}{\omega} d\omega. \quad (3.25)$$

The integration needs actually to be done only over frequencies where the absorption part of susceptibility $\chi''(\omega)$ is nonzero. For ^1H nuclei in 2.5 T field is the NMR line narrow²¹, yielding $\omega_I/\omega \approx 1$ inside the integrated area. As will be explained soon, only the proportionality of the polarization to the integral $\int \chi''(\omega) d\omega$ is important for the measurement.

The absorption part of the nuclear susceptibility is measured as follows: A coil is placed inside or on the surface of the target cell. The dynamic nuclear susceptibility $\chi(\omega)$ changes the coil inductance

$$L(\omega) = L_0(1 + \eta\chi(\omega)), \quad (3.26)$$

where η is coil filling factor and L_0 is inductance of the empty coil. The coil impedance

$$Z_c = R_c + i\omega L(\omega) \quad (3.27)$$

is measured by a series-tuned **Q-meter**. The circuit is shown on figure 3.8. The Q-meter provides a complex voltage $V(\omega, \chi)$. The real part of voltage is selected by a phase-sensitive detector²². The Q-meter is tuned so that the minimum of $V(\omega, 0)$ occurs at $\omega = \omega_I$. The RF synthesizer provides voltage, swept around the ω_I .

²¹For the ^1H and ^2H targets used by the SMC in 2.5 T field was $\chi''(\omega) \neq 0$ in about 300 kHz range around ω_I , the Larmor frequency was 106.5 MHz for ^1H and 16.35 MHz for ^2H [3].

²²See the right-hand side of figure 3.8.

The signal is measured in two steps. Firstly, a "baseline" is measured by shifting the magnetic field by a few percent, while keeping the RF scan in the nominal frequency range. This way the nuclei are brought off-resonance and $V(\omega, \chi'' = 0)$, the frequency response of the Q-meter alone, is recorded. Then the NMR signal is measured by scanning at normal B [3]. The two signals are subtracted with the result

$$\text{Re}[V(\omega, \chi)] - \text{Re}[V(\omega, \chi'' = 0)] \equiv S(\omega). \quad (3.28)$$

It can be shown (see [3]), that $S(\omega) \propto \chi''(\omega)$, yielding

$$P = C \int S(\omega) d\omega. \quad (3.29)$$

The constant of proportionality C depends on both properties of the material and the Q-meter circuit. It is determined by a **thermal equilibrium calibration** of the system.

At a thermal equilibrium²³ with the lattice the polarization is given by the Brillouin function [33]

$$P_{\text{TE}}(x) = \frac{2I+1}{2I} \coth\left(\frac{2I+1}{2I}x\right) - \frac{1}{2I} \coth \frac{x}{2I}, \quad x = \frac{\hbar\gamma_I I}{k_B T}, \quad (3.30)$$

which is simply $\tanh(x)$ for spin $I = 1/2$. As long as the polarization is known, the constant C can be calculated from the equation (3.29).

3.4.2 COMPASS NMR system

There are 10 Q-meter circuits to ensure good sampling of the target volume. Diagram of the system is shown on figure 3.9 (only one coil branch is shown for better readability). All branches are fed from a single RF synthesizer and share a common data taking system.

There are quite contradicting demands on the NMR coils. The filling factor η and the empty coil inductance L_0 should be large in order to have strong signal. Moreover, the sensitivity is most important on the target axis, where the beam is strongest and thus most scattering events happen there. Coils embedded in the target material would be ideal from this point of view. On the other hand, coils placed inside the target volume lower the dilution factor²⁴ f . See the section 4.2 for more discussion on coil design.

Another problem with coils with large inductance is a danger of superradiance during the field rotations [3]. The superradiance is a spontaneous emission, where the emitting particles are coupled by their common radiation field and thus decay cooperatively²⁵. The effect occurs for the negatively polarized cell, when the Larmor frequency of the nuclei, which varies with the field during the field rotation procedure, crosses the resonant frequency of the coils. On the SMC target a polarization change from -88% to +28% locally near the NMR coil was recorded

²³This is actually true always when the Zeeman energy is large in comparison to the energy of spin-spin interactions, the lattice temperature T just has to be replaced by the spin temperature.

²⁴defined in equation (3.2) in section 3.1.1.

²⁵The practical experience with the effect on a polarized target can be found in [41], where reversal from -90% to +60% was observed when the circuit was adjusted the right way. The theoretical description can be found in the original paper [18].

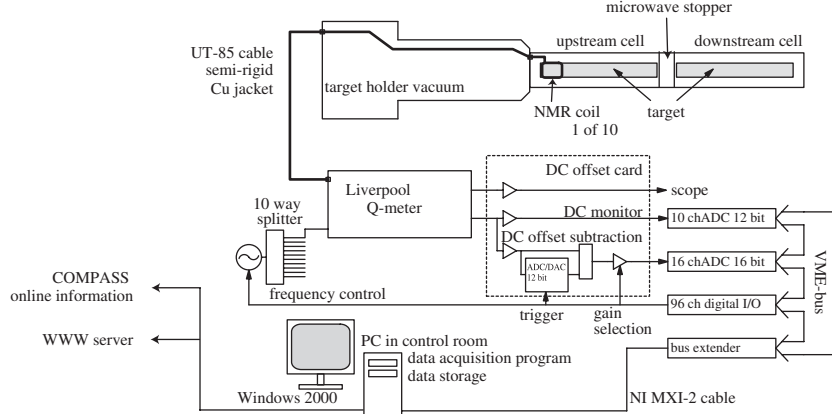


Figure 3.9: The NMR system. The coils are connected to the Q-meters by coaxial cables. The Yale-cards subtract offset and amplify the signal. The signals are read by 16-bit ADC modules connected to PC via VME bus. Another VME module controls the synthesizer [33].

in an extreme case. This effect can be suppressed, if the magnetic field is made inhomogeneous during the field rotation. The second precaution is use of small-inductance coils [3].

The coils should not touch the material, because the RF field is strong near the coil surface, causing unwanted saturation effects. Coating can help with that and was previously used several times. The isolation layer must not contain any protons, otherwise they would cause strong background signal.

The coils are connected to the Q-meters by a half-integer wavelength coaxial cable. A small modification was made to the conventional Liverpool Q-meters. Varactor diodes were added for more convenient tuning. They are driven by a DC voltage and can vary capacitance of the resonant circuit in range 20–550 pF. The Q-meters amplify the signal and select the real part of voltage $V(\omega, \chi)$. They are followed by Yale cards. They subtract DC offset and further amplify the signal. The offset is measured at the lowest frequency of the "baseline" scan. The same DC voltage of the opposite polarity is then applied to the signal. This operation provides better dynamic range of the system. The gain of the cards can be switched to 1, 207 or 334. The gain 207 is used for measurement of weak TE signals, while no amplification is used for enhanced polarization measurement during frozen spin mode. [33]

VME-bus modules are used for controlling the system and acquiring the data. The crate with VME modules is placed on the target platform to minimize the length of the coaxial cables. The data acquisition program runs on PC in control room. The LabVIEW program was used during previous runs. The new data acquisition system will probably be made for the remote control during DY run.

The TE calibration is done at several temperatures around 1 K. That is for two reasons. The first is that it is a good compromise between two contradictory demands, which are a strong signal and a short spin-lattice relaxation. The signal strength drops with rising temperature, while the relaxation rate is the opposite. Around 1 K the spin-lattice relaxation time is about 20 minutes, the polarization is about 0.25 % in the 2.5 T field [3]. The second is that the temperature can

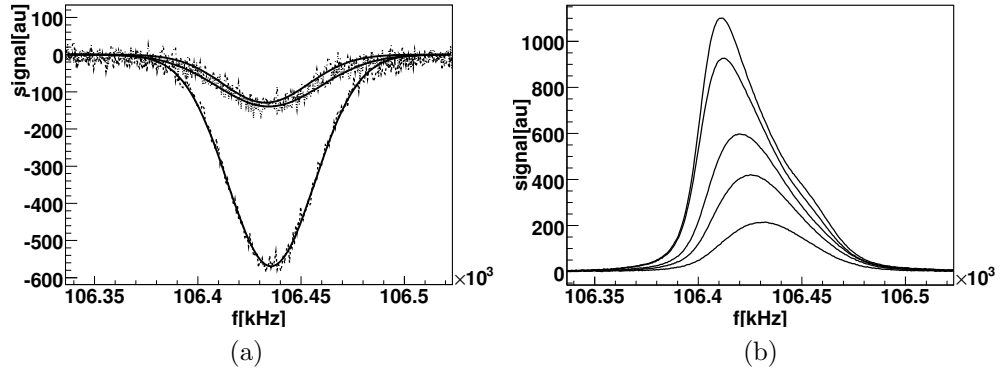


Figure 3.10: NMR signals of ^1H : (a) During TE calibration at 1.3 K. The smaller signal is from empty target holder calibration. All signals fit well a Gaussian. (b) Signal lineshape at approximate polarizations -20%, -40%, -60%, -80% and -90% [31].

be kept stable and uniform by pumping vapours of pure superfluid ^4He by the dilution refrigerator system and precisely measured by the ^3He vapour pressure thermometer (see the section 3.2).

In ammonia, the protons are arranged in triangular configurations, resulting in an asymmetric lineshape at high polarizations [3] (see the figure 3.10b). Unlike in the frozen spin mode, when the signal is quite strong, during TE calibration the signal has to be amplified and is noisy (see figure 3.10a). The noise causes dependency of the integrated area on the choice of the bounds of integration, even outside the region where the susceptibility can be nonzero. One of used approaches is to select many different bounds and use the average result²⁶. Another problem is that the background signal of protons in the construction materials cannot be neglected. This background signal is measured at the beginning and at the end of each run with the empty target holder. [39]

²⁶See [33], where the method is applied to ^2H nuclei.

4. Remote control and simulations of the target NMR

4.1 Program package ptread for remote control and monitoring

The polarized target is a complex device with many parameters that have to be monitored and sometimes adjusted. Cryogenic systems of the dilution refrigerator and the superconducting magnet can cause great losses in the hypothetical case of catastrophic failure. The microwave and NMR systems are less delicate, but their precise operation is critical for the accuracy of the experiment.

In the previous runs with polarized target there were several computers in the control room, which allowed monitoring and control of polarized target systems. There was a Linux computer with Perl and EPICS software to control the magnet power supply and another PC with CERN software based on Java to control magnet cryogenics. The dilution refrigerator was controlled from Windows PC with LabVIEW program, the most important parameters were controlled also by the PLC, powered by an uninterruptable source [25]. Another PC with LabVIEW controlled the NMR system. The microwaves for DNP were controlled manually.

The need of moving of the control room to the office building due to higher radiation level expected during DY run (see the section 2.1.7) means that the described schema has to be altered. Especially the LabVIEW PCs would be difficult to operate remotely. Apart from that it was decided that on this occasion the slow control of the target will be transferred under the standard COMPASS DCS¹.

The strategy, that was chosen for monitoring of the dilution refrigerator and possibly some other instruments, is to control them from Linux PC using a program package **ptread**, which is being developed. The target magnet is going to be maintained by CERN Cryogenics group after the repair, which is in progress in the CERN workshop. They are also going to take care of delivering of the magnet monitoring parameters to the COMPASS DCS. The PLC, which has proved to be useful, is keeping its backup role.

4.1.1 Introduction to ptread

The purpose of the ptread package is to provide remote access to temperatures, flows, pressures and other parameters of the polarized target. It communicates with measuring instruments, and it makes the readings accessible for the COMPASS shift crew, the weekly coordinator and target experts from the PCs in the new remote control room and from the internet. The best way to that goal is to provide the data to the DCS, since it is a COMPASS standard, easy to use for any member of the collaboration. The target experts may also appreciate alternative ways, that are also being tested.

¹The polarized target is actually the last major part of the experiment which is not fully using the DCS slow control.

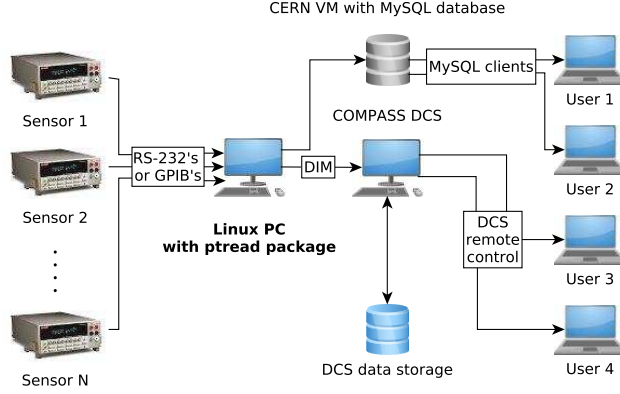


Figure 4.1: Diagram of pthread communication. The computer with SLC 5 and pthread package reads sensors. Data can be stored locally in SQLite database, send to MySQL database and published by DIM server for COMPASS DCS (PVSS).

The pthread package is being developed by Jaakko Koivuniemi, with the help of the author of this thesis. It is a set of command-line Linux applications, written under the GNU General Public License. The main language used is Perl, but parts use also Python and C++. The CERN SVN² server is used to backup and share the work. Careful attention is paid to program documentation. Every program in the package has to have a standard Unix manual page and an on-line "How-to" [32] is being composed for the future users. The program package is modular and can be easily modified if for example some instrument is exchanged. Thanks to the documentation, modularity, open-source components and the wide spectra of outputs, including standard databases, its use for other systems than the COMPASS polarized target is possible. It can be found suitable for control of slow-varying parameters of any system.

The schema of pthread PC communication with sensors and users is shown on figure 4.1. The communication with instruments goes mainly via General Purpose Interface Bus (GPIB), which is also called IEEE-488 bus. The use of GPIB requires a dedicated PCI board or an external USB GPIB device. Because the package is designed for a Linux machine³, the board has to be supported by the LinuxGPIB package [28]. The advantages of the GPIB are easy operation, once the LinuxGPIB package is configured correctly, and the possibility to connect up to 15 instruments. If the device supports a serial connection (RS-232 standard) the corresponding pthread driver supports it too. The serial interface has an advantage that it can be connected to any PC without any special hardware, just the cable and eventually the RS-232–USB converter.

The measured data can be published by a DIM server⁴ for the DCS, stored in a local SQLite database⁵ and send to MySQL database. The last possibility makes the system more versatile, since MySQL is a widespread standard. The data can be easily read using PHP, Perl or Python clients, suited to fit needs of

²Apache Subversion, the open-source version control system [13].

³Currently the Scientific Linux CERN (SLC) 5

⁴DIM [24] is a standard way of communication for the DCS (see the section 2.1.6, or [16]).

⁵Lightweight database for local use (no server), uses the Structred Query Language (SQL).

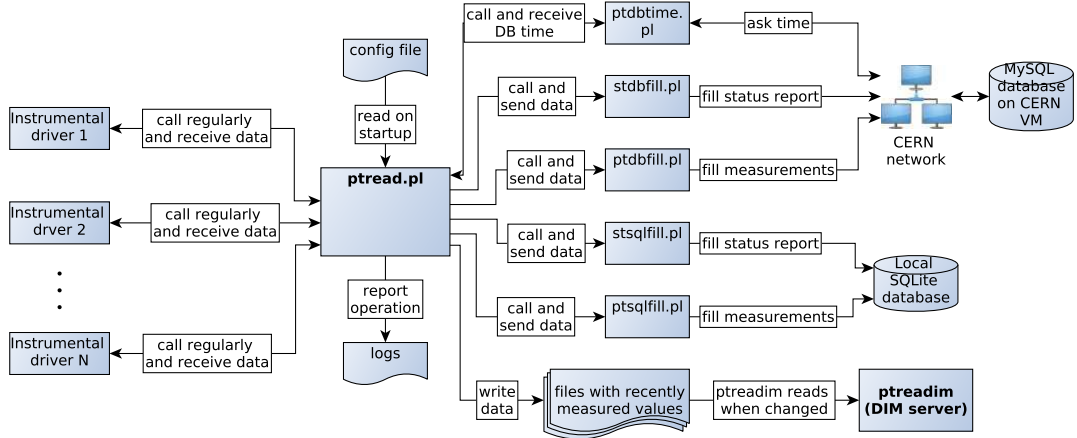


Figure 4.2: Diagram of pthead operation. The pthead and the ptheadim programs run as daemons. The pthead calls instrumental drivers and then database-writing scripts. It also writes the data to files, which are monitored by the ptheadim. The ptheadim publishes fresh data whenever any file is changed.

target experts and sparing the resources of the DCS. The development focuses now on the drivers and information transfer to the databases and to the DCS and the role of database clients is not clear yet. The optional SQLite database gives the opportunity to operate the system autonomously, without any network connection. This might be helpful in case of a network failure.

As was stated before, the pthead package consists mainly of Perl scripts. The diagram, showing how the package works, is on figure⁶ 4.2. The hearth of the system is a Perl program pthead, which runs as a daemon⁷ and calls instrumental drivers on schedule, given in the configuration file, which also contains names of the drivers, parameters they should be called with and names of the measured values. The calls are of two types. One is the usual request for measurement data; the other is a request for status information. That enables monitoring of the instruments and error tracing. After receiving the data, the pthead calls database-filling scripts and writes values into simple text files. The files are monitored by a DIM server ptheadim, which publishes fresh data right after any of them is changed. The data can be read by the DCS, which has the role of a DIM subscriber (see [24]). The program ptheadim is written in C++ and also runs in the background.

4.1.2 Instrumental drivers

The instrumental drivers are command-line applications written in Perl. They are primarily designed to be called by the pthead. That means to provide two functions: Firstly to ask the devices for measurement data and print them on the standard output as a comma-separated string. Secondly to print short device status information. Its content depends on what information can the instrument provide. The current settings and an error queue are the most useful ones. There

⁶Figures 4.1, 4.2 and 4.3 were drawn using yEd diagram editor.

⁷Linux term for a background process, 'service' in Windows terminology

is a possibility to run them directly from the command line too. That can be useful for testing and changing the device settings. They have a switch between the comma-separated output and a 'human-readable' output. The writing of several drivers⁸ was the main contribution of the author of this thesis to the pthead project.

The addition of a driver to the package involves, apart from writing the driver code, also design of the database tables, an entry in the pthead configuration file and several modifications in server-filling Perl scripts. There is a room for further improvement, because it would be better just edit some configuration file, than the code itself.

4.1.3 Current status and future of the pthead

The list of drivers is nearly complete and the package is being tested. The acquisition and sending data to the databases seems to work well. The DIM server is in provisional operation and is still being developed. Some more elaborate testing of the whole system is to be done. Only operation in "easy conditions" have been tried so far.

The role of the database clients is not clear yet. The author of this thesis has written a program `monitorpt` in Python, which can plot data from the MySQL database using Matplotlib library. It is only a simple command-line application so far, but there are some interesting possibilities of its future development. The similarity of the MySQL and SQLite databases encourages to extend the support to both of them. Only simple modifications would be needed and one would have a tool to visualize the local data without any network. That can be practical, for example, in the beginning of run when the refrigerator is being started and people are in the old control room. For such cases the command-line nature of the program could be an obstacle. A graphical user interface would be better. The difficulties and advantages of such an extension are to be considered yet.

4.2 Simulations of NMR coils setup

4.2.1 Criteria of a coil setup

The Drell–Yan program with an intense hadron beam needs new target cells. There are going to be two of them, each 55 cm long, with 4 cm in diameter and with a 20 cm gap between (see the section 3.1). There were three cells during most of previous polarized runs.

The setup of the NMR coils for the new cells is being discussed. As was said in the section 3.4.1, the coil filling factor is a crucial parameter for the NMR signal strength. The polarization measurement is tricky in this point, because we do not care only about the quality of the signal. The location it comes from is important too. The sensitivity near the target axis is more important than near the surface. Most of the scattering events happen on the target axis, since the Gaussian-like beam intensity is maximum there. Another issue is that the

⁸Namely to Picowatt AVS-47-B resistance bridge, Phase Matrix EIP-548-B frequency counter, Keithley 2000 multimeter, Siemens Multireg C1732 multi-channel acquisition unit and plotter and HP 34970A multi-channel acquisition unit.

more intense beam means there is a stronger heat input, so the polarization can possibly decrease a bit faster here. On the other hand, coils inside the target volume, which would be sensitive to that region, add a background material and lower the dilution factor (see the section 3.1).

To describe the "sampling" of the target by the NMR the **local filling factor** [30] is introduced. The energy of the magnetic field B of the coil with inductance L is

$$E = \frac{1}{2} L J^2 = \frac{1}{2} \int_V \frac{B^2(\vec{r})}{\mu(\vec{r}, \omega)} dV, \quad (4.1)$$

where V is volume where the field is not negligible, J is the current in the coil and $\mu(\vec{r}, \omega) = \mu_0(1 + \chi(\vec{r}, \omega))$. Considering $\chi(\vec{r}) = 0$ outside the target volume V_{trg} and $\chi(\vec{r}, \omega) = \chi(\omega)$ inside, one can express the filling factor. Remembering the definition (3.26) of the filling factor η , we write

$$1 + \eta\chi(\omega) = \frac{L(\omega)}{L_0} = \frac{\frac{1}{1+\chi(\omega)} \int_{V_{\text{trg}}} B^2 dV + \int_{V_{\text{out}}} B^2 dV}{\int_V B^2 dV}. \quad (4.2)$$

Using $V = V_{\text{trg}} + V_{\text{out}}$, which implies $\int_{V_{\text{out}}} B^2 dV - \int_V B^2 dV = -\int_{V_{\text{trg}}} B^2 dV$, we get

$$\eta = -\frac{1}{1 + \chi} \frac{\int_{V_{\text{trg}}} B^2 dV}{\int_V B^2 dV}. \quad (4.3)$$

Several modifications to the formula have to be made. Since we care only about the magnitude, we can forget about the sign. The nuclear magnetic susceptibility $\chi(\omega) \ll 1$, even in resonance. The target material is not homogeneous, it has a form of beads, that occupy only fraction F_P (called the packing fraction) of the V_{targ} . Only B_{\perp} , the part of the RF field perpendicular to the static field, couples to the spins. The procedure can be revised, considering $B^2 = B_z^2 + B_{\perp}^2$ and $\chi = 0$ for B_z , yielding

$$\eta = F_P \frac{\int_{V_{\text{trg}}} B_{\perp}^2(\vec{r}) dV}{2 \int_V B^2(\vec{r}) dV}. \quad (4.4)$$

The factor $1/2$ takes into account that only the part of linear RF field rotating with the spins couples to them, while the counter-rotating does not. Now it seems natural to define the local filling factor [30]

$$\eta(\vec{r}) = \frac{B_{\perp}^2(\vec{r})}{2 \int_V B^2(\vec{r}) dV}, \quad (4.5)$$

which shows how the material at position \vec{r} couples to the NMR coil.

In the SMC target publication [3] a single number is used to evaluate the quality of the coil setup. It is the difference in sampling of the target volume by the beam and the NMR system

$$\Delta S = \frac{1}{2} \int_{V_{\text{targ}}} |c_{\text{beam}} I_{\text{beam}}(\vec{r}) - c_{\text{NMR}} B_{\perp}^2(\vec{r})| dV, \quad (4.6)$$

where $I_{\text{beam}}(\vec{r})$ is the beam profile and $c_{\text{beam}, \text{NMR}}$ are normalization factors.

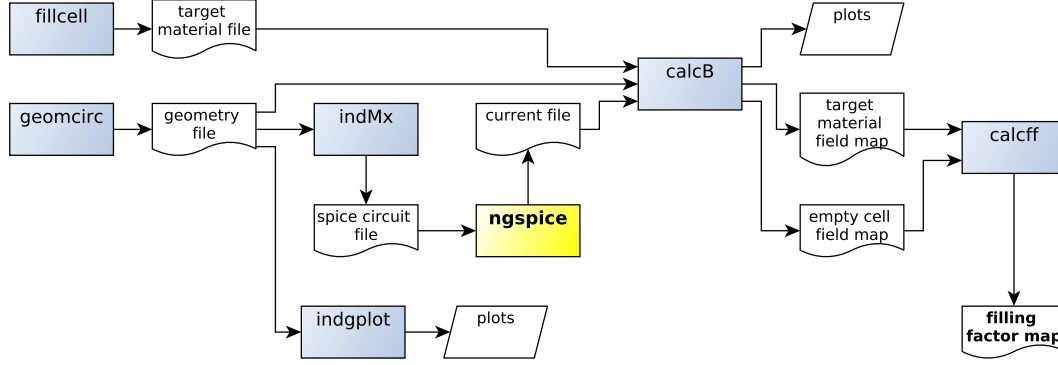


Figure 4.3: Calculating filling factors with rfindcalc. Coil geometries are defined using geomcirc. The geometry can be visualized by indgplot for checking. Inductance matrix is calculated by indMx. The currents in coils are calculated using ngspice [37]. The currents and geometries are used to calculate magnetic field in empty and filled target with calcB. The filling simulator fillcell can be used. Program calcff then calculates the filling factor $\eta(\vec{r})$. The programs from the rfindcalc package are indicated in blue.

4.2.2 Simulation with the rfindcalc package

To calculate the local filling factor $\eta(\vec{r})$ from the equation (4.6) one needs to know shapes and positions of the coils and the currents that flow inside them. There is a complication, because coils are inductively coupled to each other. Moreover there are couplings to other conducting parts around — the microwave cavity, the ^3He filling tube and the heat exchanger. The coupling is described by an inductance matrix. The matrix, as well as other parameters of the resonant circuits, have to be taken into account if one want to calculate the currents.

There is a program package called **rfindcalc**, written by Jaakko Koivuniemi. It is a set of C++ programs and scripts, designed to calculate both local and global filling factors. Some of the programs use the ROOT⁹ environment.

First the geometry of the coils and conducting materials is defined using geomcirc. Coils are build from simple geometrical elements, straight and bent tubes, connected in series. The program decomposes them into volume elements dV_k with user-defined refinement. An unit current \vec{J}_k , parallel to the tube axis, is assigned to every element. Also resistivity and intended frequency is set. Geometry can be visualized by program indgplot, so one can check if the design was done correctly. A proton coil is shown on figure 4.4a. Program indMx then calculates the inductance matrix using the Neumann’s formula [30]

$$M_{ij} = \frac{\mu_r \mu_0}{4\pi J_i J_j} \int_{V_i} \int_{V_j} V_j \frac{\vec{J}(\vec{r}_i) \cdot \vec{J}(\vec{r}_j)}{|\vec{r}_i - \vec{r}_j|} dV_i dV_j, \quad (4.7)$$

where M_{ij} is the inductance between i -th and j -th coil, $J(\vec{r})$ is electric current density. The integration is done numerically using Monte Carlo approach. Random points are generated inside every volume element dV_k and summation is done

⁹A CERN-developed framework for data processing and analysis, based on C++. See [42].

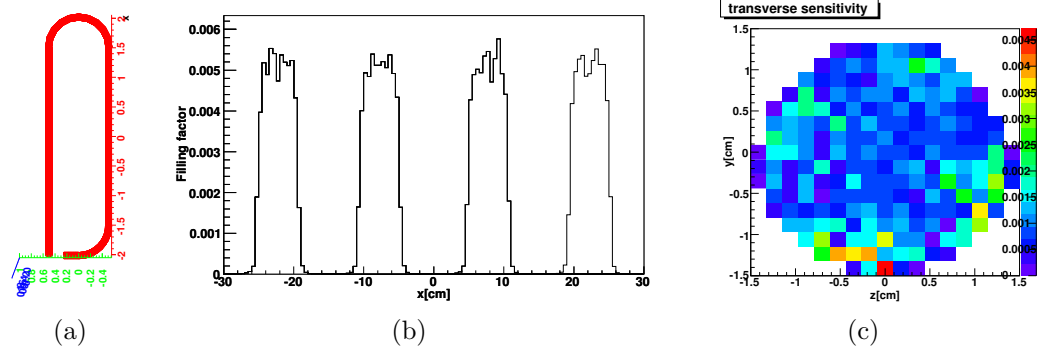


Figure 4.4: (a) A figure of the proton coil used in 2002 drawn by indgplot. (b) The longitudinal sensitivity, the bin width is 0.5 cm. Summing the bins one get total filling factor 0.05–0.06. (c) The transverse sensitivity from the 95% signal volume for all upstream coils. The bin size is about $0.18 \times 0.18 \text{ cm}^2$. Both sensitivities were calculated by rfindcalc package and refer to upstream deuteron coils used in 2003–2004 runs [30].

over both elements and points inside them. Thus one can avoid singularity in self-inductance and systematic errors due to deterministic sampling. The inductance can be also measured. Program indMx also calculates coil resistances [30]

A simplified model of the coupled Q-meter circuits and a ground loop simulating the other conducting materials is solved using **ngspice**¹⁰ The results can be compared with the measured Q-curves (NMR "baselines", see the section 3.4.1), but still one have to take them as an approximate values [30]. The calculated currents are used for field calculation.

The magnetic field calculation is done by program calcB. Coils are made of tubes which are far away from each other, so cylindrically symmetric current density in the cross-section of the tubes is assumed. The unit currents J_k in volume elements are multiplied by the corresponding coil currents. The skin effect is taken into account. Then the field is calculated using the Biot-Savart law [30]

$$\vec{B}(\vec{r}) = \frac{\mu_0}{4\pi} \int_{V_1} \frac{\vec{J}(\vec{r}_1) \times (\vec{r} - \vec{r}_1)}{|\vec{r} - \vec{r}_1|^3} dV_1 \quad (4.8)$$

and the same Monte Carlo approach as indMx. Program fillcell simulates the target filling and can be used to filling factor estimate. When magnetic fields in empty and filled cells is calculated, the filling factor is easily obtained from equation (4.6) using program calcff. Results from deuteron coils used in 2003–2004 runs are shown on figure 4.4 for illustration.

4.2.3 Rfindcalc testing

The rfindcalc package is quite complex. It is useful to test if the calculations are reasonably accurate. The easiest way of doing this is to compare the results for some particularly simple geometries with results of approximate analytical

¹⁰An open-source circuit simulator, based on Berkeley's Spice. See [37].

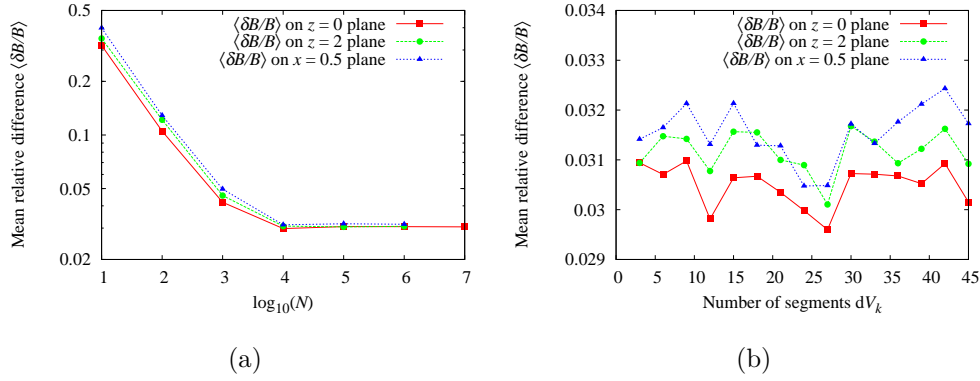


Figure 4.5: Mean relative differences between magnetic field calculated with calcB and by approximate analytic formula on three planes. (a) Dependence on number of random points used for calculation (12 segments used), (b) dependence on number of segments dV_k (10^4 random points used).

formulas. This was done by the author of this thesis for the case of a thin straight tube. It can be modeled as an infinitely thin wire of length l . Lets consider that the wire is placed in the center of the coordinate system, parallel to the z -axis, and there is a current J flowing inside. The Biot-Savart law (4.8) gives for this case

$$\vec{B}(\vec{r}) = \frac{\mu_0}{4\pi R} \left[\frac{z + l/2}{\sqrt{(z + l/2)^2 + R^2}} - \frac{z - l/2}{\sqrt{(z - l/2)^2 + R^2}} \right] \vec{e}_\phi, \quad (4.9)$$

where \vec{e}_ϕ is an unit vector in direction of the azimuthal angle ϕ in cylindrical coordinates.

The procedure was done programatically, using bash shell scripts. First the geometry was defined by calling the geomcirc. The parameters were tube length $l = 40$ mm, radius $r = 0.1$ mm and wall thickness $w = 0.05$ mm. Then the magnetic field was calculated with calcB on planes $x = 0.5$, $z = 0$ and $z = 2$. For every point in the produced field files the magnetic field was calculated from (4.9) using a Perl script. The differences between fields were evaluated using an AWK¹¹ script. Finally, the differences were plotted using gnuplot¹².

The dependences of the differences on the number of random points, used for calculation, and the number of geometric segments (axial, radial and angular), the tube consists of, were investigated. The results are shown in figure 4.5. The mean relative difference

$$\frac{|\delta \vec{B}|}{|\vec{B}_{\text{analytic}}|} = \frac{|\vec{B}_{\text{calcB}} - \vec{B}_{\text{analytic}}|}{|\vec{B}_{\text{analytic}}|} \quad (4.10)$$

for each plane was used as a criterion. We can see that the accuracy depends on number of the random points N for $N < 10^4$. Using more points the calculation only consumes more time without giving better results. The mean difference is then about 3%. That is sufficient for a practical use of the rfindcalc. The difference may be caused by the finite radius of the wire. One would expect the

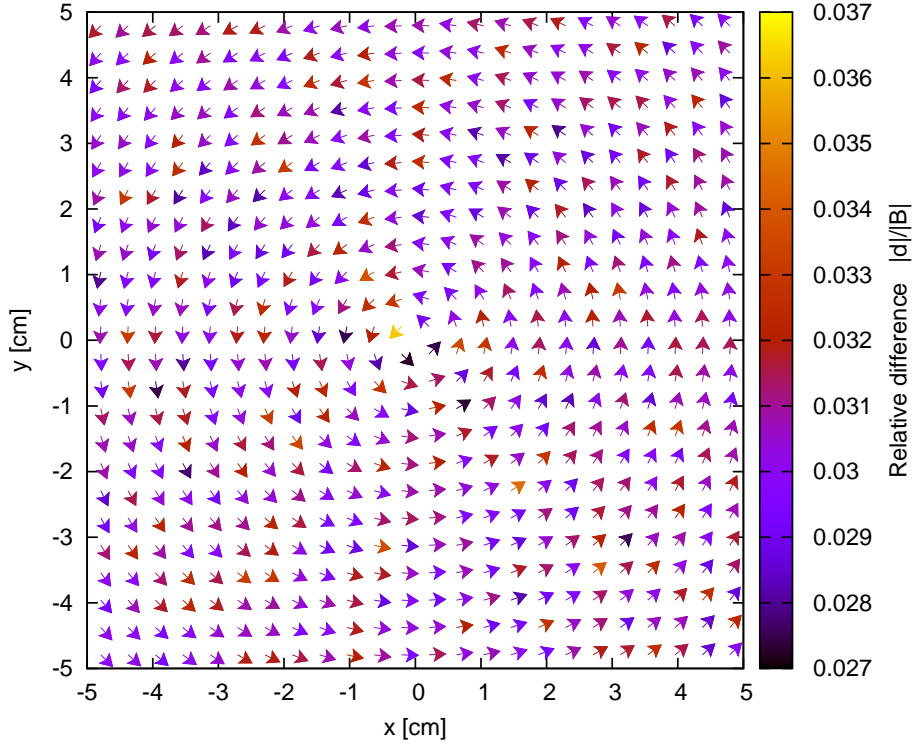
¹¹Programming language used for data extraction, standard on all Unix platforms.

¹²A command-line driven, interactive and freely-distributed plotting program.

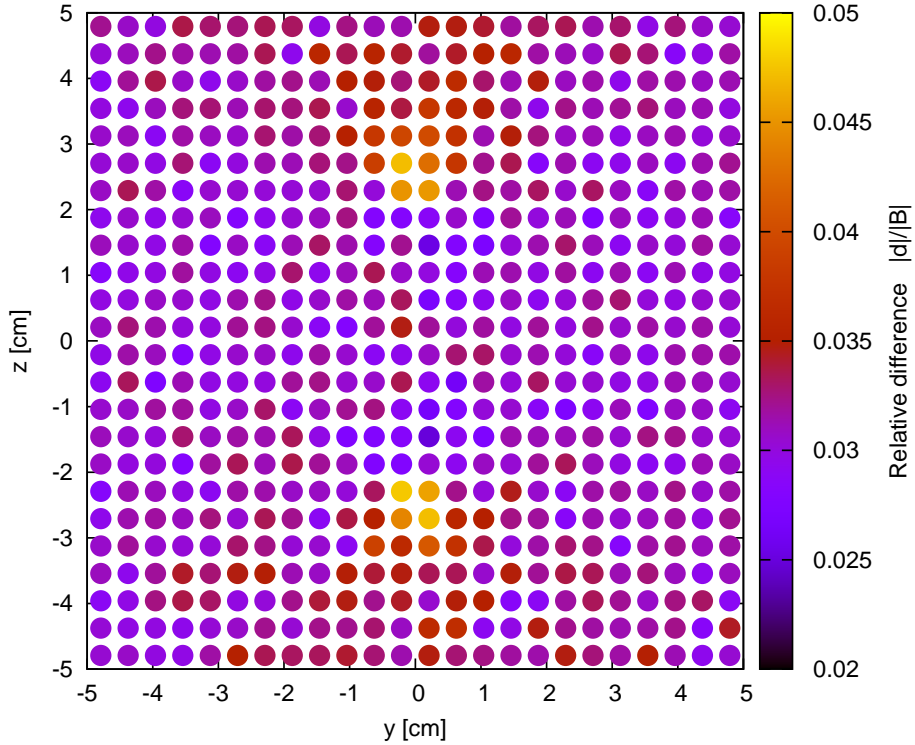
relative difference to decrease with distance from the axis in that case, because the approximation should hold better in greater distance. When we look on the figure 4.6 we do not see such a dependence, but a clear systematical increase in differences can be seen near the ends of the wire.

On the other hand the differences were found independent on the number of geometric segments, created by geomcirc (see the figure 4.5b) . The coil geometry is build from tubes and bents, which are divided by the geomcirc into volume segments dV_k . The program uses cylindrical or toroidal coordinates to describe the segments and to generate random points inside. They are then transformed into global cartesian coordinate system using the Euler angles and translations (see [30]). That means the accuracy should not depend on the number of segments, if the number of random points is large, especially for the extremely simple geometry used for the testing.

The conclusion is that the precision of the magnetic field calculation is 3% or better. That seems to be suitable since there are other possible sources of errors, like the simplified circuit model.



(a) Relative differences on plane $z = 0$. The arrows show direction of vectors, colors denote their magnitudes. No clear maximum can be seen. The vectors differ in magnitude, not in direction.



(b) Relative differences on plane $x = 0.5$. Since the z -component of the magnetic field is always zero from symmetry reasons, only the magnitudes are shown. We can see maxima near the wire ends ($z = \pm 2$).

Figure 4.6: Spatial dependence of relative differences in magnetic field $[\delta \vec{B}/|\vec{B}_{\text{analytic}}|](\vec{r})$ for 10^6 random points and 12 segments.

Conclusion

The description of goals of the COMPASS Drell–Yan program was given. The physical meaning of the TMDs, accessible to the program, was outlined and the means of their extraction from the measured asymmetries sketched. COMPASS is going to collect more than 5000 DY events per day. The verification of the sign-reversal property of the Sivers function of the proton will be performed by measuring the $A^{\sin\phi}$ asymmetry. The pretzelosity and transversity of the proton will be accessible too. The experiment is an important test of QCD in non-perturbative regime.

General description of the COMPASS apparatus was given. Modifications for the Drell–Yan program were discussed. The hadron absorber is needed to lower occupancies of trackers by hadrons, which are of no importance for DY. This will restrict versatility of the apparatus and complicate the vertex reconstruction, but it is necessary to enable detection of the DY events at sufficient rate. The radiation dose in the hall will be just below the CERN’s limits for ”radiation supervised area”. The control room will be moved from the experimental hall to office building, following the ALARA principle. This brings challenges to the polarized target monitoring.

The polarized target was described in greater detail. Physical principles as well as practical realization of the dilution refrigerator, dynamic nuclear polarization system and continuous-wave NMR system were covered. The dilution refrigerator has a cooling power of about 5 mW at 70 K and about 1 W at 600 mK. The microwave DNP system is able to polarize ^1H nuclei in ammonia to a degree of about 90%. It works on a principle of cooling electronic spin-spin interaction reservoir, which is thermally connected to the nuclear Zeeman reservoir. For the NMR system a good ”sampling” of the target is crucial, but this demand is contradictory to demands of a strong signal and of no background material in the target cells.

The demands on the systems from both the low-temperature and the high-energy-physics points of view were discussed. There are many trade-offs in such an experiment, like the isolation of the cryostat versus spectrometer acceptance, or the NMR coils issue.

The new monitoring system of the dilution refrigerator — program package `ptread`, based on Linux technologies — was described. Its task will be to collect data from the sensors and publish them via DIM server for the standard COMPASS Detector Control System. Alternative ways of reaching the data are to be discussed yet. A client with a graphical user interface, capable to use both remote MySQL databases and local SQLite databases for the case of network failure may be the next step. The author wrote five instrumental drivers and incorporated them into the package. He contributed to the documentation and to the discussion about the overall design. He will continue to cooperate on the development.

The software for NMR coils simulation was tested by the author, the relative error of the calculated magnetic field was found equal or less to 3%. That is suitable, considering other sources of errors, like the simplified circuit model used.

Bibliography

- [1] ABBON, P., et al. *Nucl. Instrum. Methods Phys. Res. A* 577 (2007), 455.
- [2] ABRAGAM, A., GOLDMAN, M. *Rep. Prog. Phys.* 41 (1978) 395.
- [3] ADAMS, D. et al. *Nucl. Instrum. Methods Phys. Res. A* 437 (1999), 23.
- [4] ADOLPH, C. et al. *In-absorber-SciFi-detector for Drell–Yan program*. Presented on Drell–Yan Hardware meeting, CERN, November 14, 2012.
- [5] ARNOLD, S., METZ, A, SCHLEGEL, M. *Phys. Rev. D* 79 (2009) 034005.
- [6] BARONE, V., DRAGO, A., RATCLIFFE, P. G. *Phys. Rept.* 359 (2002) 1.
- [7] BJORKEN, J. D, PASCHOS, E. A. *Phys. Rev.* 185 (1969), 1975.
- [8] DE BOER, W. *Dynamic Orientation of Nuclei at Low Temperatures*. CERN Yellow report 74-11 (1974). Available at:
<http://cds.cern.ch/collection/CERN%20Yellow%20Reports>
- [9] BRESKIN, A. et al. *Nucl. Instrum. Methods Phys. Res. A* 535 (2004), 303.
- [10] CHARPAK, G. et al. *Nucl. Instrum. Methods Phys. Res. A* 376 (1996) 29.
- [11] CHIOSO, M., GNESI, I., QUINTANS, C. *COMPASS Note 2010-4* (2010). Available at:
http://wwwcompass.cern.ch/compass/notes_public/2010-4.pdf.
- [12] CHÝLA, J. *Quarks, Partons and Quantum Chromodynamics*. Available at: <http://www-hep2.fzu.cz/~chyla/lectures/text.pdf>.
- [13] COLLINS-SUSSMAN, B., FITZPATRICK, B. W., PILATO, C. M. *Version Control with Subversion*. Available at: <http://svnbook.red-bean.com/>.
- [14] THE COMPASS COLLABORATION. *COMPASS-II Proposal*. CERN-SPSC-2010-014. SPSC-P-340. Available at: <http://wwwcompass.cern.ch/>.
- [15] *The COMPASS homepage*. <http://wwwcompass.cern.ch/>.
- [16] COMPASS DCS GROUP. *Detectors Control System homepage*. <https://compass-dcs.web.cern.ch/compass-dcs/intro.html>.
- [17] DENISOV, O. *2012 Drell–Yan test beam—proposal, expectations, results*. Presented on Drell–Yan Analysis meeting, CERN, February 4, 2013.
- [18] DICKE, R. H. *Phys. Rev.* 93 (1954) 99.
- [19] DOSHITA, N. *Past and Future of COMPASS Polarized Target*. Presented at SPIN conference, Prague, July 20–26, 2008.
- [20] DOSHITA, N. et al. *Nucl. Instrum. Methods Phys. Res. A* 526 (2004) 138.

- [21] DRELL, S. D., YAN, T. M. *Phys. Rev. Lett.* 25 (1970), 316.
- [22] EXPERIMENTAL GROUP, RIKEN BNL RESEARCH CENTER.
Sifting out the sources of spin. Available at:
<http://www.rikenresearch.riken.jp/eng/research/6054>.
- [23] FEYNMAN, R. P. *Phys. Rev. Lett.* 23 (1969) 1415.
- [24] GASPAR, C. et al. *DIM homepage*. <http://dim.web.cern.ch/dim/>
- [25] GAUTHERON, F. et al. *Nucl. Instrum. Methods Phys. Res. A* 526 (2004) 147.
- [26] GDD, CERN. *Gas Detectors Development homepage*.
<http://gdd.web.cern.ch/GDD/>.
- [27] KLÍMA, J., VELICKÝ, B. *Kvantová mechanika II*. Praha: Univerzita Karlova, 1985.
- [28] *Linux GPIB package homepage*. <http://linux-gpib.sourceforge.net/>.
- [29] KOIVUNIEMI, J. H. *Polarized target web*. PT group part of the internal COMPASS Wiki.
- [30] KOIVUNIEMI, J. H. et al. *COMPASS Note 2005-19* (2005).
- [31] KOIVUNIEMI, J. H. et al. *Journal of Physics: Conference series* 150 (2009) 012023.
- [32] KOIVUNIEMI, J. H., MATOUSEK, J. *Ptread HOWTO*. Available at:
<http://wwwcompass.cern.ch/compass/detector/target/ptread/index.htm>.
- [33] KONDO K. et al. *Nucl. Instrum. Methods Phys. Res. A* 526 (2004) 70.
- [34] KOTZINIAN, A. *COMPASS Note 2010-2* (2010). Available at:
http://wwwcompass.cern.ch/compass/notes_public/2010-2.pdf.
- [35] LEVIT, D. et al. *The COMPASS DAQ Upgrade*. Presented on COMPASS Collaboration meeting, CERN, 17–18 November 2011.
- [36] MAGGIORA, A. *Final hadron absorber simulation status*. Presented on Drell–Yan Hardware meeting, CERN, September 5, 2012.
- [37] *ngspice homepage* <http://ngspice.sourceforge.net/presentation.html>.
- [38] NOVÝ, J. *COMPASS DAQ—Basic control system*. Diploma thesis, ČVUT, Prague, 2012.
- [39] PEŠEK, M. *Low temperature proton polarized target for nucleon structure studies at COMPASS*. Bachelor thesis, Charles university, Prague, 2012.
- [40] QUINTANS, C. *Transverse spin physics from the Drell-Yan process in COMPASS*. Presented on ECT Workshop on Drell–Yan Scattering, Lisbon, May 23, 2012. Available at:
<http://wwwcompass.cern.ch/compass/publications/talks/>.

- [41] REICHERTZ, L. A. et al. *Nucl. Instrum. Methods Phys. Res. A* 340 (1994) 578.
- [42] THE ROOT TEAM. *ROOT homepage* <http://root.cern.ch>.
- [43] SAULI, F. *Nucl. Instrum. Methods Phys. Res. A* 386 (1997) 531.
- [44] SKRBEK, L. et al. *Fyzika nízkých teplot*. Praha: MatfyzPress, 2011. ISBN 978-80-7378-168-2.
- [45] THUNEBERG, E. *Liquid mixture of ^3He and ^4He* . Available at <http://lth.tkk.fi/research/theory/mixture.html>.
- [46] ŽÁČEK, J. *Úvod do fyziky elementárních částic*. Praha: Karolinum, 2009. ISBN 978-80-246-1109-9.

List of Abbreviations

ALARA	As Low As Reasonably Achievable (the radiation dose)
CERN	European Organization for Nuclear Research (originating from 'Conseil Européen pour la Recherche Nucléaire'—its provisional predecessor)
CMS	Center-of-Mass System
COMPASS	Common Muon and Proton Apparatus for Structure and Spectroscopy
DAQ	Data Acquisition
DATE	Data Acquisition and Test Environment
DCS	Detector Control System
DIS	Deep Inelastic Scattering
DIM	Distributed Information Management
DNP	Dynamic Nuclear Polarization
DY	Drell–Yan
EIO	Extended Interaction Oscillator
ESR	Electron Spin Resonance
FPGA	Field Programmable Gate Array
GEM	Gas Electron Multiplier
GPIO	General Purpose Interface Bus
LAS	Large Angle Spectrometer
LED	Light Emitting Diode
Micromegas	Micromesh Gaseous Structure
MWPC	Multiwire Proportional Chamber
NMR	Nuclear Magnetic Resonance
PDF	Parton Distribution Function
PLC	Programmable Logic Controller
QCD	Quantum Chromodynamics
QED	Quantum Electrodynamics
TMD	Transverse Momentum Dependent (PDFs)

RICH	Ring-Imaging Cherenkov (detector)
SAS	Small Angle Spectrometer
SIDIS	Semi-Inclusive Deep Inelastic Scattering
SPS	Super Proton Synchrotron
SMC	Spin Muon Collaboration
SQL	Structred Query Language
THGEM	Thick GEM